THEORETICAL AND EXPERIMENTAL STUDIES ON NONLINEAR LUMPED ELEMENT TRANSMISSION LINES FOR RF GENERATION

KUEK NGEE SIANG
(B.Eng.(1st class Hons.), NUS)

A THESIS SUBMITTED

FOR THE DEGREE OF DOCTOR OF PHILOSOPHY

DEPARTMENT OF ELECTRICAL & COMPUTER ENGINEERING

NATIONAL UNIVERSITY OF SINGAPORE

2013

DECLARATION

I hereby declare that the thesis is my original work and it has been written by me in its entirety.

I have duly acknowledged all the sources of information which have been used in this thesis.

This thesis has also not been submitted for any degree in any university previously.

Kuek Ngee Siang

29 July 2013

ACKNOWLEDGEMENTS

First and foremost, I wish to express sincere thanks to Professor Liew Ah Choy, my supervisor, for accepting me as his last Ph.D. student before he retires. I am very grateful to him for being ready to answer my numerous questions anytime. He has been extremely patient and understanding with me; especially when I encountered some medical issues at home in the midst of the research work. His guidance and encouragement have been a driving force in expediting the completion of this thesis.

I would like to extend my heartfelt gratitude to Professor Edl Schamiloglu, my co-supervisor, for his broad outlook and resourcefulness. Even though we are separated by thousands of miles, he never fails to respond to my email queries. He is very sharp and quick thinking as he promptly directs me to the essential materials to conduct the research work.

It is also my pleasure to thank Dr Jose Rossi for being such a great help in reviewing my conference and journal papers before submission. His technical advice and constructive criticism have greatly improved the quality of the technical papers.

I would also like to extend my gratitude to Oh Hock Wuan, my friend and former colleague, for helping me with the high voltage experiments. His deft pair of hands and excellent hardware skill have help accelerated the numerous experiment setups, without which the research work would not have proceeded so quickly and smoothly. I greatly appreciate his invaluable time and effort for not only helping to conduct the experiments, but also for the fruitful discussions on measurement techniques and the experiment results.

I am also thankful to the staff at the Power Technology Laboratory at NUS for their assistance in purchasing the materials necessary for the experiments.

Last but not least, I would like to thank my family for their love, support and encouragement throughout this entire process.

TABLE OF CONTENTS

SUMMARY

A nonlinear lumped element transmission line (NLETL) that consists of a LC ladder network can be used to convert a rectangular input pump pulse to a series of RF oscillations at the output. The discreteness of the LC sections in the network contributes to the line dispersion while the nonlinearity of the LC elements produces the nonlinear characteristics of the line. Both of these properties combine to produce wave trains of high frequency. Three types of lines were studied: a) nonlinear capacitive line (NLCL) where only the capacitive component is nonlinear; b) nonlinear inductive line (NLIL) where only the inductive component is nonlinear; and c) nonlinear hybrid line (NLHL) where both LC components are nonlinear. Based on circuit theory, a NLETL circuit model was developed for simulation and extensive parametric studies were carried out to understand the behaviour and characteristics of these lines. Generally, results from the NLETL model showed good agreement to the experimental data. The voltage modulation and the frequency content of the output RF pulses were analyzed. An innovative method for more efficient RF extraction was implemented in the NLCL. A simple novel method was also found to obtain the necessary material parameters for modeling the NLIL. For better matching to resistive load, the NLHL (where no experimental NLHL has been reported to date) was successfully demonstrated in experiment.

LIST OF PUBLICATIONS

Conference Publications:

1. N.S. Kuek, A.C. Liew, E. Schamiloglu, and J.O. Rossi, "Circuit modeling of nonlinear lumped element transmission lines," *Proc. of 18th IEEE Int. Pulsed Power Conf.* (Chicago, IL, June 2011), pp. 185-192.

2. N.S. Kuek, A.C. Liew and E. Schamiloglu, "Experimental demonstration of nonlinear lumped element transmission lines using COTS components," *Proc. of 18th IEEE Int. Pulsed Power Conf.* (Chicago, IL, June 2011), pp. 193-198.

3. N.S. Kuek, A.C. Liew, E. Schamiloglu and J.O. Rossi, "Generating oscillating pulses using nonlinear capacitive transmission lines," *Proc. of 2012 IEEE Int. Power Modulator and High Voltage Conf.* (San Diego, CA, 2012), pp. 231-234.

4. N.S. Kuek, A.C. Liew, E. Schamiloglu and J.O. Rossi, "Nonlinear inductive line for producing oscillating pulses," *Proc. of 4th Euro-Asian Pulsed Power Conference* (Karlsruhe, Germany, Oct. 2012).

5. N.S. Kuek, A.C. Liew, E. Schamiloglu and J.O. Rossi, "Generating RF pulses using a nonlinear hybrid line," *Proc. of 19th IEEE Int. Pulsed Power Conf.* (San Francisco, CA, June 2013).

6. J.O Rossi, F.S. Yamasaki, N.S. Kuek, and E. Schamiloglu, "Design considerations in lossy dielectric nonlinear transmission lines," *Proc. of 19th IEEE Int. Pulsed Power Conf.* (San Francisco, CA, June 2013).

Journal Publications:

7. N.S. Kuek, A.C. Liew, E. Schamiloglu and J.O. Rossi, "Circuit modeling of nonlinear lumped element transmission lines including hybrid lines," *IEEE Transactions on Plasma Science*, vol. 40, no. 10, pp. 2523-2534, Oct. 2012.

8. N.S. Kuek, A.C. Liew, E. Schamiloglu and J.O. Rossi, "Pulsed RF oscillations on a nonlinear capacitive transmission line," *IEEE Transactions on Dielectrics and Electrical Insulation*, vol. 20, no. 4, pp. 1129-1135, Aug. 2013.

9. N.S. Kuek, A.C. Liew, E. Schamiloglu and J.O. Rossi, "Oscillating pulse generator based on a nonlinear inductive line," *IEEE Transactions on Plasma Science*, vol. 41, no. 10, pp. 2619-2624, Oct. 2013.

10. N.S. Kuek, A.C. Liew, E. Schamiloglu and J.O. Rossi, "RF pulse generator based on a nonlinear hybrid line," accepted for publication for *October 2014 Special Issue on Pulsed Power Science and Technology of the IEEE Transactions on Plasma Science*.

LIST OF TABLES

LIST OF FIGURES

LIST OF SYMBOLS

a,b	Capacitive nonlinearity factors
amp	Pulse amplitude
f_B	Bragg's frequency
i	Index ranging from 0 to (n-1)
l_e	Effective magnetic path length
n	Number of LC sections
t_r	Pulse Rise time
t_p	Pulse duration
v_p	Phase velocity
A_e	Effective cross-sectional area
C	Capacitor / Capacitance
C_0	Initial capacitance (at zero voltage)
C_{sat}	Saturation capacitance at large value of applied voltage V
C_x	Value of crosslink capacitor
$C(V)$	Capacitance as a function of voltage
E_{in}	Total input energy
E_{out}	Output energy
E_{RF}	Output RF energy
$H(t)$	Magnetic field strength
I_{gen}	Current from pulse generator / pulser
I_i	Current flowing in inductor at $(i+1)^{th}$ section

I_L	Current flowing in nonlinear inductor
I_S	Inductive nonlinearity factor
I_{sat}	Saturation scaling factor
I_t	Current shifting factor
L	Inductor / Inductance
L_{bias}	Isolating inductor
L_d	Differential inductance / effective inductance
L_0	Initial inductance (at zero current)
L_S	Asymptotic inductance with current increase
L_{sat}	Saturation inductance at large value of current
$L(I)$	Inductance as a function of current
$M(t)$	Mean value of magnetization vector
M_s	Saturation magnetization
N	Number of coil turns
P_{ave}	Average peak load power
R_{bias}	Value of biasing resistor
R_{gen}	Input impedance
R_{load}	Value of resistive load
R_L	Resistive loss in inductor
R_C	Resistive loss in capacitor
V_{bias}	Bias voltage applied to capacitor
V_{DC}	DC Power supply source
V_c	Voltage across nonlinear capacitor
Vc_i	Voltage across capacitor at $(i+1)^{th}$ section
V_i	Voltage at $(i+1)^{th}$ node

V_L	Voltage across nonlinear indcutor
V_{pt}	Peak-to-trough load oscillation voltage
V_{pump}	Input voltage pump pulse
V_{sat}	Saturation factor
Z_0	Characteristic impedance of LC section line
η_m	Matching efficiency
η_{RF}	RF efficiency
α	Dimensionless damping parameter
γ	Coupling coefficient
γ_0	Gyromagnetic ratio
μ_0	Permeability of free space
ΔT	Reduction in rise time
Ψ	Magnetic flux linkage
Ψ_t	Flux shifting factor

wrt	with respect to
ASP	asymmetric parallel
BD	breakdown
BT	barium titanate
COTS	Commercial-Off-The-Shelf
EM	Electromagnetic
ESR	Equivalent Series Resistance
FFT	Fast Fourier Transform
HPM	High Power Microwave
KdV	Korteweg-de Vries

LLG	Landau-Lifshitz-Gilbert
NLCL	Nonlinear Capacitive Line
NLETL	Nonlinear Lumped Element Transmission Line
NLHL	Nonlinear Hybrid Line
NLIL	Nonlinear Inductive Line
NLTL	Nonlinear Transmission Line
ODE	Ordinary Differential Equation
PDE	Partial Differential Equation
PFN	Pulse forming network
PFL	Pulse forming line
PMN	Lead-Manganese-Niobate
PSpice	Personal Simulation Program with Integrated Circuit Emphasis
RF	Radio Frequency
TL	Transmission Line
VMD	Voltage modulation depth
VMDI	Voltage modulation depth index

CHAPTER 1: INTRODUCTION

1.1 BACKGROUND

1.1.1 DESCRIPTION OF NONLINEAR TRANSMISSION LINE (NLTL)

The focus of the research work here is on lumped element transmission line (TL) that is periodically loaded with nonlinear elements and can be represented by an equivalent LC ladder circuit. These elements can be made up of nonlinear dielectric materials (or capacitors) or nonlinear magnetic materials (or inductors). This type of nonlinear transmission line (NLTL) is known to cause two effects on an input rectangular pulse: 1) forming electromagnetic (EM) shock waves [1] to sharpen the rise time of the input pulse and; 2) modulating the input pulse to produce an array of solitons. The term "soliton" was coined by Zabusky and Kruskal [2] in 1965 and it is a localized self-reinforcing solitary wave [3] that does not change its shape as it propagates and preserves its form after interaction with other solitons. Solitons are encountered in the analysis of water waves, plasmas, fiber optics, shock compression and NLTL [4]. The nonlinearity of the TL elements causes the pulse sharpening effect and if this nonlinearity is balanced by the dispersive characteristic of the TL, radio frequency (RF) oscillations in the form of solitons are produced. For the discrete and nonlinear nature of this type of line, it is called the nonlinear lumped element

transmission line (NLETL). The NLETL should be differentiated from the usual distributed transmission line filled with continuous media.

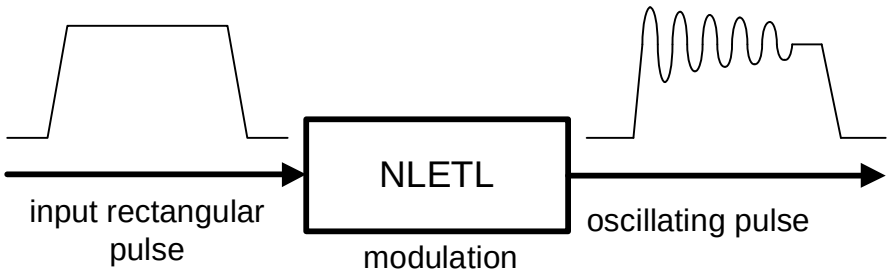

Figure 1.1 RF generation in NLETL.

As illustrated in Figure 1.1, a NLETL with nonlinear LC ladder network comprising either nonlinear inductors or nonlinear capacitors can be used to convert an input rectangular pump pulse into a train of oscillating pulses [5]-[7]. The input rectangular pump pulse injected into the line is steepened by the nonlinearity effect and, subsequently, modulated and broken into an array of solitons (oscillating pulse) due to dispersion that arises from the discreteness of the line. The background on this method of using nonlinear discrete elements to generate a train of solitons (resulting in oscillating signals) and a simplified theory on solitons are well described in [8].

Possible applications of the NLETL as a RF generator include satellite communications and communication systems in space vehicle, as high power microwave (HPM) sources for electronic countermeasures and remote sensing, as HPM source for radar applications and battlefield communication disruption, and in directed energy and nonlethal defense systems. Compared to conventional microwave sources that use electron beam [9]-[11], the advantages of NLETL as a beamless device for RF generation are:

a) simple discrete components are used;

b) does not use an electron beam in which heating from beam and beam

control will be a concern;

c) no applied external magnetic field is needed when compared to electron beam devices (eg. magnetron, gyrotron, klystron);

d) no vacuum required compare to microwave tubes;

e) no secondary x-ray radiation as no electron beam is employed; and

f) wide frequency tunability by DC biasing.

Research on NLETL is important as this method of RF generation offers a potentially simpler, compact and less costly system. The defence industries will be particularly interested in using it on a mobile platform to disrupt electronics. For homeland security, a mobile system based on NLETL can be used to stop runaway cars and boats.

1.1.2 SURVEY ON NLETL RESEARCH

Investigation of nonlinear lumped element transmission lines (NLETLs) has long been carried out to understand the principle of soliton generation [12]-[16] and the principle of pulse sharpening of the rise time of a voltage waveform [17]-[20]. Each of these lines consists of discrete parallel capacitive/dielectric and series inductive/magnetic elements connected in such a way to make up a chain of cascading LC segments. Nonlinearity in the line is introduced by having either nonlinear capacitive elements (with constant inductance) or nonlinear inductive elements (with constant capacitance). On the other hand, Afshari [21] and [22] has made use of NLETL for pulse shaping.

Earlier work on generating solitons using NLETLs has focused on comprehending the characteristics of soliton propagation and interaction. Ikezi [23]-

[25] and Kuusela [26]-[30] have done a great deal of work investigating soliton generation in NLETLs. Gradually, research on NLETL has progressed to producing a train of narrow pulses (solitary waves) [5], [6], [31]-[33]. It is now possible to use the NLETL technique to generate a series of narrow radio frequency (RF) pulses at megawatt power levels from an input rectangular pump pulse using nonlinear inductive line (NLIL) (consisting of nonlinear inductors but linear capacitors) and nonlinear capacitive line (NLCL) (consisting of nonlinear capacitors but linear inductors). NLIL and NLCL have been used for energy compression in the early days and can be traced to the Melville line [34] and Johannessen line [35] respectively. Belyantsev and his team have studied intensively the RF generation properties of NLCL [36] and [37] and NLIL [38]-[40]. A LC ladder network with both nonlinear capacitors and nonlinear inductors is called the nonlinear hybrid line (NLHL) or simply hybrid line.

The group from Oxford University has made use of nonlinear capacitive lines to produce 60 MW peak RF power at frequencies of 200 MHz by means of a modulated strip line cooled to 77 K using liquid nitrogen [7]; and also to produce 25 MW peak RF power at frequencies of 30 MHz by means of asymmetric parallel NLETL [41]. In [7], a numerical computer model was also developed to study the behaviour of the modulated strip line. When the input voltage increases, the modulation depth and frequency of the solitons produced by the line also increase. The modulation depth of the solitons can also be increased by adding more sections to the line. The model also studied the matching of the strip line to a linear load for 3 cases: under matched, approximately matched and over matched. In summary, the group believes that higher powers and higher frequencies are attainable by using materials with higher relaxation frequency and lower loss, better pulse injection and more line sections. This method has the possibility of rapid frequency change by biasing the

modulated line since the frequency of solitons generated is voltage dependent.

Another group from BAE systems (UK) has achieved 20 MW peak RF power at 1.0 GHz by using a nonlinear inductive line [42]. They made use of an LC ladder network with saturable magnetic material in the inductor and cross-link capacitors were added to modify the dispersion characteristic of the LC ladder network. Using this technique, they showed that it is possible to control the timing of the RF wave at the output and the frequency of the RF signal by adding a DC bias current in the nonlinear inductors. They also demonstrated that it is possible to increase system power by building phased arrays of NLTL circuits. They have built a NLIL circuit measuring 0.5 m x 0.5 m x 0.07 m that has a centre frequency of 1 GHz and peak output power of 20 MW. It can operate at a pulse repetition frequency (PRF) up to 1.5 kHz. The input pump pulse has amplitude 30-50 kV with rise time of 10 ns and pulse width of 50 ns. They have also demonstrated phase and frequency control by using 4 identical NLIL circuits (each producing RF pulses of 30ns with 1 GHz centre frequency and tuneability from 700 MHz to 1.3 GHz). The NLIL can operate with centre frequencies from 200 MHz to 2 GHz and is suitable for operation in phased arrays with tuneability of at least +/-20% about the centre frequency having bandwidth from 2.5% to 40%.

Work has also been carried out to study the hybrid line using numerical simulation with the goal of better matching to a resistive load [43] and [44]. In [43], the authors used Spice simulator to study the nonlinear hybrid line that consists of discrete nonlinear inductors and nonlinear capacitors. They simulated a 50-section line made up of varactor diodes MV2201 and variable inductors with initial value of 54 nH. The nonlinear inductors were modelled by using hyperbolic tangent function. Results using nonlinear and linear inductors were compared. In summary, the authors opined

that there is a minimum rise time for the input pulse to excite high frequency oscillations at the output and there is a range of optimal values to produce maximum modulation depth close to saturation. They projected that a hybrid line made of parallel plates with nonlinear medium having alternate lumped ferroelectric tiles (capacitors) and ferrite blocks (inductors) could be developed to produce solitons with frequency between 1-2 GHz.

It should be noted that a distributed NLTL filled with ferrites has also been used to sharpen the rise time of an input pulse [45]-[48] and by introducing an external biasing magnetic field, it can be tuned to produce RF oscillations. Dolan has carried out a number of works on pulse-sharpening effect in ferrite-loaded NLTL [49]-[52] that is due to the formation of an electromagnetic shock front at the leading edge of a pulse waveform. Rostov and his team has numerous publications on applying an external biasing magnetic field on a coaxial line filled with ferrite cores to produce subgigawatt RF pulses [53]-[56]. Similar magnetic biased ferrite-filled line or gyromagnetic NLTL are also investigated by Bragg [57] and [58] and Chadwick [59].

Another interesting research area related to NLTL is the work of D. S. Ricketts at Harvard University on self-sustained electrical soliton oscillator with experimental demonstration [60]. The oscillator consists of a NLTL and a nonlinear amplifier with adaptive bias control. This one-port system can self-generate a periodic soliton pulse train from ambient noise. One of the amplifiers was implemented using MOS transistors for a low megahertz soliton oscillator prototype with pulse repetition rate of 1 MHz and soliton pulse width of 100 ns. Another prototype was constructed using RF bipolar transistors in the amplifier and p-n junction diodes as varactors in the artificial NLTL. It produced soliton with pulse width of 827 ps and has pulse repetition rate of 130 MHz.

1.1.3 THEORETICAL CONSIDERATIONS

There are three basic equations for describing the discrete LC ladder network. The phase velocity v_p, Bragg's frequency f_B, and characteristic impedance Z_0 of the line are given as follows [61] and [62]:

$$v_p = \frac{1}{\sqrt{L(I)C(V)}} \tag{1.1}$$

$$f_B = \frac{1}{\pi \cdot \sqrt{L(I)C(V)}} \tag{1.2}$$

$$Z_0 = \sqrt{\frac{L(I)}{C(V)}} \quad , \tag{1.3}$$

where

C(V) – capacitance as a function of voltage V

L(I) – inductance as a function of current I.

The principle of RF or soliton generation using an artificial LC ladder circuit is simple to describe qualitatively [8], [21], [42] but to analyse it mathematically is a very difficult task. The formation of a soliton requires a combination of the nolinearity effect and the dispersion effect of the transmission line. If either of the nonlinear components of the line, *L(I)* or *C(V)*, has a characteristic that decreases with increasing current *I* or voltage *V*, respectively, the phase velocity according to Eq.(1.1) will increase. This means that due to the nonlinearity, points closer to the peak of the current or voltage waveform will have a faster propagation (phase) velocity and produce a shockwave front as shown in the upper part of Figure 1.2. On the other hand, dispersion due to the discreteness of the NLETL causes the waveform to spread out as indicated in the lower half of Figure 1.2. The combination of both nonlinearity and dispersion leads to the formation of a soliton. A series of solitons propagating will

then result in the formation of RF pulses. Marksteiner [63] and [64] estimated that the RF efficiency from a solition generating NLETL in the absence of dissipation is close to 1/3.

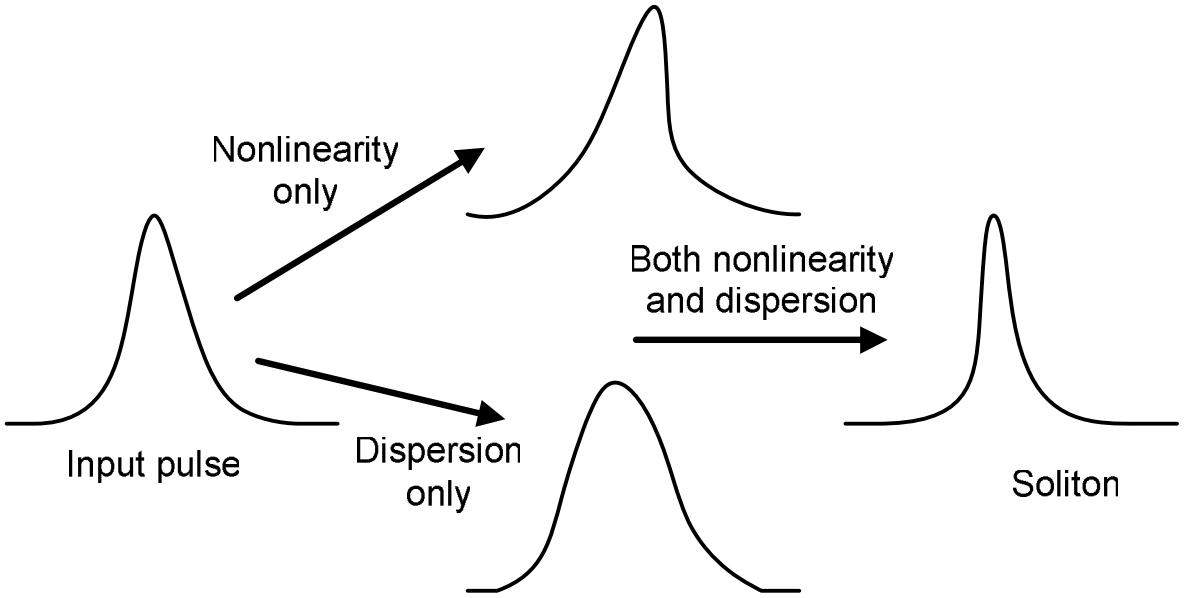

Figure 1.2 Dispersion and nonlinear effects in NLETL.

Nonetheless, it has been shown that the differential-difference equations for the NLETL can be derived by applying Kirchoff's law to the LC sections. These nonlinear equations can be combined into a higher order equation which subsequently can be reduced to the normal or modified Korteweg-de Vries (KdV) equation through a coordinate transformation [12], [13], [65]. The derivation of the KdV equation as depicted in Eq.(1.4) for a LC ladder circuit with nonlinear capacitors is illustrated in Appendix A.

$$\frac{\partial u}{\partial t} - 6u\frac{\partial u}{\partial x} + \frac{\partial^3 u}{\partial x^3} = 0\,. \tag{1.4}$$

This method of obtaining the KdV equation from a NLETL has been known to be applied to the nonlinear dielectric line and the nonlinear magnetic line [66]. More works on KdV equation can be found in [67]-[72].

The soliton formation process can be described in 3 time intervals [2]: (i) initially, the first two terms of Eq.(1.4) dominate and u steepens in regions where it has a positive slope; (ii) after u has steepened sufficiently, the third term becomes important and oscillations develop on the left of the front; (iii) each oscillation or soliton begins to move uniformly at a rate which is proportional to its amplitude. The solitons spread apart and eventually overlap spatially and interact nonlinearly. The nonlinear partial differential KdV equation can be solved analytically using the "Inverse Scattering Method" [73] and the "Direct Method" by Hirota [74]. Analytic solutions in terms of single or multiple solitons [75]-[78] can be obtained from the KdV equations. An example of a single soliton solution is shown in Eq.(1.5),

$$u(x,t) = -\frac{1}{2}a^2 \sec h^2\left[\frac{a}{2}\left(x - x_0 - a^2 t\right)\right] \tag{1.5}$$

where x_0 is the initial position and $a = \sqrt{v}$ as a function of the soliton velocity v. It is worth noting that the amplitude of the soliton pulse is proportional to the velocity of propagation and its pulse width is inversely proportional to the square root of the velocity. By assuming the solution is in the form of a "$sech^2$" function travelling wave, the details of obtaining a single-soliton solution for the KdV equation are shown in Appendix B.

It should be noted that this process of deriving the KdV equation assumes that the number of LC sections is large (in the continuum limit) and resistive losses are negligible. Furthermore, the nonlinear elements (dielectric or magnetic) have to follow a certain function that allows for a simple first order approximation and ignoring of higher order terms. Hence, the analytic solution is only good enough for understanding the basics of solitons generation and their characteristics. It could not be used to predict the exact output waveform of the NLETL with an input rectangular pump pulse. A numerical method has to be used instead to solve the system of equations

associated with the NLETL. It is with this in mind that a circuit model was developed for the NLETL in this research work so that it could be implemented numerically in any programming software. Parametric studies could then be carried out to understand the effect of each parameter variation in the NLETL.

1.2 OBJECTIVES AND CONTRIBUTION

This section describes the objectives of the research work and the contributions that the results of the research will make to the archival engineering literature. In brief, an NLETL circuit model based on circuit theory was developed for simulation and extensive parametric studies were carried out to understand the behaviour and characteristics of these lines. An innovative method for more efficient RF extraction was implemented in the NLCL and a simple novel method was also found to obtain the necessary material parameters for modeling the NLIL. Last but not least, the NLHL (where no experimental NLHL has been reported to date) was successfully demonstrated in experiment.

Most current circuit models and PSpice (Personal Simulation Program with Integrated Circuit Emphasis) models for NLETL focus on studying the rise time of the output pulse and only a handful reported having done simulations for RF generation. These simulations for RF generation do not include resistive losses and the authors do not show how well their model matched to the experimental data. The omission of the resistive element in the circuit model and the lack of validation of the model through practical experiment led to an impetus to develop an in-house NLETL circuit model. Hence, one of the objectives in the research work is to develop a generic NLETL circuit model to simulate the three types of NLETL (NLCL, NLIL and NLHL) and validate their results against experiments. The in-house NLETL model was

successfully validated with low voltage experiments before being utilized in high voltage work. The NLETL model forms the backbone of the research work as it becomes a crucial tool used in designing the high voltage lines and it helps to guide the physical implementation of the NLETL. In addition, an extensive and comprehensive parametric study using the NLETL model was carried out to understand how the parameters of the line and input pulse affect the output pulse oscillation. Literature reports on the effect of parameters change are limited and most give very brief descriptions on only a few line or input pulse parameters. Through this study, all line and input pulse parameters were investigated thoroughly, and the trends and conditions for good output oscillating pulse can now be better understood.

Another objective of the research work is to improve the extraction efficiency of the RF pulses. It is known that there is a problem with extraction when a resistor is connected to a conventional NLETL as a load. The oscillation of the pulse at the load is greatly damped and a high pass filter is needed to remove the DC content. A novel method is proposed in this thesis where direct AC extraction is possible without the need for filtering. Furthermore, the proposed method whereby the load is strategically located in the line gives better modulation depth and RF efficiency. This novel method was successfully demonstrated in the nonlinear capacitive line (NLCL) and results from the in-house NLETL model gives good match to the experimental data.

For a nonlinear inductive line (NLIL), it is reported in the open literature that a simplified form of the Landau-Lifshitz-Gilbert (LLG) equation can be used to model the dynamics of the nonlinear inductor made of ferrite. However, there is a lack of information on the critical parameters used in the LLG equation and how these parameters can be obtained. This spurs the formation of another objective which is to develop a procedure to find out the critical parameters in the simplified LLG equation

for use in the in-house NLETL model. An innovative method was eventually developed to obtain the key parameters in the LLG equation. Simulation results from the NLETL model where the LLG equation is used show very good match to the NLIL experimental data. Furthermore, a simple and quick method was also developed to obtain the characteristic L-I curve of the nonlinear inductor for use in the NLETL model. Henceforth, the curve-fit function attained for the L-I curve can also be easily implemented in PSpice software.

Last but not least is the objective to design and build a nonlinear hybrid line (NLHL). Current literature reveals that only simulation work has been done on NLHL and no experimental work has been carried out on NLHL to date. This could be due to the difficulty in getting the right combination of both nonlinear magnetic and nonlinear dielectric materials. With the help of the in-house NLETL circuit model, a NLHL was successfully constructed and tested in the research work undertaken here. Simulation results show good match to the NLHL experimental data.

1.3 ORGANIZATION

There are altogether 6 chapters in this dissertation. Following the introduction in this chapter, Chapter 2 describes the development of the NLETL circuit model which forms an essential tool in simulating the various types of NLETL (NLCL, NLIL and NLHL). In addition, the model was used to carry out a comprehensive and extensive parametric study of the NLETL. Taking reference to a NLETL with fixed parameter values, every parameter was varied to find the trend and effects on the output voltage waveform.

Chapter 3 features the implementation of the NLCL at low voltage and high voltage. The low voltage work validated the NLETL circuit model and subsequently the model was used to design the NLCL at high voltage. A proposed innovative method to directly extract the RF waveform to give better efficiency without the need for a high pass filter as compared to a conventional NLCL is described. The results obtained from the NLETL model are evaluated against the experimental data.

The design and construction of a high voltage NLIL is described in Chapter 4. A novel method to find the critical parameters of the simplified Landau-Lifshitz-Gilbert (LLG) equation for use in the NLETL model is shown. Another simple and quick method to obtain the characteristic L-I curve of the nonlinear inductor for modeling is also presented.

Chapter 5 compares the performances of a NLHL as compared to the NLCL and NLIL through simulations using the NLETL circuit model. The prospect of using the NLHL is evaluated and discussed. Subsequently, the design and implementation of a high voltage NLHL is illustrated. The experimental results are presented and discussed.

The final chapter concludes this thesis and suggests the scope for future work.

CHAPTER 2: NLETL CIRCUIT MODEL

This chapter describes the development of the nonlinear lumped element transmission line (NLETL) circuit model which forms the backbone of this research as it is used in simulating the various nonlinear lines (NLCL, NLIL and NLHL). It should be noted that even though the Korteweg-de Vries (KdV) equation for NLETL gives an analytic solution in the form of solitary waves [65], it cannot be used to predict the output waveforms. Numerical simulation has to be used instead and the NLETL circuit model provides the basis for the computation.

2.1 DESCRIPTION OF MODEL

This section describes the process of implementing and verifying a numerical model for a nonlinear lumped element transmission line (NLETL). The main goal is to establish a generic model that is flexible for making changes in the various parameters of the line and hence can be conveniently used for conducting quick parametric studies. The model is also built such that it can incorporate characteristics of nonlinear elements defined by equations or obtained via experiments, such as for example, the capacitance *C(V)* that is voltage dependent for a nonlinear capacitor and the inductance *L(I)* that is current dependent for a nonlinear inductor. The equations for these dependencies could normally be obtained from the component manufacturers. If the

capacitance versus voltage (C-V characteristic) curve and inductance versus current (L-I characteristic) curve are obtained experimentally, the data can be implemented as a look-up table or as a curve fit function in the numerical model.

The circuit diagram used for constructing the numerical model for the NLETL is depicted in Figure 2.1. Similar to the numerical techniques used for modeling pulse sharpening circuits by Turner [79], the NLETL circuit model was formulated with the addition of dissipative losses for the inductive and capacitive elements. The model comprises three parts: 1) the input that is a user-defined pump pulse or a discharge pulse from a storage capacitor, and input impedance "R_{gen}"; 2) the passive NLETL itself that comprises n number of LC sections in which each section contains a single series L connected to a single shunt C arranged in an inverted "L" shape; and 3) a load "R_{load}" that is resistive. "R_L" and "R_C" are included for losses in the inductor and capacitor, respectively.

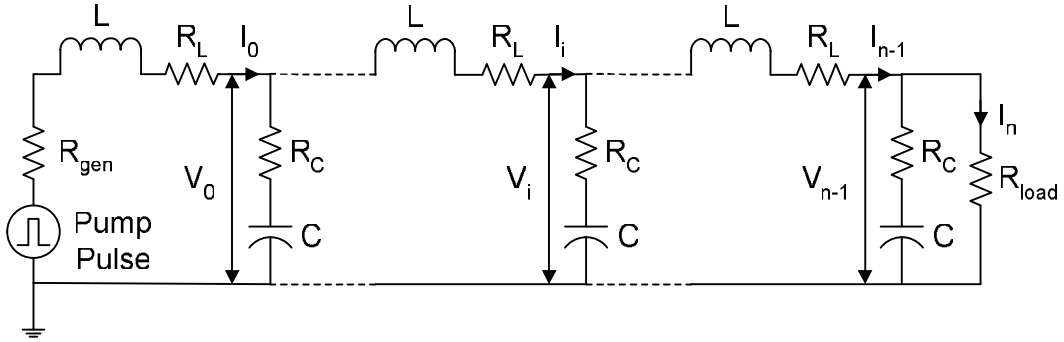

Figure 2.1 Circuit diagram of a nonlinear lumped element transmission line (NLETL).

Using Kirchoff's voltage and current laws, the equations for the 1st section of the LC ladder circuit can be obtained as follows:

$$V_{pump} = L \cdot \frac{dI_0}{dt} + V_0 + I_0 \cdot \left(R_{gen} + R_L \right) \tag{2.1}$$

$$\frac{dVc_0}{dt} = \frac{I_0 - I_1}{C} \tag{2.2}$$

$$V_0 = Vc_0 + (I_0 - I_1) \cdot R_C \quad . \tag{2.3}$$

The equations for the $(i+1)^{th}$ section are:

$$V_{i-1} = L \cdot \frac{dI_i}{dt} + V_i + I_i \cdot R_L \tag{2.4}$$

$$\frac{dVc_i}{dt} = \frac{I_i - I_{i+1}}{C} \tag{2.5}$$

$$V_i = Vc_i + (I_i - I_{i+1}) \cdot R_C \quad . \tag{2.6}$$

The equations for the final loop at the load are:

$$\frac{dVc_{n-1}}{dt} = \frac{I_{n-1} - I_n}{C} \tag{2.7}$$

$$V_{n-1} = Vc_{n-1} + (I_{n-1} - I_n) \cdot R_C \tag{2.8}$$

$$V_{n-1} = I_n \cdot R_{load} \quad . \tag{2.9}$$

For the nonlinear elements of the line, i.e. nonlinear capacitor and nonlinear inductor, their values are functions of voltage and current respectively, and are user-defined in the form of a mathematical expression or empirical look-up table:

$$C = f(V) \tag{2.10}$$

$$L = f(I) \, . \tag{2.11}$$

where

V_{pump} *– input voltage pump pulse*

Vc_i *– voltage across capacitor at* $(i+1)^{th}$ *section*

V_i *– voltage at* $(i+1)^{th}$ *node*

I_i – current flowing in inductor at $(i+1)^{th}$ section

n – number of LC sections

i – index ranging from 0 to (n-1)

C – capacitance as a function of voltage

L – inductance as a function of current.

The NLETL circuit model was implemented as a system of ordinary differential equations (ODE) using the MathCad software and the numerical solver used is the 4^{th}-order Runge Kutta method.

To test the validity of the model, a low voltage nonlinear capacitive line was first constructed and the experimental results are compared with the simulated ones from the NLETL circuit model. The details of the experiments are documented in Chapter 3. The results from the NLETL circuit model are in very good agreement with the ones from the experiments. An example to show the good matching of the output waveforms for a rectangular pump pulse of amplitude 5 V, duration 400 ns, and rise time 10 ns that is input into a 10-section line with constant $L = 1$ μH and nonlinear C as defined in Eq.(2.12) [80] is illustrated in Figure 2.2. R_{gen} and R_{load} are taken as 50 Ω. R_C and R_L are 2.0 Ω and 0.16 Ω, respectively.

$$C(V) = C_0 \cdot \left[b + (1-b) \cdot e^{\frac{-V}{a}} \right] \tag{2.12}$$

where $C_0 = 816.14$ pF, $a = 2.137$ V and $b = 6.072 \times 10^{-3}$.

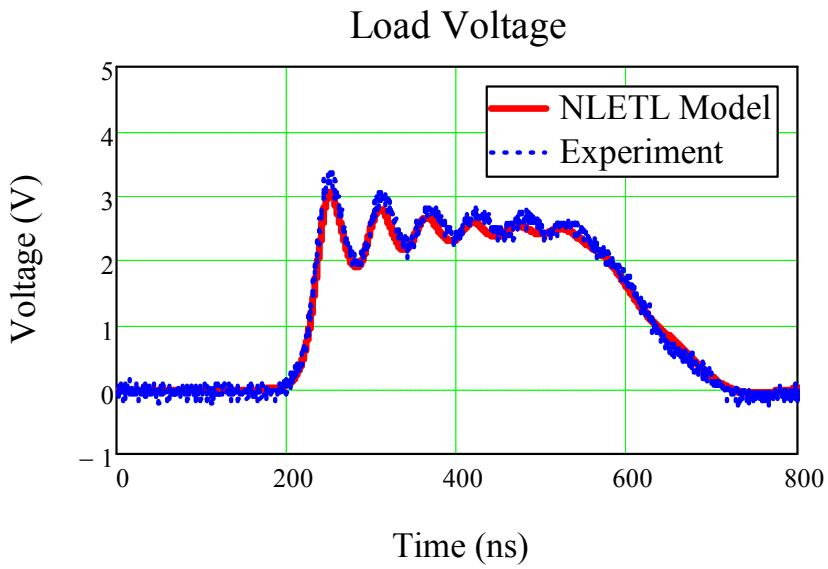

Figure 2.2 Comparison of output waveforms from the NLETL circuit model and experiment.

2.2 PARAMETRIC STUDIES

Having verified that the NLETL circuit model can predict waveforms that closely matched the experimental results, parametric studies using the model were subsequently conducted to understand the trend and effects by varying the parameters of the line. As a starting point, the parameters used for producing the waveform in Figure 2.2 as given in Section 2.1 will be used as reference values. For each parametric study, only one parameter will vary while the others will remain unchanged. The effect of each parameter change is elaborated in subsequent subsections. Subsections 2.2.1 to 2.2.6 refer to nonlinear capacitive lines while subsection 2.2.7 refers to a nonlinear inductive line. To avoid cluttering only 3 or 4 cases are plotted for the load voltage simulations to be shown.

2.2.1 INPUT RECTANGULAR PULSE

2.2.1.1 Rise Time

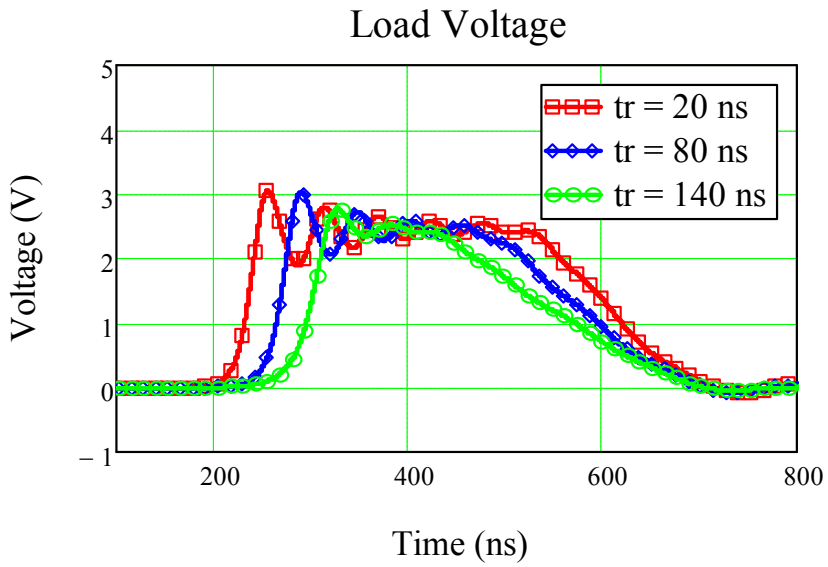

Figure 2.3 Effect of input pulse rise time t_r on output load voltage.

Here the rise time and fall time of the input pulse are taken to be the same. It is also maintained that the reduction in rise time ΔT as indicated in Eq.(2.13) and rise time t_r are such that $\Delta T >> t_r$ so that solitons are generated instead of simply pulse sharpening occurring [43].

$$\Delta T = n \cdot \left(\sqrt{LC(V_{\min})} - \sqrt{LC(V_{\max})} \right) \tag{2.13}$$

The rise time t_r is varied from 20 ns to 200 ns in steps of 20 ns and the effect on the output load voltage is shown in Figure 2.3. It is observed that once the line is capable of producing solitary waves, the frequency of the oscillations remain the same as the rise time varies. However, the number of oscillations decreases as the rise time increases because pulse duration being constant, the portion of the flat top reduces as the rise time increases, thus limiting the number of cycles for the same frequency.

2.2.1.2 Pulse Duration

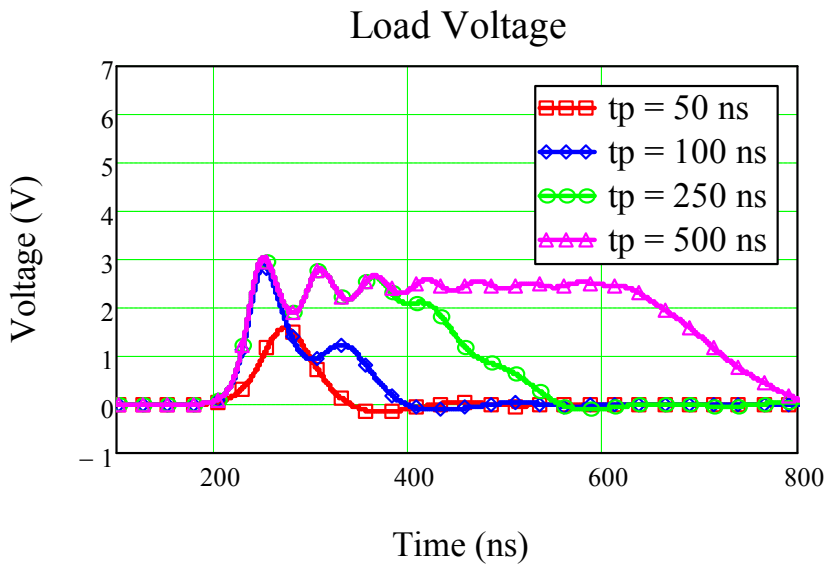

Figure 2.4 Effect of input pulse duration t_p on output load voltage.

The pulse duration t_p is varied from 50 ns to 500 ns in steps of 50 ns and the effect on the output load voltage is shown in Figure 2.4. It is observed that a minimum duration is needed to initiate oscillations and as the duration increases, the frequency of oscillation remains the same, but the oscillation amplitudes continue to decay.

2.2.1.3 Pulse Amplitude

The pulse amplitude *amp* is varied from 1 V to 10 V in steps of 1 V and the effect on the output load voltage is shown in Figure 2.5. It is observed that a low amplitude pulse will not generate any oscillations as the nonlinear capacitance *C(V)* does not vary much with small voltages applied. Too large an amplitude will cause the oscillations to shift upwards, ultimately resulting in distortions which are due to load reflections. Generally, as the amplitude increases, the frequency of oscillations also increases.

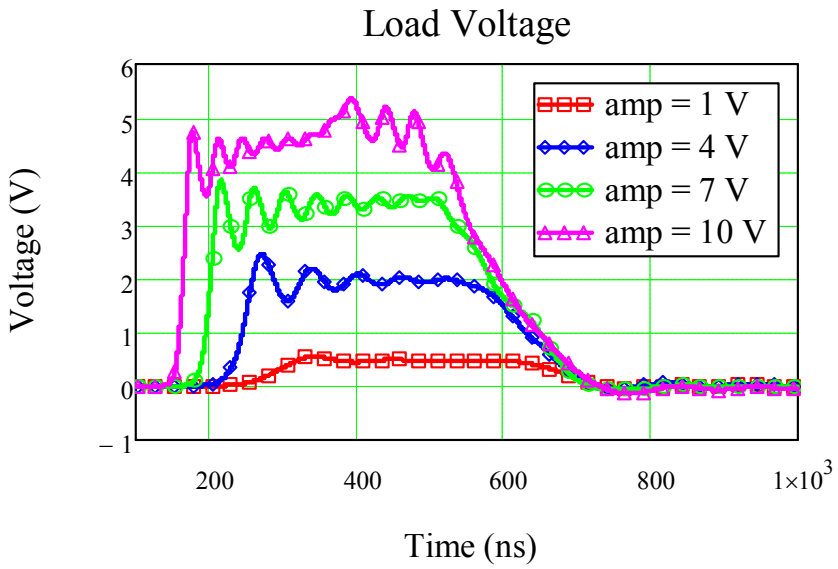

Figure 2.5 Effect of input pulse amplitude *amp* on output load voltage.

2.2.2 NUMBER OF SECTIONS

The number of LC sections *n* is varied from 5 to 50 in steps of 5 and the effect on the output load voltage is shown in Figure 2.6. It is observed that the frequency of oscillations stays approximately the same for all cases, but there is an optimum number of sections where the number of oscillations is greatest. As the number of sections increases, the fall time of the output pulse increases (i.e. the tail lengthens) and the oscillations shift downwards following the tail; the peak voltage also correspondingly decreases.

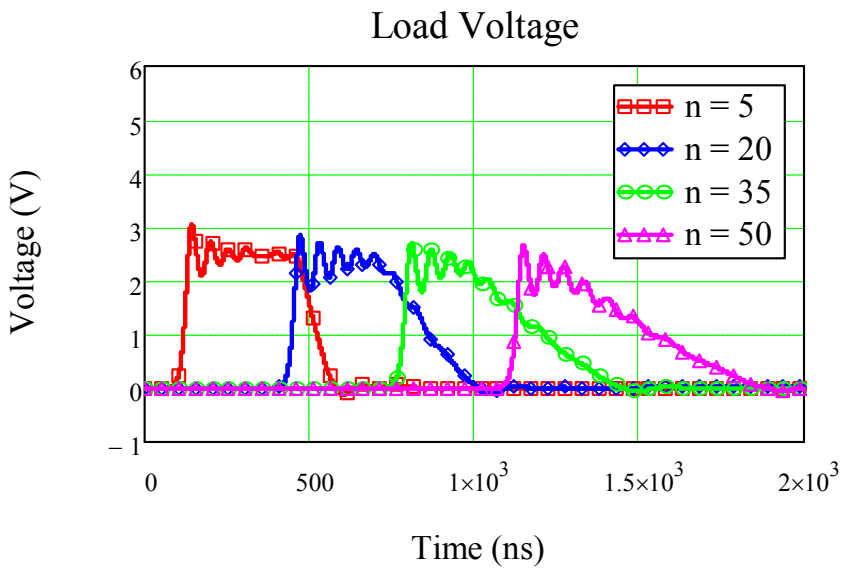

Figure 2.6 Effect of the number of LC sections *n* on output load voltage.

2.2.3 VALUE OF RESISTIVE LOAD

The value of the resistive load R_{load} is varied from 100 Ω to 1000 Ω in steps of 100 Ω and the effect on the output load voltage is shown in Figure 2.7. It is observed that the peak voltage and the peak-to-trough oscillation amplitudes increase as the load value increases. However, there is an optimum point at which the peak power is maximum and this occurs at R_{load} = 700 Ω, as depicted in Figure 2.8. It could be considered that the changing impedance of the nonlinear capacitive line is best matched to the load at this value. The frequency of oscillations increases as the load resistance increases and approaches the Bragg's frequency limit of the line. Distortion also sets in at the end of the pulse for a large load resistance.

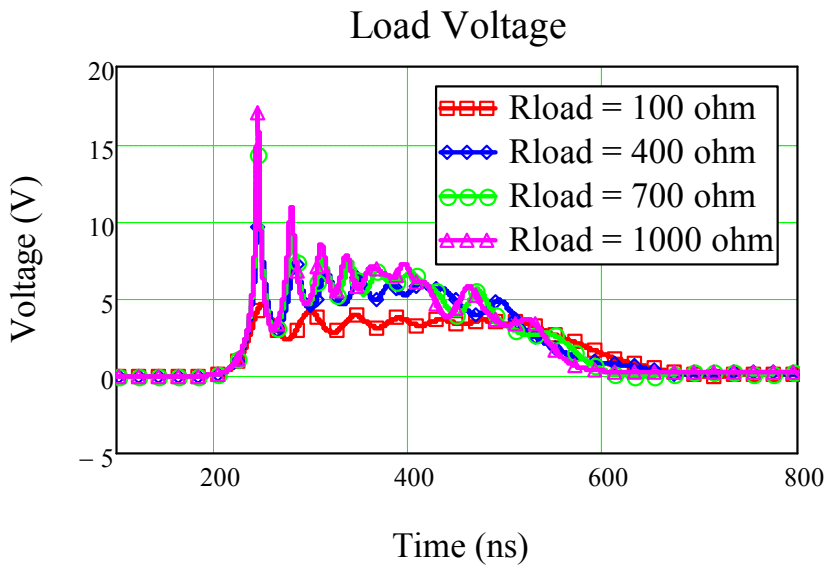

Figure 2.7 Effect of resistive load R_{load} on output load voltage.

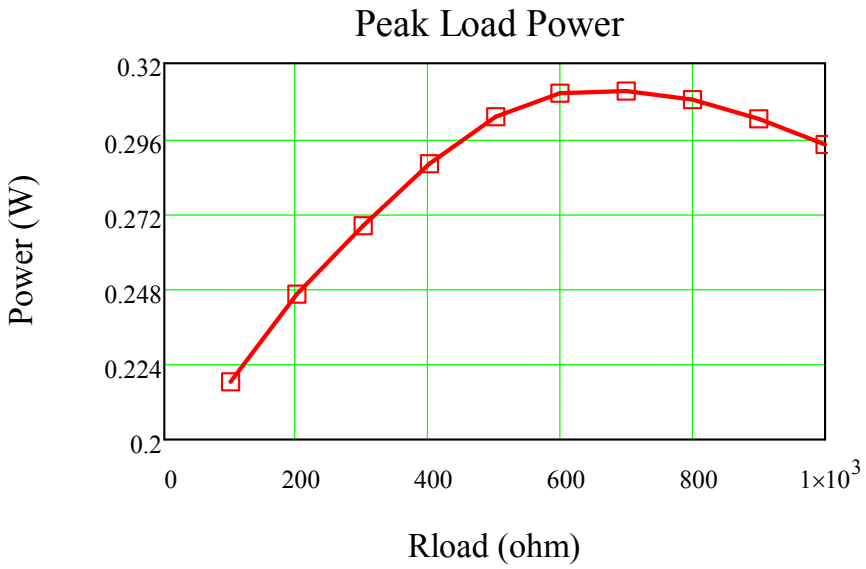

Figure 2.8 Peak power as a function of R_{load}.

2.2.4 VALUE OF RESISTIVE LOSSES

2.2.4.1 Dissipation in Resistor R_L

The value of resistor R_L is varied from 1 Ω to 10 Ω in steps of 1 Ω and the effect on the output load voltage is shown in Figure 2.9. It is observed that as R_L increases, the peak-to-trough oscillation amplitudes decrease and at high value of R_L,

oscillations start to diminish. The DC value of the pulse also decreases for higher value of R_L because for the same input voltage, the current in R_L decreases as R_L increases and, hence, a smaller current will flow in the load resulting in a lower output voltage.

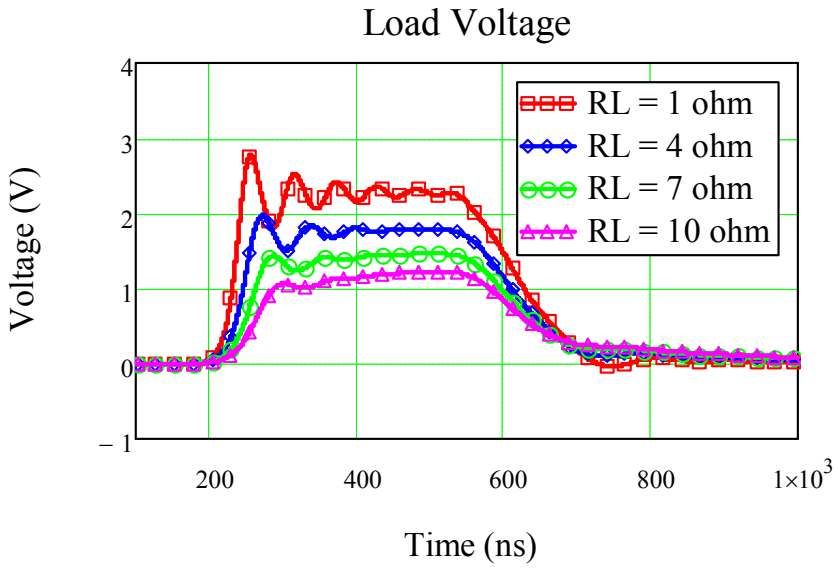

Figure 2.9 Effect of resistor R_L on output load voltage.

2.2.4.2 Dissipation in Resistor R_C

The value of resistor R_C is varied from 1 Ω to 10 Ω in steps of 1 Ω and the effect on the output load voltage is shown in Figure 2.10. Similar to the case of R_L, as R_C increases, the peak-to-trough oscillation amplitudes decrease and at high value of R_C, oscillations start to diminish. However, the DC value of the pulse remains unchanged for varying R_C value. This shows that R_C only attenuates the AC component of the inductor current that charges or discharges the nonlinear capacitor.

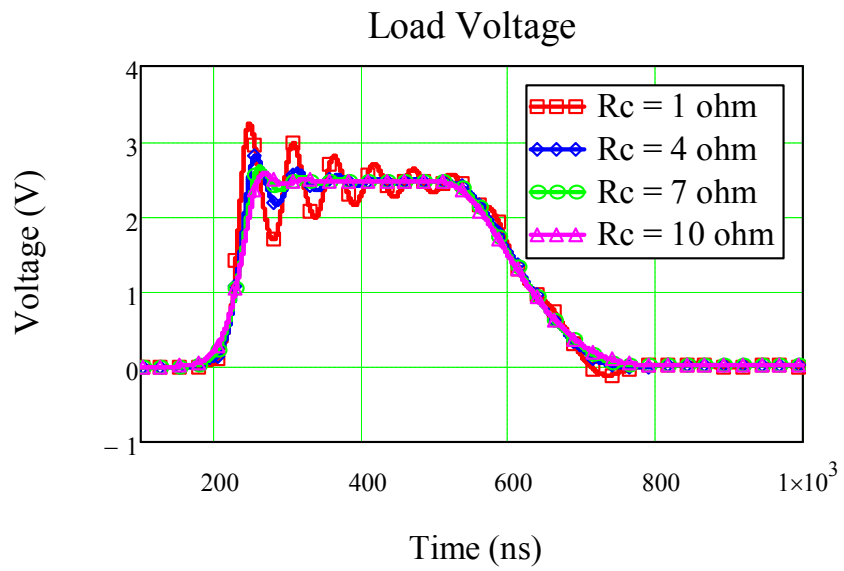

Figure 2.10 Effect of resistor R_C on output load voltage.

2.2.5 VALUE OF INDUCTOR

The value of the inductor L is varied from 0.2 μH to 2.0 μH in steps of 0.2 μH and the effect on the output load voltage is shown in Figure 2.11. It is observed that at low value of L, there are no oscillations (agrees with the observation in [80]) and the output pulse appears in staggered steps.

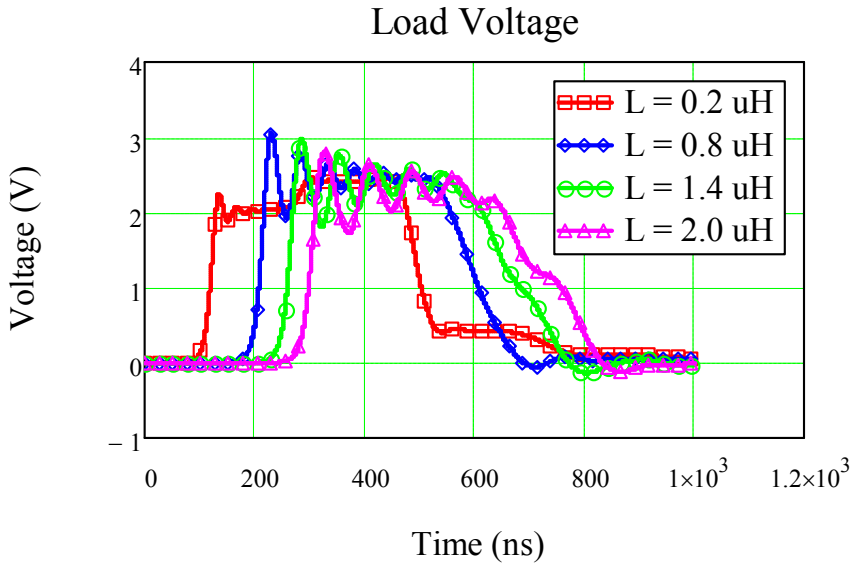

Figure 2.11 Effect of constant inductor L on output load voltage.

Oscillations start at higher value of L and there is an optimum point at which the peak power is maximum and this occurs at L = 1.0 μH as depicted in Figure 2.12. It could be considered that the load is best matched to the changing impedance of the nonlinear capacitive line at this value. The frequency of oscillations decreases as L increases.

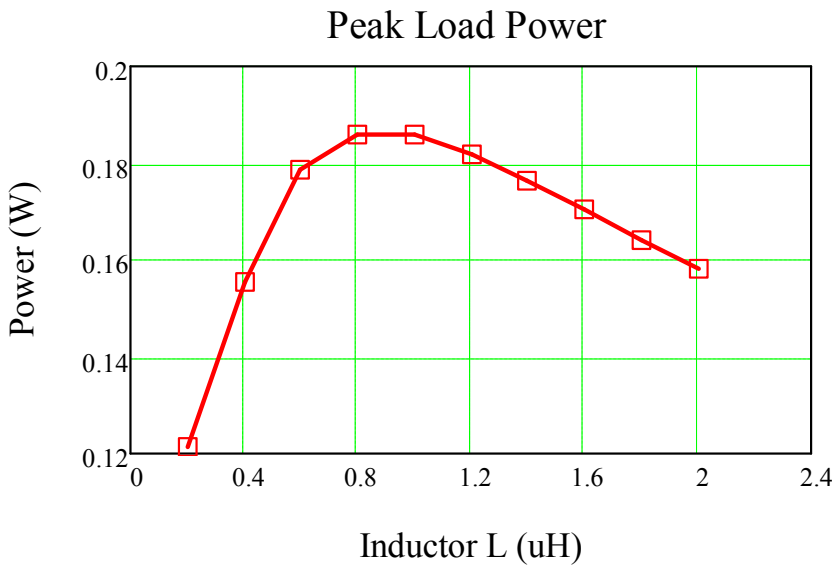

Figure 2.12 Peak power as a function of L.

2.2.6 NONLINEARITY OF CAPACITOR

The equation used for the nonlinear capacitor is shown in Eq.(2.12). The nonlinearity factor a determines the steepness of the nonlinear capacitance whereas the nonlinearity factor b determines the final capacitance as the voltage approaches infinity and lies in the range $0 < b < 1$.

2.2.6.1 Nonlinearity Factor *a*

The value of nonlinearity factor a is varied from 0.5 to 5.0 in steps of 0.5 and the effect on the output load voltage is shown in Figure 2.13. A low value of a indicates steep nonlinearity of the capacitance. At very steep nonlinearity for a = 0.5 to

1.5, the output pulses oscillate at high frequencies but with distortion. For a = 2.0 to 5.0, normal sinusoidal oscillations appear and the frequency decreases with increasing a (less steepness). It is observed that there is an optimum point at which the peak power is maximum and this occurs at a = *2.5*, as depicted in Figure 2.14.

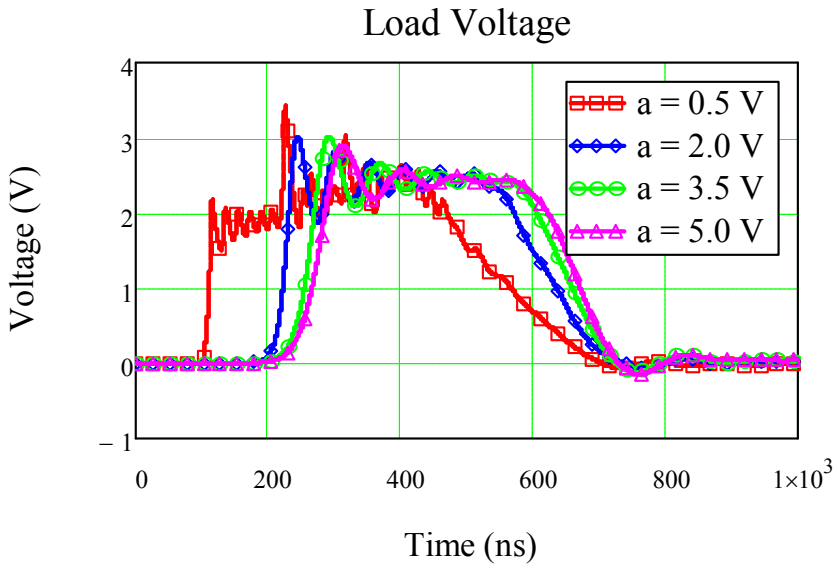

Figure 2.13 Effect of capacitive nonlinearity factor a on output load voltage.

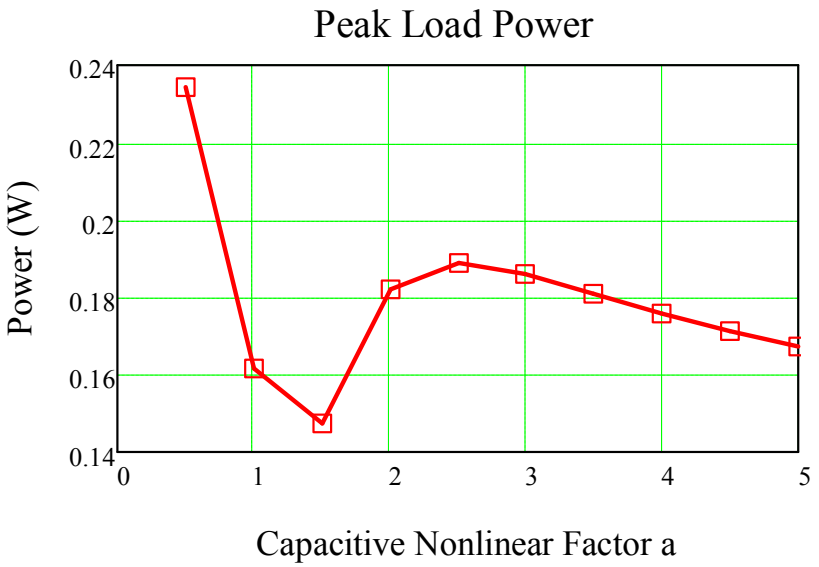

Figure 2.14 Peak power as a function of capacitive nonlinearity factor a.

2.2.6.2 Nonlinearity Factor *b*

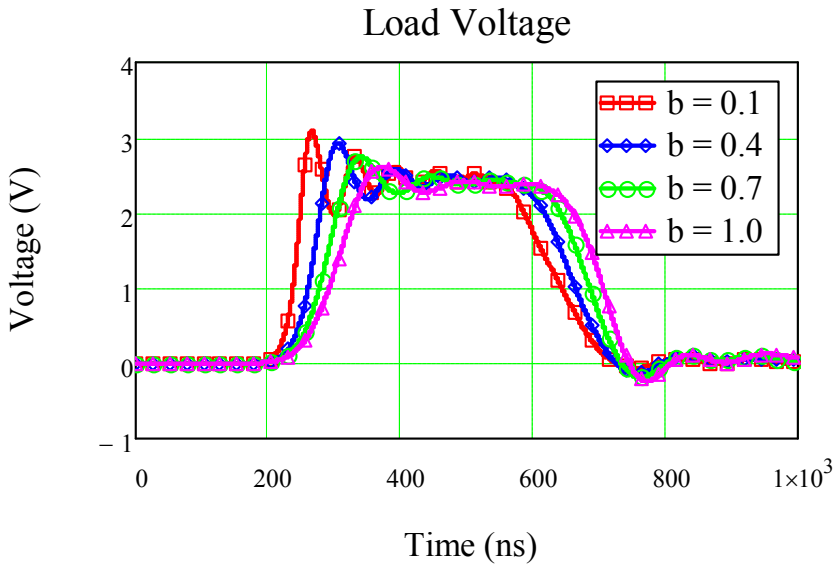

Figure 2.15 Effect of capacitive nonlinearity factor *b* on output load voltage.

The value of the factor *b* is varied from 0.1 to 1 in steps of 0.1 and the effect on the output load voltage is shown in Figure 2.15. A low value of *b* indicates low final capacitance and hence implies steep nonlinearity of the capacitance. As the value of *b* increases (less steep), both the amplitude and frequency of oscillations decrease as well. The peak power also decreases correspondingly. It should be noted that when *b* = *1*, the capacitance becomes a constant.

2.2.7 NONLINEARITY OF INDUCTOR

In order to investigate a nonlinear inductive line with a constant capacitance, a nonlinear inductor equation is adopted from [43] where it is modified so as to have a smoothly varying inductance function that approaches an asymptotic value as the current increases. This will better emulate the actual inductor when it saturates. The modified nonlinear equation for the inductor is shown as

$$L(I) = (L_0 - L_S)\left[1 - \tanh^2\left(\frac{I}{I_S}\right)\right] + L_S \tag{2.14}$$

where

L_0 – *initial inductance (at zero current)*

L_S – *asymptotic inductance with current increase*

I – *current flowing through inductor*

I_S – *inductive nonlinearity factor.*

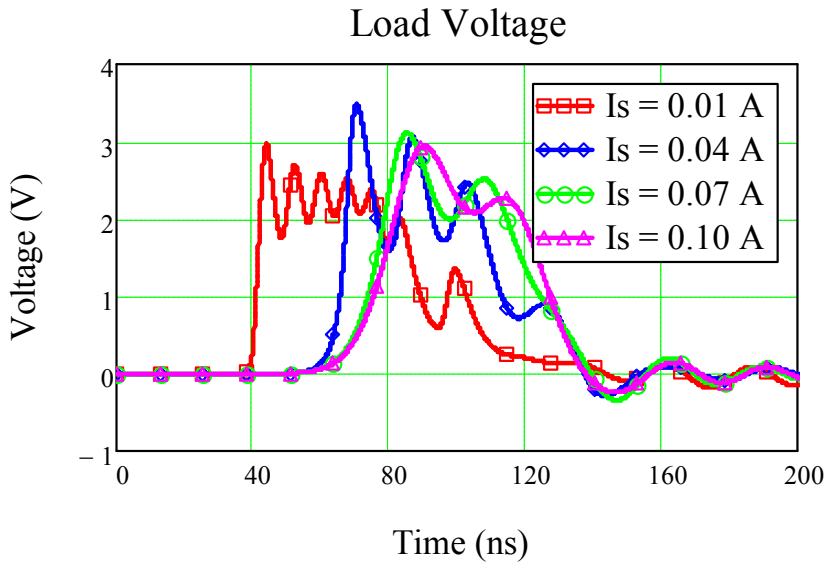

Figure 2.16 Effect of inductive nonlinearity factor I_S on output load voltage.

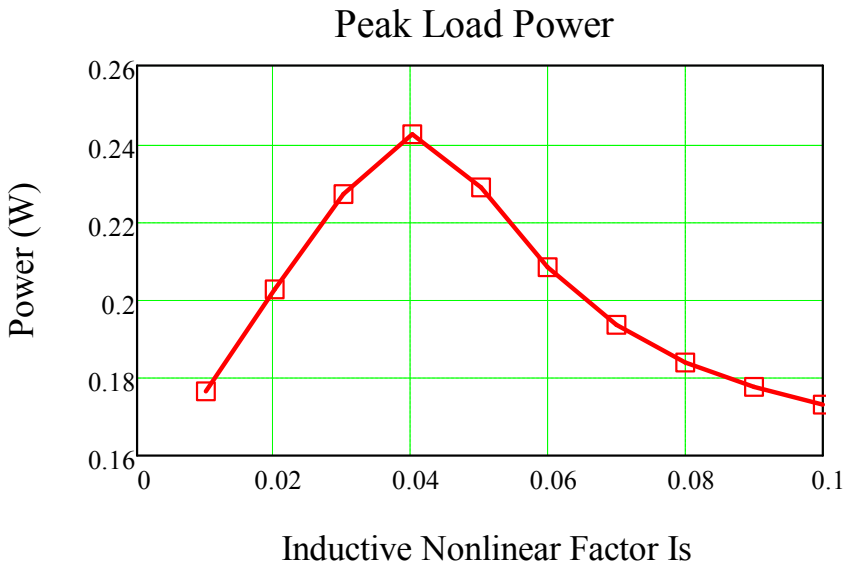

Figure 2.17 Peak power as a function of inductive nonlinearity factor I_S.

In this study, the values of the parameters in Eq.(2.14) are taken as L_0 = 500 nH and L_s = 50 nH. The other line parameters are similar to those in Section 2.1 but with an input pulse duration of 50 ns, C = 100 pF, and R_C = 0.2 Ω. The value of the nonlinearity factor I_S is varied from 0.01 A to 0.10 A in steps of 0.01 A and the effect on the output load voltage is shown in Figure 2.16. A low value of I_S indicates steep nonlinearity of the inductance. As I_S increases (less steepness), the frequency of oscillation decreases but there appears to be an optimum point at which the peak power is maximum and this occurs at I_S = *0.04* A depicted in Figure 2.17.

2.3 SUMMARY OF PARAMETERIC STUDIES

The results of the parametric studies are summarized in Table 2.1 where the effects and trends on each parameter variation are tabulated.

Table 2.1 Summary of Parametric Studies on NLETL.

S/N	Parameter	Effect on Frequency (*freq*)	Remarks
1	**Input Rectangular Pulse** a) Rise Time, t_r	increase t_r → *freq* remain approx. constant	increase t_r, → no. of oscillations decreases
	b) Pulse Duration, t_d	increase t_d → *freq* remain approx. constant	minimum duration needed to initiate oscillations
	c) Pulse Amplitude, *amp*	increase *amp* → *freq* increases	too large an amplitude will cause the oscillations to shift upwards resulting in distortions
2	**No. of Sections, *n***	increase *n* → *freq* remain approx. constant	increase *n*, → increase fall time → oscillations shift downwards, following the tail → peak voltage decreases
3	**Resistive Load, R_{load}**	increase R_{load} → *freq* increases	increase R_{load}, → oscillation amplitudes increase → optimum point where peak power is maximum (load best matched to changing line impedance)
4	**Resistive Losses** a) Loss in Inductor, R_L	increase R_L → *freq* decreases	increase R_L, → oscillation amplitudes decrease → DC value of pulse decreases (for same input voltage, current in R_L decreases, hence smaller current flow in load resulting in lower voltage)

	b) Loss in Capacitor, R_C	increase $R_C \rightarrow$ *freq* decreases	increase R_C, $\rightarrow$ oscillation amplitudes decrease $\rightarrow$ DC value of pulse remains unchanged (R_C only attenuates the AC component of the inductor current)
5	**Linear Inductor, *L***	increase $L \rightarrow$ *freq* decreases	▪ no oscillations at low value of L ▪ optimum point where peak power is maximum
6	**Nonlinearity of Capacitor** $C(V) = C_0 \cdot \left[b + (1-b) \cdot e^{\frac{-V}{a}} \right]$ a) Nonlinearity Factor *a*	increase "*a*" $\rightarrow$ *freq* decreases	▪ low "*a*" indicates steep nonlinearity ▪ at low "*a*", output pulses oscillate at high frequency but with distortion ▪ optimum point where peak power is maximum
	b) Nonlinearity Factor *b*	increase "*b*" $\rightarrow$ *freq* decreases	▪ low "*b*" indicates steep nonlinearity ▪ increase "*b*", $\rightarrow$ oscillation amplitudes decrease $\rightarrow$ peak power decreases
7	**Nonlinearity of Inductor** $L(I) = (L_0 - L_S)\left[1 - \tanh^2\left(\frac{I}{I_S}\right)\right] + L_S$ nonlinearity factor I_S	increase $I_S \rightarrow$ *freq* decreases	▪ low I_S indicates steep nonlinearity ▪ increase I_S, $\rightarrow$ optimum point where peak power is maximum

2.4 CONCLUSIONS

A circuit model has been developed and described for a nonlinear lumped element transmission line (NLETL). This NLETL model has been used to extensively investigate the effects of various parameters changes of the NLETL. It is observed that an optimum point exists in peak load power for certain parameter combinations. Even though a steep nonlinearity of the nonlinear L or C elements and small values of constant L or C elements could result in high frequency oscillations, they could also cause distortion to the output oscillations. As the impedance of the NLETL changes with time due to the nonlinear elements, it is difficult to find the value of the resistive load to match to the line. However, a parameter sweep can be simulated using the NLETL model to find the load value that gives the best match in terms of maximum peak load power.

CHAPTER 3: NONLINEAR CAPACITIVE LINE (NLCL)

This chapter showcases the implementation of low voltage and high voltage nonlinear capacitive lines (NLCLs). For ease of reference and clarity, the phase velocity v_p, Bragg frequency f_B, and characteristic impedance Z_0 of the line are reproduced here from Section 1.1.3 in Eqs. (3.1), (3.2) and (3.3) respectively; but in this case, the inductor is linear and the inductance is taken as a constant L.

$$v_p = \frac{1}{\sqrt{L \cdot C(V)}} \tag{3.1}$$

$$f_B = \frac{1}{\pi \cdot \sqrt{L \cdot C(V)}} \tag{3.2}$$

$$Z_0 = \sqrt{\frac{L}{C(V)}} \tag{3.3}$$

3.1 LOW VOLTAGE NLCL

This section presents a low voltage nonlinear capacitive line (NLCL) that was designed and built using reverse-biased varactor diodes as the nonlinear elements to generate RF pulses. Frequency control of the line was demonstrated by using a simple biasing circuit. Two different configurations of connecting capacitive NLETLs were also implemented to study the quality of the RF oscillations.

3.1.1 DESCRIPTION OF LOW VOLTAGE NLCL

To demonstrate the generation of RF oscillations using a NLETL, a nonlinear capacitive line (NLCL) was built with commercial-off-the-shelf (COTS) components. The circuit diagram for setting up the experiment is illustrated in Figure 3.1 where the capacitor *C* is nonlinear and the inductor *L* is constant.

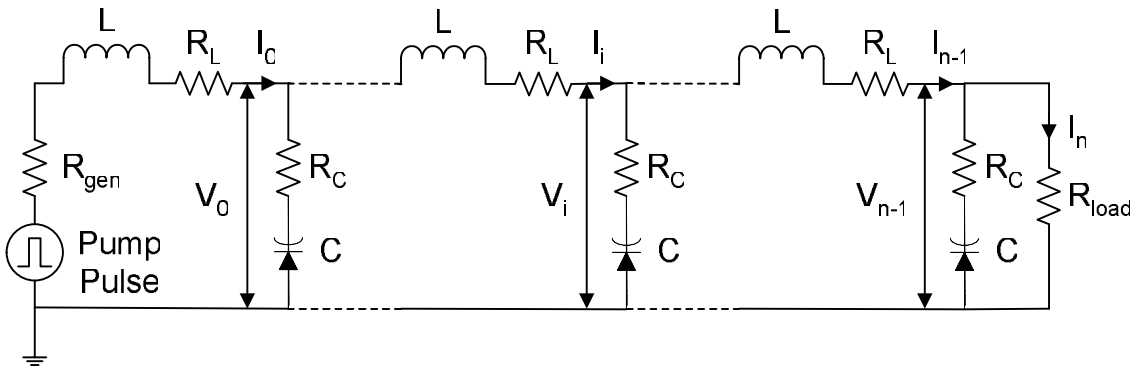

Figure 3.1 Circuit diagram of a nonlinear capacitive line (NLCL).

The nonlinear capacitors were implemented using Sanyo SVC388 hyper-abrupt junction type silicon composite varactors operated in the reverse-bias mode. They are twin type varactor diodes meant for AM electronic tuning applications and have a high capacitance ratio that offers steep nonlinearity for the capacitance. Only one of the pairs in each module is used in constructing the line. The characteristic capacitance versus reverse voltage (C-V) profile given by the manufacturer is shown by the blue dotted line in Figure 3.2. A curve fitting was performed using Eq.(3.4) [80] where it was subsequently utilized in the NLETL circuit model. For best fit, the parameters in the equation were obtained as follows: $C_0 = 816.14\ pF$, $a = 2.137\ V$ and $b = 6.072 \times 10^{-3}$. The curve fitting line is depicted as the red solid line in Figure 3.2.

$$C(V) = C_0 \cdot \left[b + (1-b) \cdot e^{\frac{-V}{a}} \right] \tag{3.4}$$

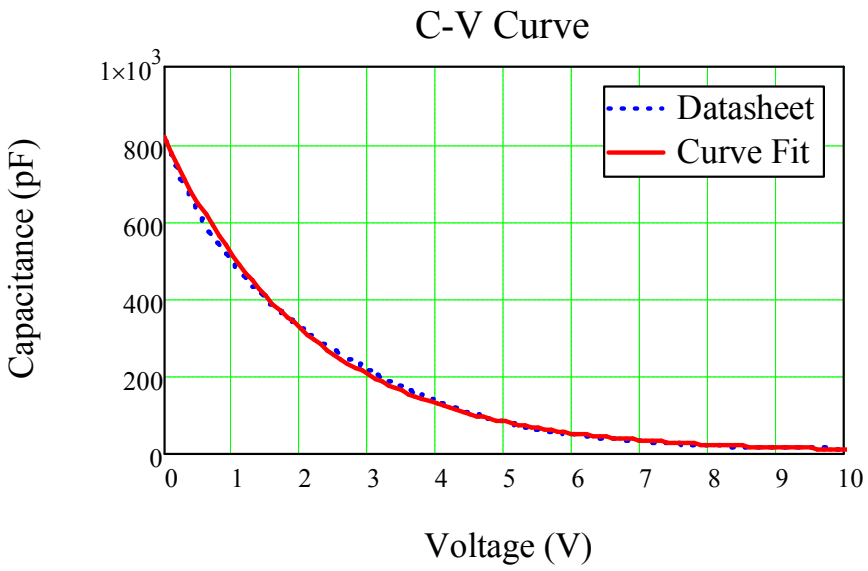

Figure 3.2 Characteristic curve of a SVC388 diode.

In general for NLCL, the COTS nonlinear capacitor was first selected based on the largest nonlinearity among those surveyed. The selected Sanyo SVC388 varactor diodes have capacitance ratio of 18.5; subsequently, inductors of 1 μH were chosen to give the operating frequency in the 10s MHz range. The constant value inductors *L* were implemented using EPCOS *1* μH BC series RF chokes with ferrite drum core. The line was then optimized by performing a parameter sweep on the load to find the load value that gives the maximum peak power.

The input pump pulse was produced using an Agilent 33250A function generator. The input pulse has amplitude of 5 V, duration 400 ns with rise and fall time of 10 ns. The number of LC sections for the NLCL is $n = 10$. The input impedance R_{gen} and load impedance R_{load} are both 50 Ω. The resistances of the inductors and capacitors are $R_L = 0.16$ Ω and $R_C = 2.0$ Ω, respectively. A photograph of the experimental set-up is shown in Figure 3.3. The experimental waveforms for the input and output of the line are shown in Figure 3.4 and they verified the results predicted by the NLETL model. The node voltage at each section of the line was also measured and

all the node voltages indicated good match to the simulated ones. Voltage measurements are made with Lecroy PP007-WR voltage probes and the data are captured on Lecroy WaveRunner 6050 oscilloscope that has a bandwidth of 500 MHz. Examples of two such node voltage measurements are shown in Figure 3.5.

Some interesting phenomena were observed on the phases of the node voltage at the capacitors and the currents in the inductors. The adjacent node voltages (preceding node and subsequent node voltages) for a particular node are approximately 180 degrees out of phase to the voltage at that node. The current in each inductor is approximately 90 degree out of phase to the node voltages at either of its ends. These phenomena are a result of the discrete nature of the line where lumped *L* and *C* components are being used. Energy is passed from inductor to capacitor in a step-by-step manner and appears to propagate in a "bucket-brigade" mode as described by P. W. Smith [81]. He also investigated load reflection on a short circuited NLCL whereby the number of pulses in the voltage waveform increases as the stage number decreases. He attributed this observation to the fact that at the penultimate stage, the reflected wave is delayed from the incident wave by the delay of one line section.

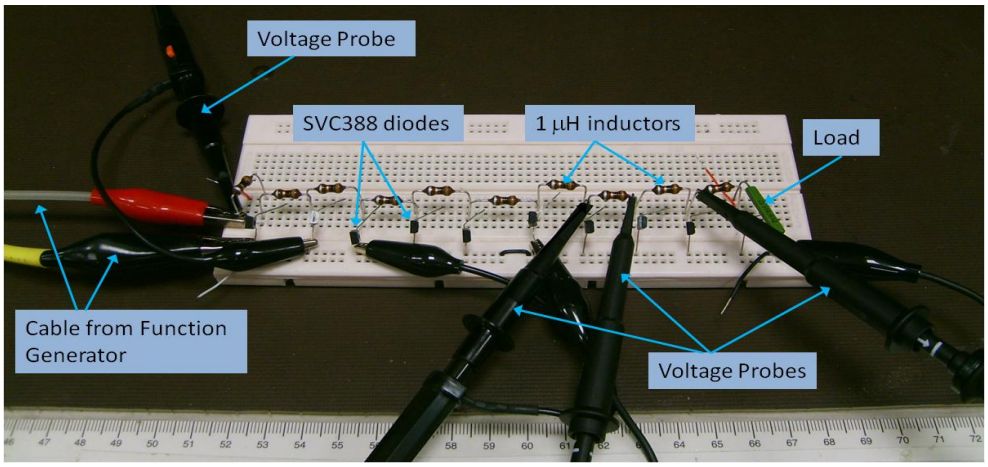

Figure 3.3 Photograph of a typical experimental set-up for a 10-section low voltage NLCL.

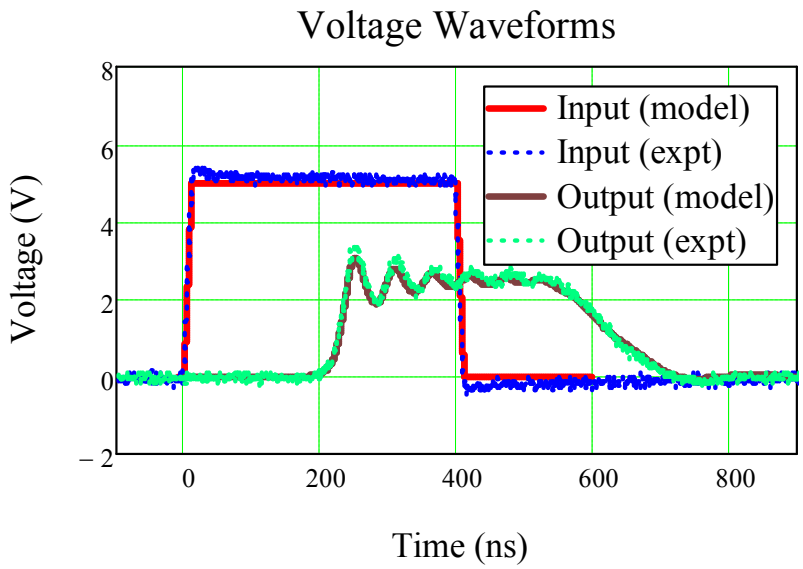

Figure 3.4 Input and output waveforms for the NLETL circuit model and experiment (V_{pump} = 5 V, n = 10, R_{load} = 50 Ω).

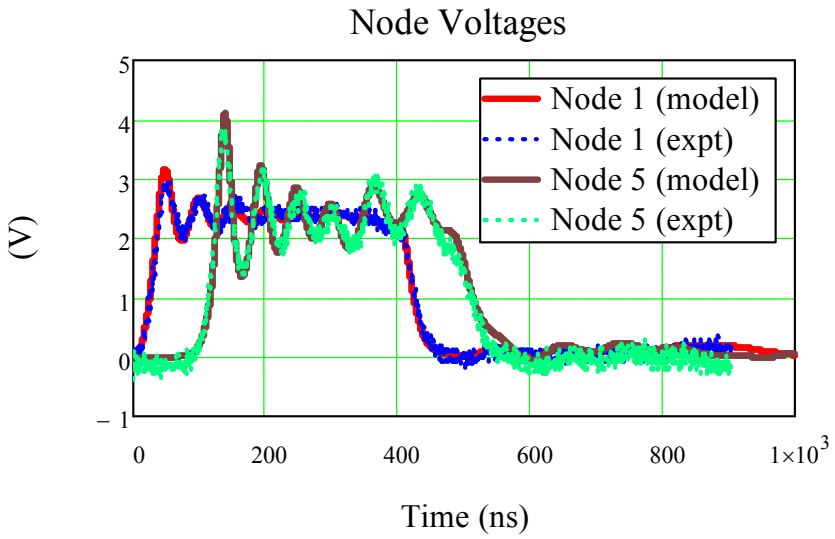

Figure 3.5 Node voltages at Node 1 and Node 5 for NLETL circuit model and experiment (V_{pump} = 5 V, n =10, R_{load} = 50 Ω).

In order to find the load that best matched to the line in terms of peak power, a parameter sweep on the load was performed using the NLETL simulation model. The corresponding simulation result is depicted in Figure 3.6 and indicates a maximum peak load power at around R_{load} = *700* Ω. To test the effect of using a higher load

value, the load was increased by a factor of 10 to $R_{load} = 500\ \Omega$ in the experiment. The load voltage measured is shown in Figure 3.7. It matches very well to what is predicted by the NLETL model.

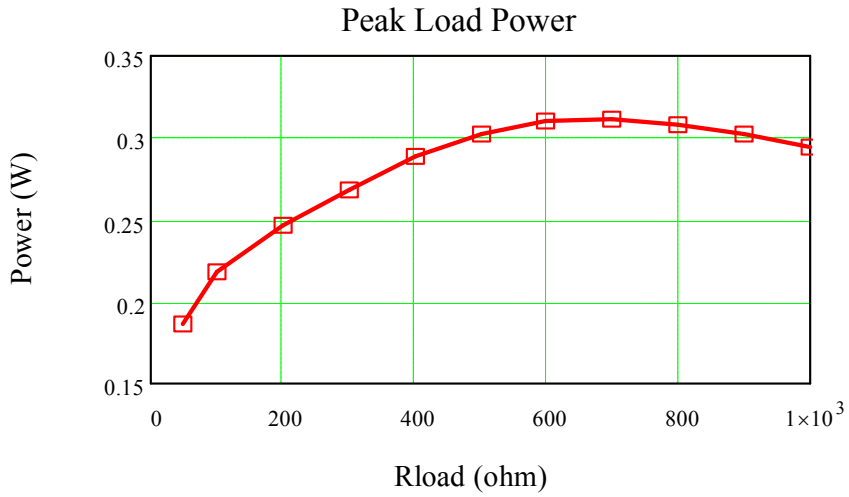

Figure 3.6 Peak power vs. R_{load} (V_{pump} = 5 V, n = 10).

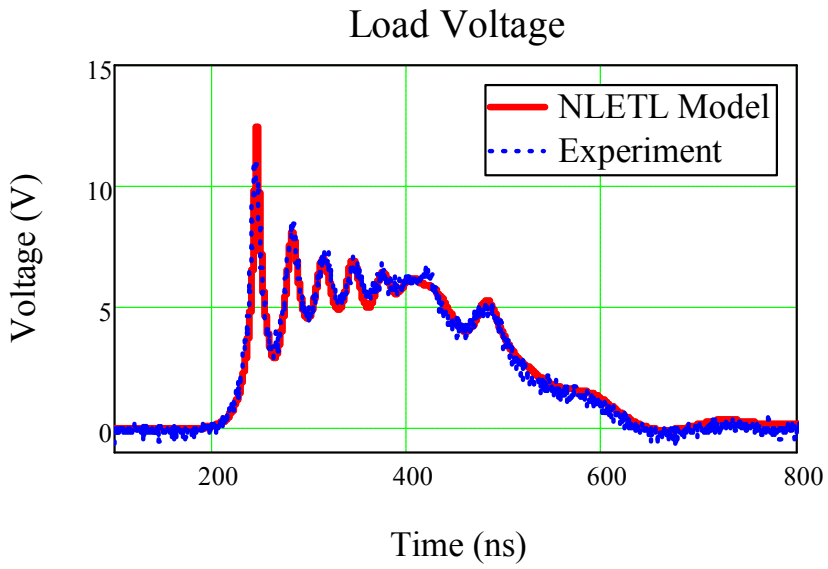

Figure 3.7 Output load voltage for NLETL circuit model and experiment (V_{pump} = 5 V, n = 10, R_{load} = 500 Ω).

It is of interest to understand how the frequency of the oscillations changes with time rather than performing fast fourier transform (FFT) on the output voltage pulse. The frequency of each cycle in the oscillations is calculated and plotted against the time when the cycle ends. This time-frequency plot can also show the number of cycles of oscillations by simply counting the number of points plotted.

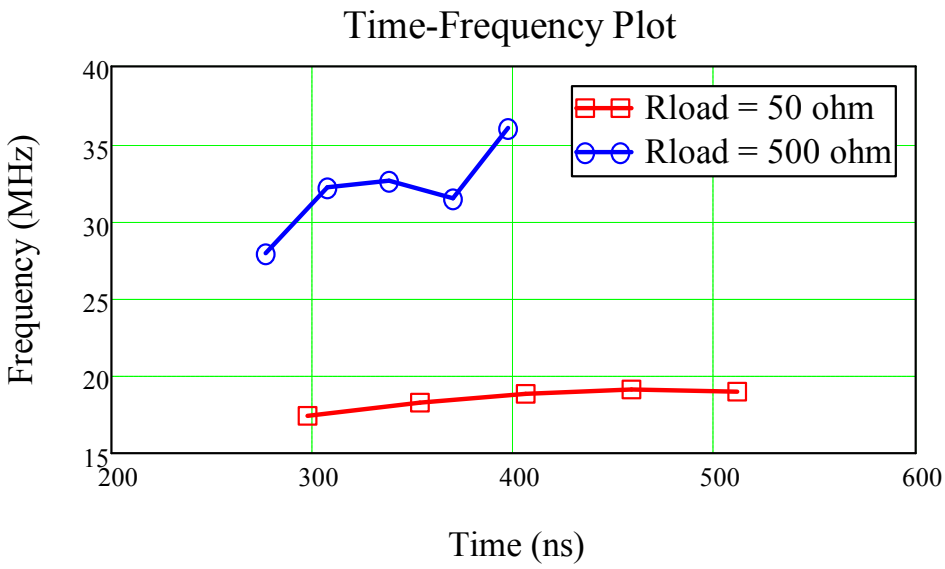

Figure 3.8 Voltage oscillation frequency vs. time for R_{load} = 50 Ω and R_{load} = 500 Ω (V_{pump} = 5 V, n = 10).

Time-frequency plots for the cases where R_{load} = 50 Ω and R_{load} = 500 Ω are depicted in Figure 3.8. It is observed that both cases have 5 cycles of oscillation and the frequency is higher for higher load value. This can be explained by the fact that for a transmission line, the voltage across the load and voltages along the line will increase as the resistive load value increases. (This was observed in the parametric study on varying the load value in Section 2.2.3.) Consequently, the capacitance of the line will decrease with increasing voltage as shown in Figure 3.2. Hence, according to Eq.(3.2), the oscillation frequency will increase with lowering *C(V)* values. The higher voltages

along the line due to higher load values are attributed to the positive reflection coefficient as $R_{load} > Z_0$. The reflected voltages propagate back on the line and add on to the incident voltages resulting in higher total voltages. It is noted that the frequency of oscillations is not truly monochromatic and tends to increase with time.

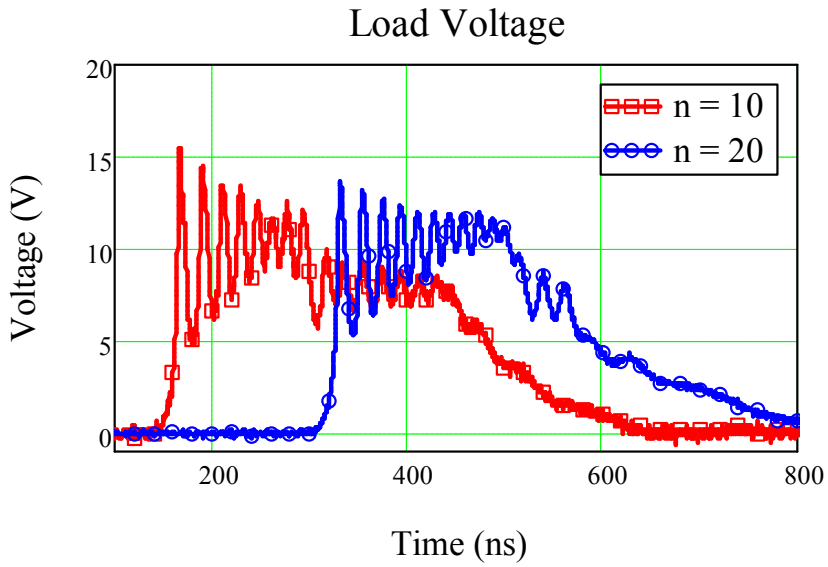

Figure 3.9 Experiment: output load voltage for n = 10 and n = 20 (V_{pump} = 10 V, R_{load} = 200 Ω).

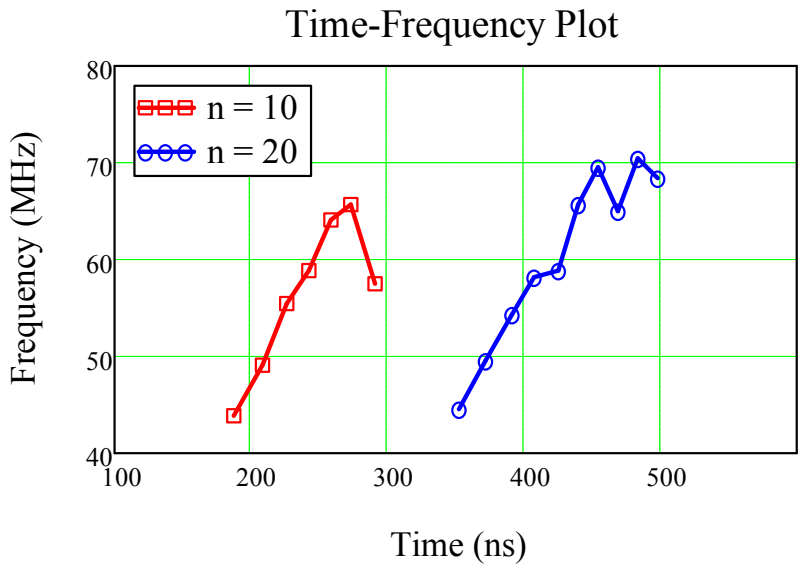

Figure 3.10 Experiment: voltage oscillation frequency vs. time for n =10 and n = 20 (V_{pump} = 10 V, R_{load} = 200 Ω).

Experiments were also carried out with higher amplitude input pump pulse and larger number of LC sections. The cases where input pulses of 10 V were injected into 10-section and 20-section lines with 200 Ω loads are shown in Figure 3.9 (the other parameters remain the same as before). It is expected that the output pulse appears later at about *300* ns for the 20-section line as every additional LC section introduces a time delay. The time-frequency plots for the two lines are compared in Figure 3.10. Both lines have oscillation frequencies within 45 to 70 MHz and their frequencies generally increase with time. The 10-section line has 7 cycles of oscillation (not counting the cycles in the later part of the pulse which appeared disjointed due to load reflections) whereas the 20-section has 10. Hence, the NLETL with larger number of LC sections can have more cycles of oscillation, but at the cost of a slight decrease in the peak amplitude of the pulses.

3.1.2 FREQUENCY CONTROL OF NLCL

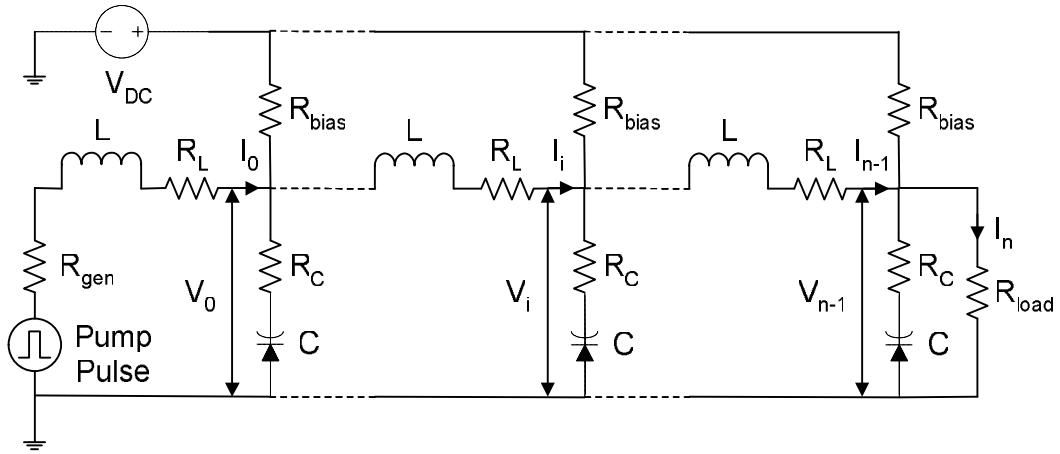

Figure 3.11 Nonlinear capacitive line (NLCL) with resistive biasing circuit.

To illustrate the ease of tuning the NLCL to produce waveforms of different frequencies, a simple biasing circuit consisting of a DC voltage source and a parallel network of resistors (R_{bias} = *5.1* kΩ) was added to the line as shown in Figure 3.11. In this experiment, the DC voltage source was adjusted until the biasing voltages at the nonlinear capacitors (varactors) reached the desired value. For demonstration of frequency tuning, the bias voltage V_{bias} at the capacitors was varied from 0 to 2.5 V. At each bias voltage, a 5 V pulse was pumped into a 10-section line connected to a 500 Ω load. For prediction of output waveform, the NLETL circuit model was expanded to include the biasing circuit. The simulated results from the NLETL model showed very good match to the experimental waveforms; an example of the comparison at V_{bias} = *1* V is depicted in Figure 3.12.

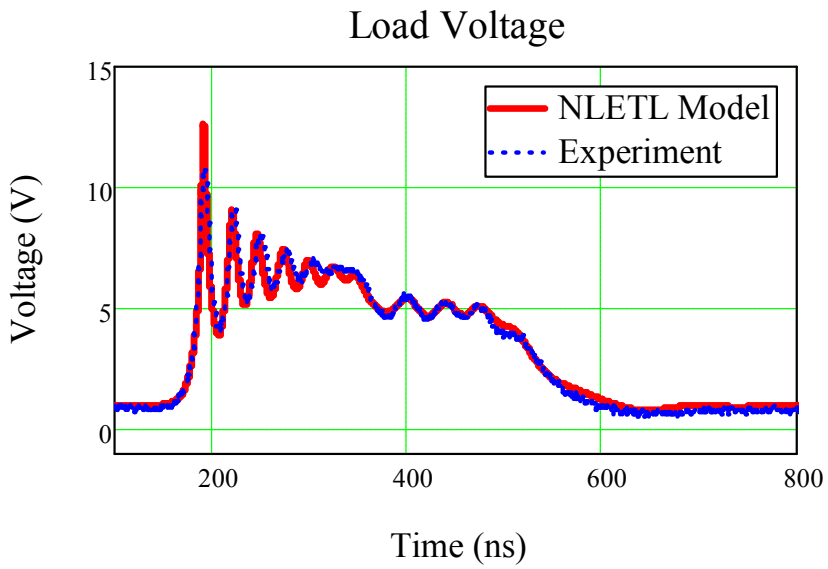

Figure 3.12 Output load voltage for NLETL circuit model and experiment at V_{bias} = 1.0 V (V_{pump} = 5 V, n = 10, R_{load} = 500 Ω).

The output load voltage waveforms for the various bias voltages are shown in Figure 3.13. It is observed that the output pulse appears earlier at higher bias voltage but the time at which the pulse starts to decrease and the fall rate remain about the same regardless of the bias voltage. The time-frequency plot in Figure 3.14 reveals that the frequency of oscillations can be tuned from 25 MHz to 55 MHz when V_{bias} is varied from 0 to 2.5 V. This demonstrates the wide frequency tunability of the NLETL. It is also noticed that the number of cycles in the oscillation is the same (5 cycles) for all cases of biasing but the range of frequency is larger at higher biasing voltage.

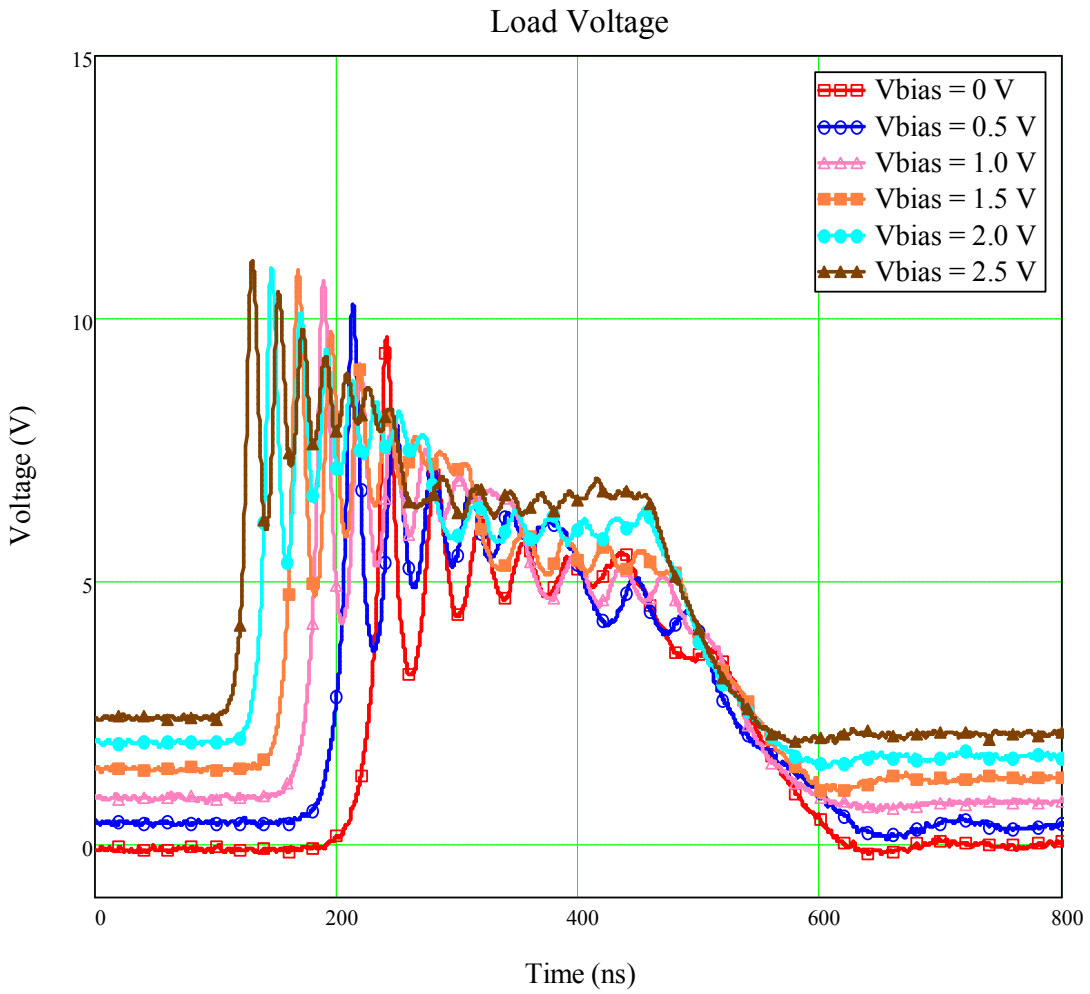

Figure 3.13 Experiment: Output Load Voltages for V_{bias} = 0 to 2.5 V (V_{pump} = 5 V, n = 10, R_{load} = 500 Ω).

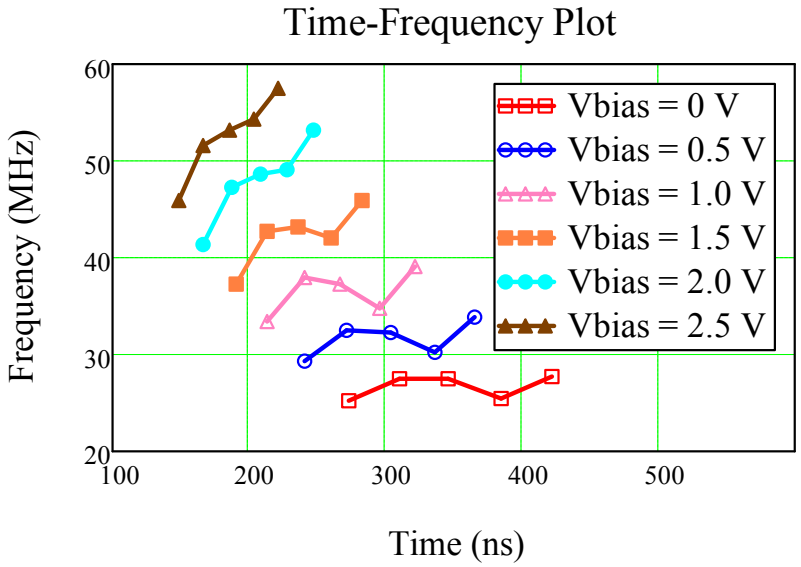

Figure 3.14 Experiment: Voltage Oscillation Frequency vs. Time for V_{bias} = 0 to 2.5 V (V_{pump} = 5 V, n = 10, R_{load} = 500 Ω).

3.1.3 VARIATION OF NLCLs

This section describes the experiments carried out on two configurations of NLETLs based on nonlinear capacitors with the aim of obtaining greater output oscillation amplitudes.

3.1.3.1 Two Parallel Lines

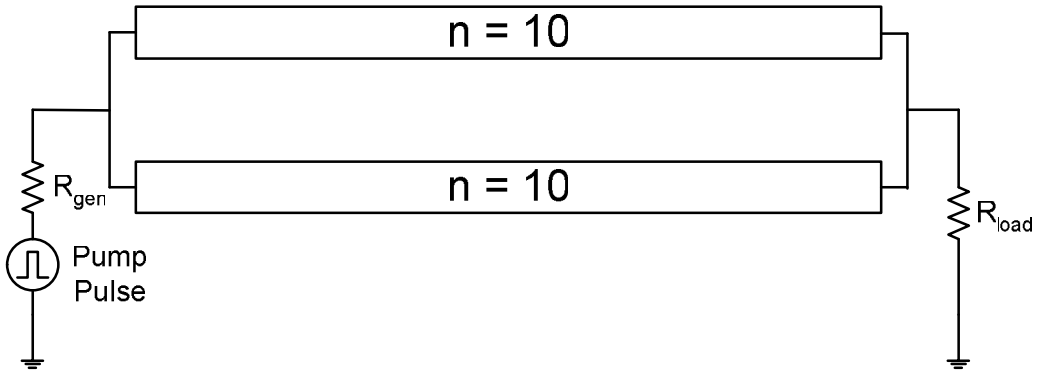

Figure 3.15 Two NLETLs in parallel: each with number of sections n = 10.

By making use of the soliton property whereby the joint amplitude of two colliding solitons is greater than the sum of the amplitudes of the two solitons [13]-[15], two NLETLs can be connected in parallel to achieve this effect as shown in Figure 3.15.

A demonstration using two parallel nonlinear capacitive lines (NLCLs) each with 10 LC sections was carried out using an input pump pulse of 10 V and a load of 200 Ω. The output load voltage of the two parallel lines is compared to that of a single line in Figure 3.16.

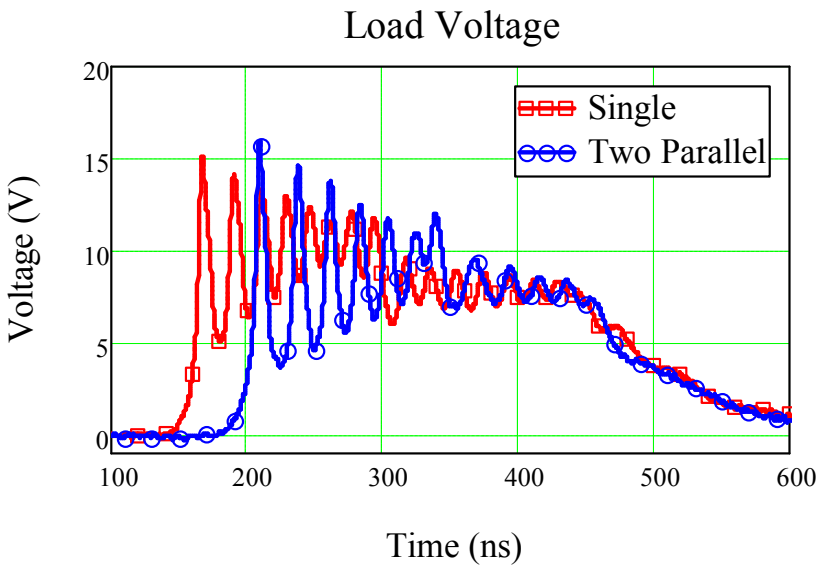

Figure 3.16 Experiment: output load voltages for single NLCL and two parallel NLCLs (V_{pump} = 10 V, n = 10, R_{load} = 200 Ω).

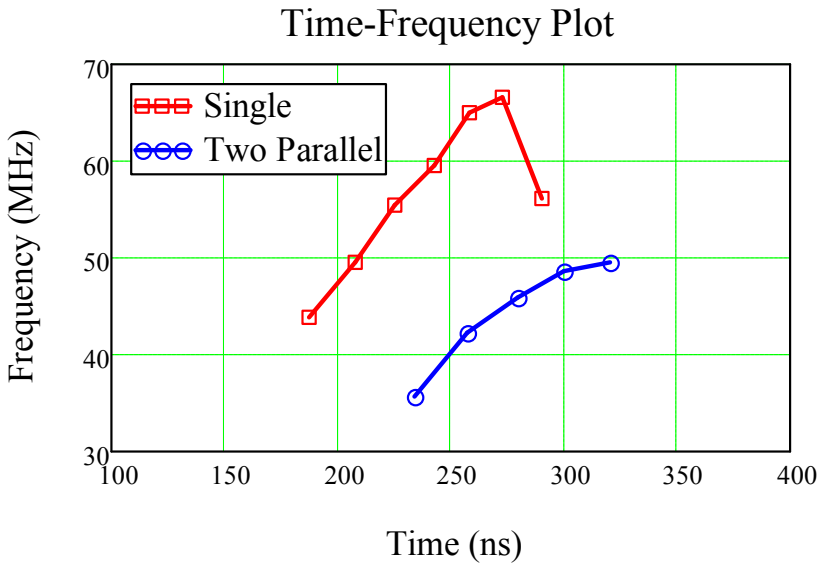

Figure 3.17 Experiment: voltage oscillation frequency vs. time for single NLCL and two parallel NLCLs (V_{pump} = 10 V, n = 10, R_{load} = 200 Ω).

It is observed that the oscillation amplitudes are indeed higher in the two parallel lines than in the single line. However, this result comes with a compromise as the oscillation frequencies drop from 45-65 MHz for the single line to 35-50 MHz for the two parallel lines as seen in the time-frequency plot in Figure 3.17. Consequently,

the number of oscillation cycles is fewer in the two parallel lines due to the lower frequencies. The drop in frequency is due to the power from the single source being distributed to the two parallel lines. The voltage and current oscillations in each of the two parallel lines are less than those in a single line. From the characteristic C-V curve in Figure 3.2, the smaller voltage swing will result in a larger capacitance value. Hence, according to the Bragg frequency in Eq.(3.2), lower oscillating frequency will be produced. However, at the load, the sum of the lower voltages from each of the two parallel lines yields a higher voltage than that of a single line.

3.1.3.2 Asymmetric Parallel Lines

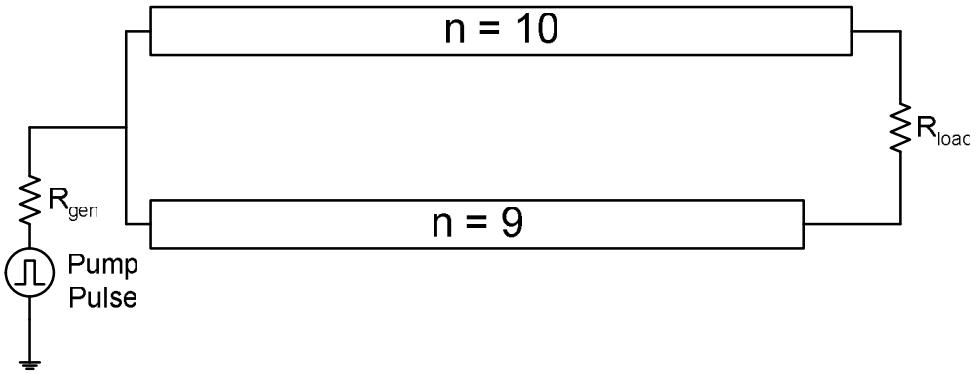

Figure 3.18 Asymmetric parallel (ASP) NLETL [80] with number of sections n = 10 and n = 9.

By utilizing the property of NLCLs whereby the voltage waveforms of alternate sections are in anti-phase, the asymmetric parallel (ASP) line was proposed in [80] to obtain waveforms with greater oscillation amplitudes. The diagram of an ASP line using a 10 LC section line in parallel with a 9 LC section line is depicted in Figure 3.18. Experiments were carried out using input pump pulses of 5, 8 and 10 V into a 200 Ω load. Two voltage probes were used to measure the voltage at node 10 of the first line and node 9 of the second line (with respect to ground). The output load

voltages were taken as the difference between the two probe measurements and are shown in Figure 3.19. As expected, the oscillation amplitudes are higher for higher pump pulse voltages since the nonlinearity of capacitors are fully utilized. The oscillation frequencies also increase as the pump pulse voltage increases, as indicated in the time-frequency plot in Figure 3.20.

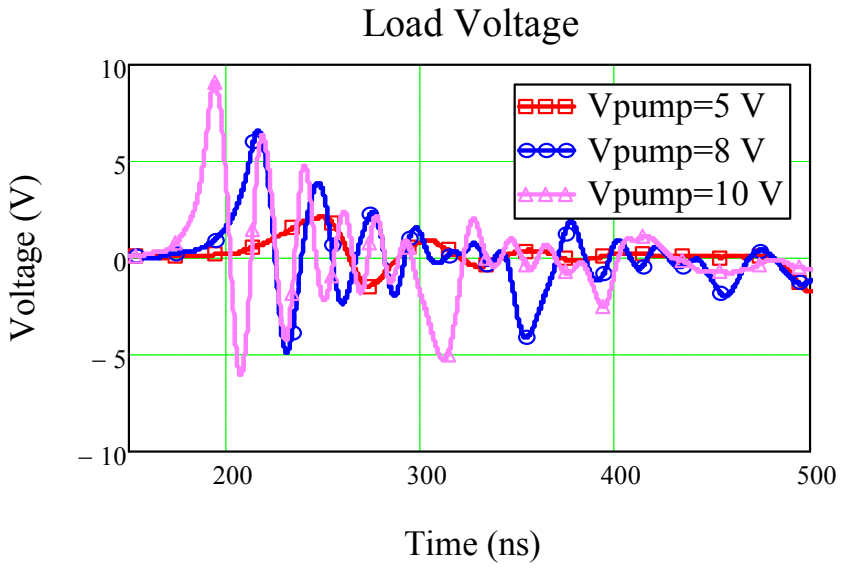

Figure 3.19 Experiment: output load voltages for ASPL for V_{pump} = 5, 8 and 10 V (n1 = 10, n2 = 9, R_{load} = 200 Ω).

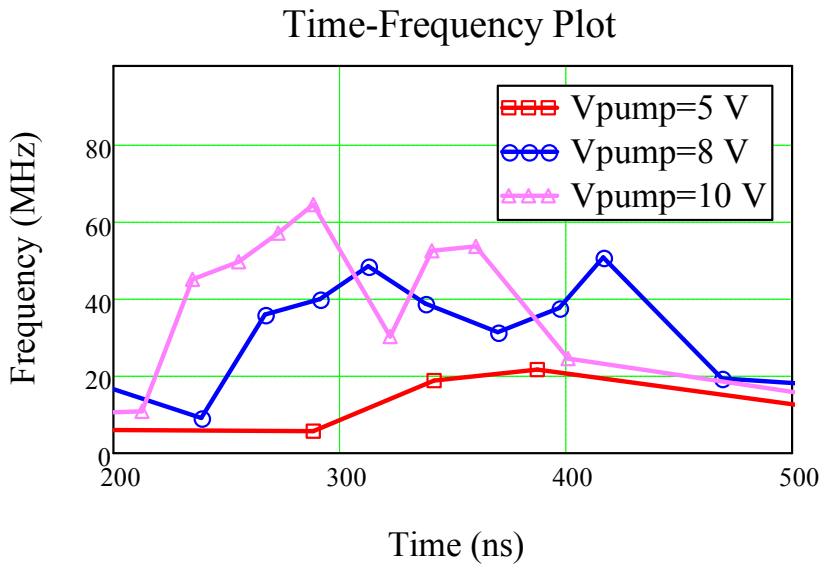

Figure 3.20 Experiment: voltage oscillation frequency vs. time for ASPL for V_{pump} = 5, 8 and 10 V (n1 = 10, n2 = 9, R_{load} = 200 Ω).

3.2 HIGH VOLTAGE NLCL

This section describes experimental work carried out in building and testing a high voltage NLCL using COTS components. The design of the NLCL was made possible by using an NLETL circuit model developed Section 2.1 that is well validated with experiments in Section 3.1. Results from the NLETL model show good match to the data obtained from the experiments described in this section. In order to study the quality of the output oscillating pulses, the voltage modulation and the frequency content of the pulses are carefully analyzed. A refined definition of voltage modulation depth (VMD) is proposed and a time-frequency plot is used to better differentiate the cycles in the oscillations. A novel method is also proposed to directly extract the AC component of the output signal as compared to a conventional single NLETL [41]-[44] where a decoupling capacitor needs to be used. The use of a decoupling capacitor or high-pass filter in series with the load often results in decreasing the efficiency of the line. The new RF extraction method proposed here placed the load across the last inductor of the LC ladder results in better performance in terms of power and voltage modulation compared to the conventional method where the load is placed across the last capacitor of the LC ladder. A biasing circuit is added to this proposed line to demonstrate the ability to tune the output frequency.

3.2.1 DESCIPTION OF HIGH VOLTAGE NLCL

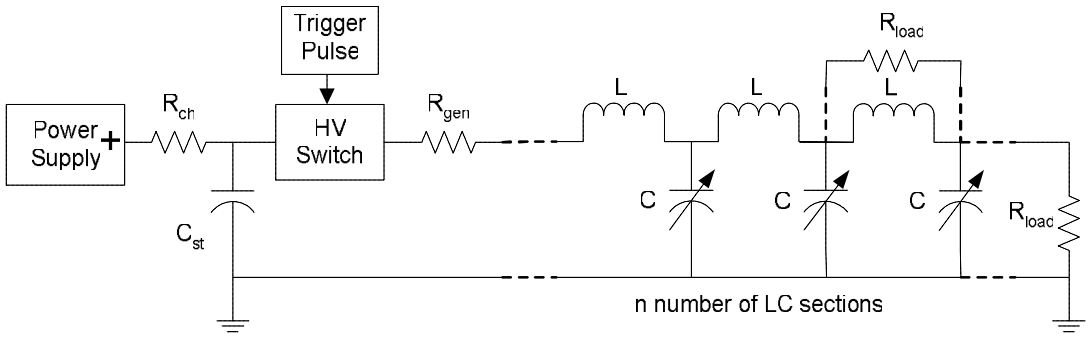

Figure 3.21 Experimental setup of the NLCL with possible R_{load} attachment across the capacitor or across the inductor.

The NLCL whose circuit diagram for setting up the experiment is illustrated in Figure 3.21 was built using COTS components. It describes two possible configurations: a) one with a resistive load R_{load} placed across the capacitor in the last section of the LC ladder network as in a conventional line and b) a proposed new method of placing the resistor R_{load} across the inductor. The results and analyses of both configurations will be described in subsequent sections of this chapter.

For the NLCL to operate, a pulse generator is required to inject a rectangular pulse into the line. Instead of using complex pulse generators [82] and those that involve pulse forming networks or pulse forming lines [41], we have implemented a much simpler pulse generator with only a few components. Our pulse generator consists of a storage capacitor C_{st} and a fast high voltage (HV) MOSFET semiconductor switch. This HV switch module actually consists of a large number of MOSFETs that are connected in parallel and in series, combined into a compact block that outputs a positive terminal and a negative terminal for external connections. For input, it requires a TTL-compatible control signal and a 5-volt auxiliary supply voltage. According to the manufacturer, the switch is rated at 10 kV and 200 A, and

has rise and fall times of 10-35 ns. A DC power supply charges the storage capacitor to the working voltage and a low voltage trigger pulse with the desired pulse duration activates the high voltage semiconductor switch to discharge the storage capacitor. The discharge pulse has a waveform that is almost rectangular in shape. A typical 3 kV discharge pulse for a capacitor C_{st} = 1 μF into a 50 Ω load is depicted in Figure 3.22. The pulse has a rise time of 35 ns and a fall time of 30 ns. A 50 Ω current limiting resistor R_{gen} is placed in series with the switch before connection to the cascading LC sections.

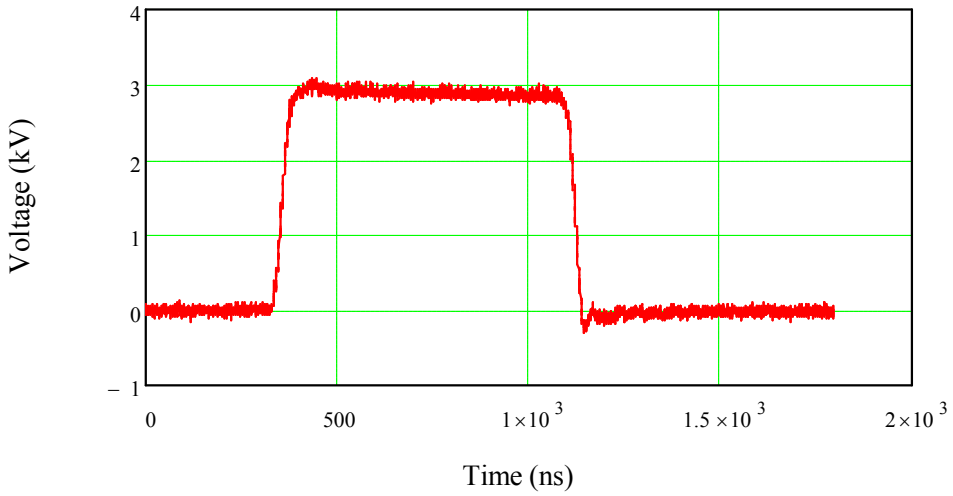

Figure 3.22 Typical output of pulse generator (charged to 3 kV) into a 50 Ω load.

The LC ladder network consists of n = 10 LC sections in which each section contains a single L connected to a single C arranged in an inverted "L" shape. Similar to the low voltage NLCL in Section 3.1.1, the nonlinear capacitors were chosen to give the largest nonlinearity among those tested; the linear inductors were then selected to have values close to 1 μH to give operating frequencies in the 10s MHz range. The inductive element L in the line is an air-core inductor made up of a 3-turn coil with diameter 48 mm and has an inductance of 0.9 μH. For the nonlinear capacitive element C in the line a Murata DEBF33D102ZP2A ceramic capacitor rated at 1 nF and 2 kV is

used. This type of ceramic capacitor is made of barium titanate (BT) and a study of its relaxation effects and the characteristic capacitance versus applied voltage (C-V) curve can be found in [83]. In the experiment here, the C-V curve of the nonlinear capacitor is obtained with the help of the measurement circuits shown in Figure 3.23.

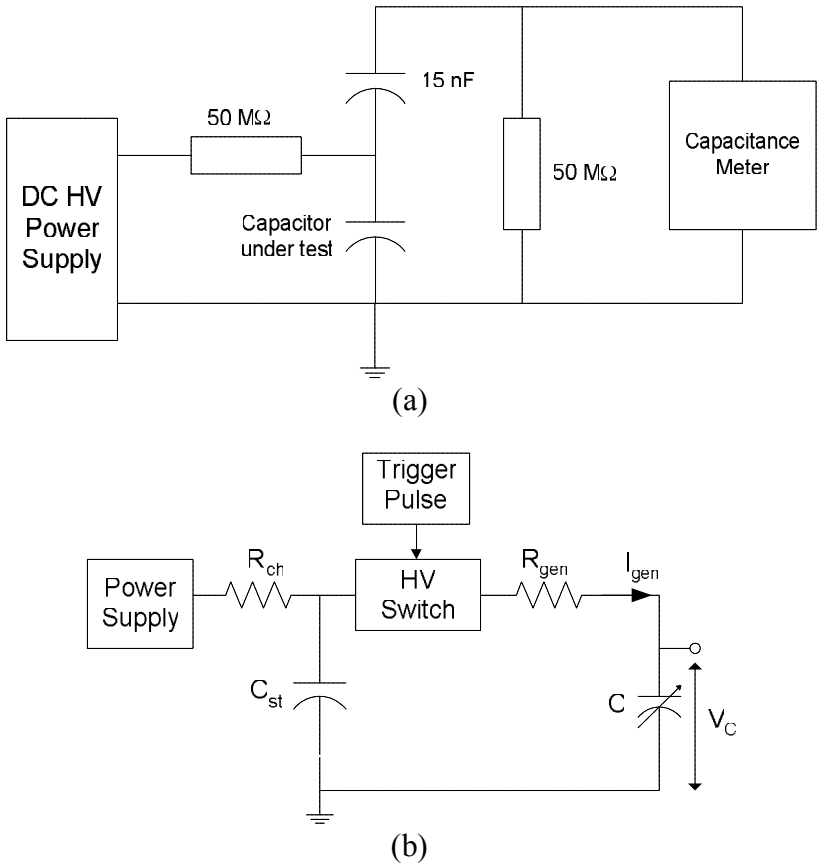

Figure 3.23 Circuits measuring the capacitance vs. applied voltage (C-V) characteristic of a nonlinear capacitor: (a) static measurement and (b) dynamic measurement.

From numerous experiments, modeling using static C-V curve gives fairly good match but tends to predict higher amplitudes. Using the dynamic C-V curve improves the matching as the capacitors are operated under rapidly pulsed voltage conditions. Figure 3.23(a) depicts the circuit for measuring the C-V characteristic under static conditions [18]. Values of the capacitance were plotted for voltages

ranging from 0 to 3 kV, as indicated in Figure 3.24. To improve the accuracy of the modeling, the C-V curve was also obtained under dynamic conditions where the time scale was consistent with the operation of the NLCL. The pulse generator was directly connected to the nonlinear capacitor under test as illustrated in Figure 3.23(b). By measuring the voltage V_c (using a commercial high voltage probe) across the capacitor and the current I_{gen} (using a commercial current monitor) flowing through it, the nonlinear differential capacitance can be calculated using

$$C = \frac{dQ}{dV} = \frac{dQ/dt}{dV/dt} = \frac{I_{gen}}{dV_c/dt} \tag{3.5}$$

where Q is the charge in the capacitor C. Basically, $C(V)$ is calculated from dividing the current through the capacitor by the derivative of the voltage across it ($I = C \cdot dV/dt$). This method of obtaining the dynamic C-V curve is similar to the one used in [20]. The dynamic C-V curve obtained at pulse amplitude of 4 kV is plotted in Figure 3.24. A curve fitting was performed on the dynamic curve using the hyperbolic tangent function as follows:

$$C(V) = (C_0 - C_{sat}) \cdot \left[1 - \tanh^2\left(\frac{V}{V_{sat}}\right)\right] + C_{sat} \tag{3.6}$$

where

V – applied voltage

C_0 – initial capacitance at $V = 0$

C_{sat} – saturation capacitance at large value of V

V_{sat} – saturation factor.

For best fit, the parameters obtained for Eq.(3.6) are C_0 = 623 pF, C_{sat} = 140 pF and V_{sat} = 658.2 V. The curve fit equation is also plotted in Figure 3.24 and is used in the NLETL model.

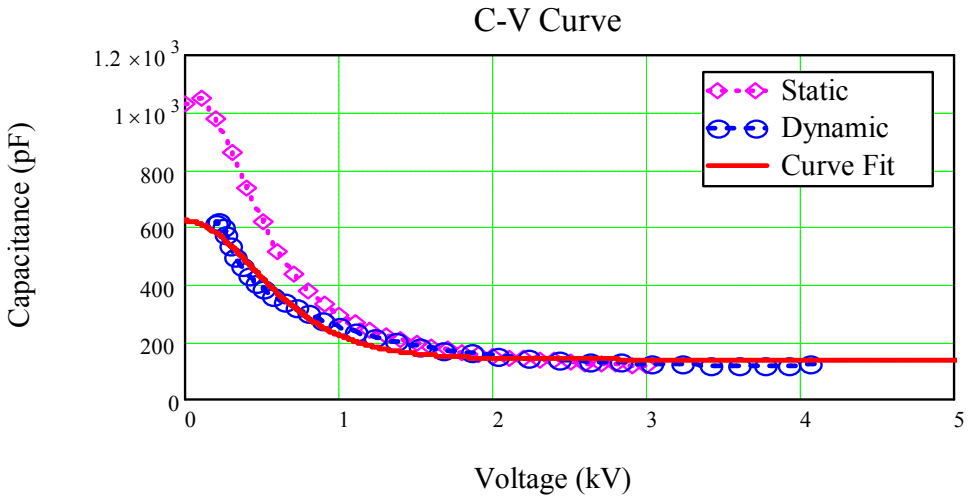

Figure 3.24 C-V curve of a nonlinear capacitor.

3.2.2 HIGH VOLTAGE NLCL WITH LOAD ACROSS CAPACITOR

This section discusses the NLCL with the resistive load placed across the nonlinear capacitor in the last LC section. The usual definition of voltage modulation depth (VMD) as a ratio of average peak-to-trough voltages [80] is good for comparing pulses with DC and AC components but cannot be used to compare pulses with only an AC component as the trough voltages are negative. We define here the average peak-to-trough load oscillation voltage for the first three pulse cycles as the voltage modulation depth (VMD) and it is given as

$$VMD = V_{ave} = \frac{\sum_{j=1}^{3} (V_{pt})_j}{3} \tag{3.7}$$

where,

j – oscillation cycle number

V_{pt} *– peak-to-trough load oscillation voltage.*

As can be seen in Eq.(3.3), the characteristic impedance will increase as *C(V)* decreases for increasing applied voltages. In order to find the load that best matches to the line in terms of peak power, a parameter sweep on the load was performed using the NLETL simulation model. We refer to the "peak power" here as the "average peak load power, P_{ave}" which is defined as the power calculated from half the average peak-to-trough load oscillation voltage for the first three pulses and the equation is given as

$$P_{ave} = \frac{\left(V_{ave}/2\right)^2}{R_{load}} \quad . \tag{3.8}$$

The VMD definition in Eq.(3.7) is more generic and allows for comparison of all waveforms where the amplitude of oscillation is a concern. The result of the simulated parameter sweep on the load is plotted in Figure 3.25 and indicates a maximum peak load power at around R_{load} = 100 Ω. Hence, for the experiment, a load of 100 Ω was placed across the capacitor at the last LC section. The measured load voltage indicates good match to the simulated one as depicted in Figure 3.26. From matching various experiment results with the NLETL model, the equivalent series resistance (ESR) of the nonlinear capacitor was estimated to be about 2 Ω.

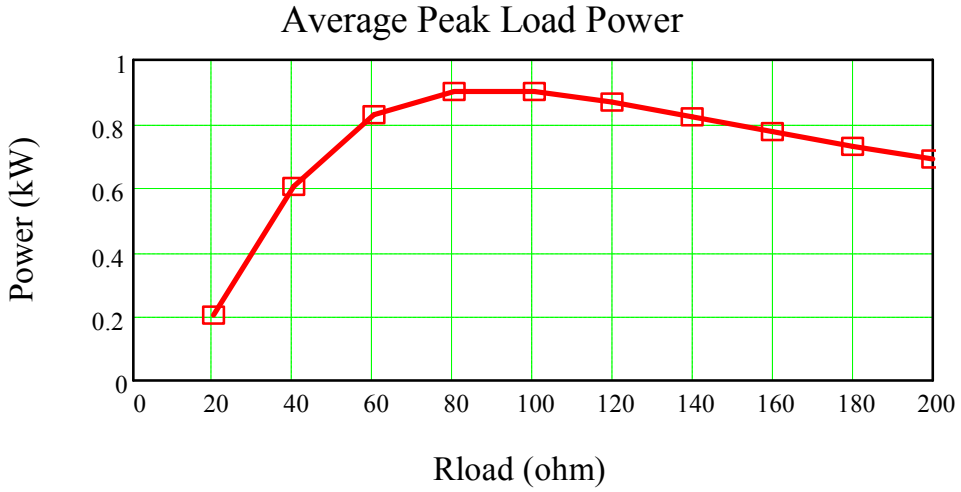

Figure 3.25 Load across capacitor: average peak load power as function of R_{load}.

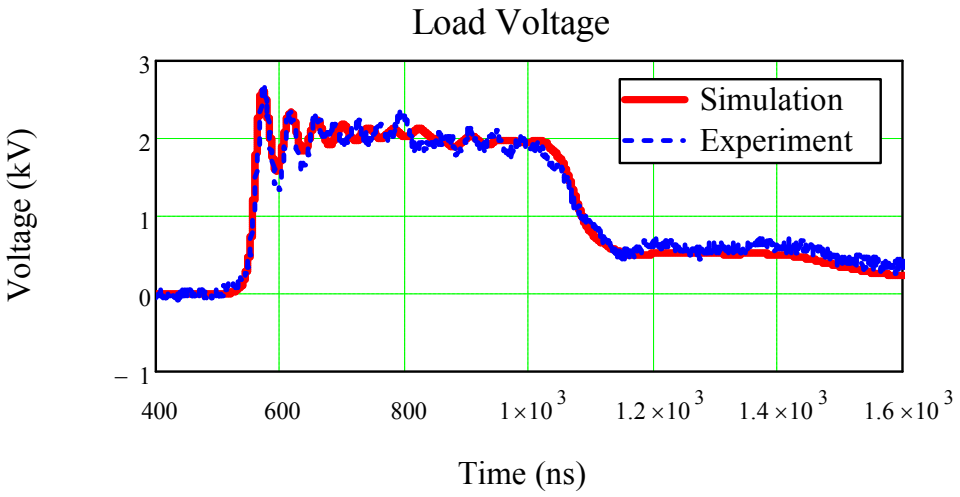

Figure 3.26 Load across capacitor: load voltage vs. time.

The frequency of each cycle in the oscillations is calculated and plotted against the time when the cycle ends. This time-frequency plot can also show the number of cycles of oscillations by simply counting the number of points plotted. The time-frequency plots for the simulation and experimental results are shown in Figure 3.27. The frequencies obtained are close to the Bragg frequency limit of 28 MHz as defined in Eq.(3.2).

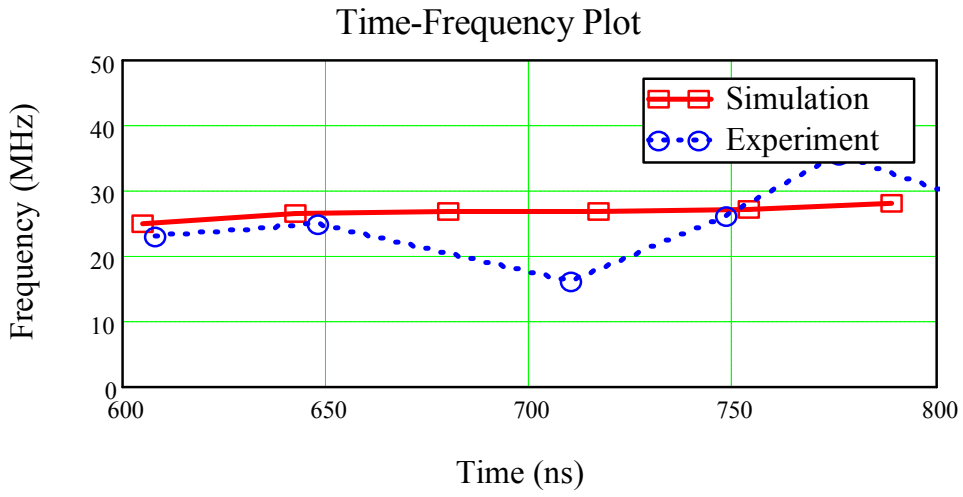

Figure 3.27 Load across capacitor: voltage oscillation frequency vs. time.

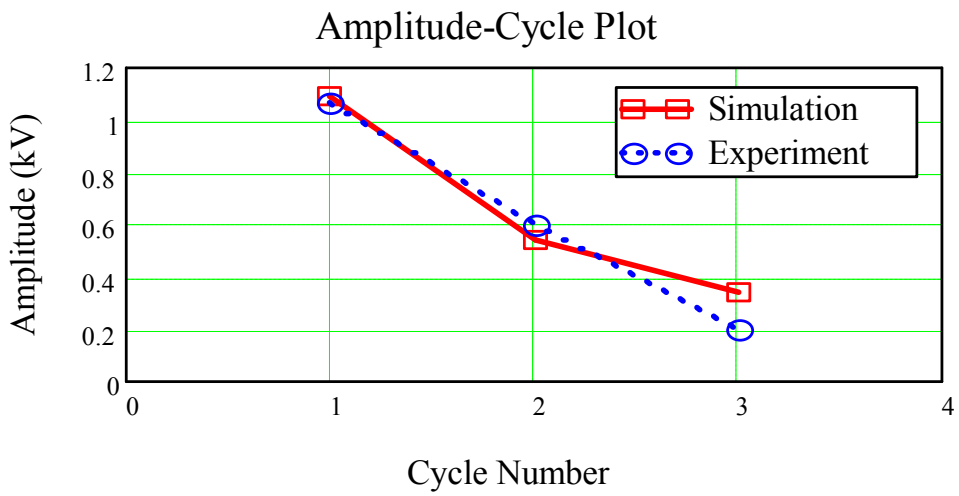

Figure 3.28 Load across capacitor: peak-to-trough oscillation amplitude vs. oscillation cycle number.

To see the quality of the load voltage modulation, the peak-to-trough oscillation amplitude V_{pt} is obtained for the first three cycles and is shown in the amplitude-cycle plot in Figure 3.28. The VMDs calculated from Eq.(3.7) for simulation and experiment are VMD_{sim} = 659 V and VMD_{expt} = 624 V, respectively. The experimental peak RF power calculated using Eq.(3.8) is 973 W. We introduce here the VMD index (VMDI) where the VMD is normalized to the input voltage. This VMD index will be useful to compare the degree of voltage modulation for lines with input pulses of different amplitudes. For an input pulse of 3 kV, the VMDIs for the NLCL with the load across the capacitor are $VMDI_{sim}$ = 0.22 and $VMDI_{expt}$ = 0.21.

The total matching efficiency and RF efficiency can be defined as $\eta_m = E_{out}/E_{in}$ and $\eta_{RF} = E_{RF}/E_{in}$ respectively;

where,

E_{in} – total input energy calculated by integrating the power entering the first section of the line

E_{out} – output energy calculated by integrating the total power on the load

E_{RF} – output RF energy calculated by integrating the power of the oscillating portion of the pulse.

In this case, $\eta_m = 96\%$ which indicates good matching to the load but the RF efficiency is only $\eta_{RF} = 0.36\%$ due to the fact that there is significant DC content in the output pulse (Figure 3.26) and the long duration of the input pulse where the latter part of the pulse did not result in any oscillations.

3.2.3 HIGH VOLTAGE NLCL WITH LOAD ACROSS INDUCTOR

For cascading LC sections in the NLCL it is observed that the voltage waveforms of the nonlinear capacitors are in anti-phase to their immediate neighbors. Based on this property, we proposed that the load be placed across the inductor in the last LC section so that the difference of the voltage waveforms for the last two nonlinear capacitors will result in higher amplitude AC waveforms in the resistive load. This method eliminates the need for a decoupling capacitor or high-pass filter at the end of the line which is required if the load is placed across the capacitor because this will contain both DC and AC components as seen in Section 3.2.2. It is also simpler than the asymmetric parallel (ASP) configuration in [80] where two lines are required.

Similar to the previous section, a simulated parameter sweep on the load was performed and the result plotted in Figure 3.29. The graph indicates a maximum average peak load power at around R_{load} = 300 Ω. For the experiment, a load of 300 Ω was placed across the inductor in the last LC section. A photograph of the experimental set-up is shown in Figure 3.30. The measured and simulated load

voltages in Figure 3.31 indicate good match.

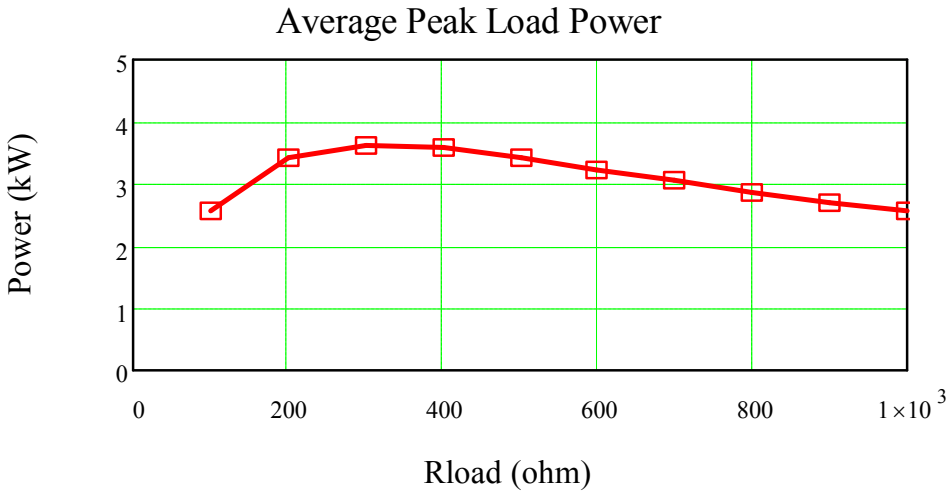

Figure 3.29 Load across inductor: average peak load power vs. R_{load}.

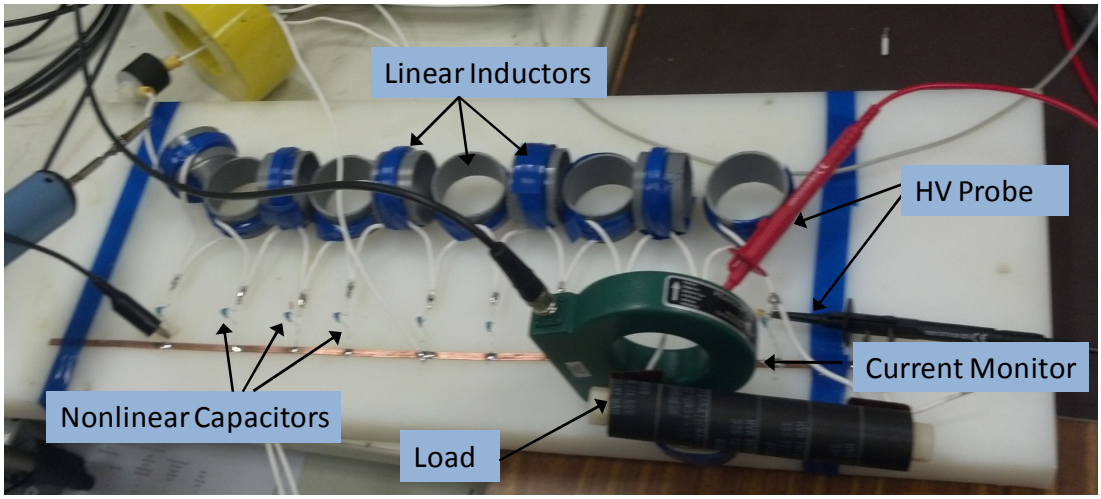

Figure 3.30 Photograph of a typical experimental set-up for a 10-section NLCL with load across inductor.

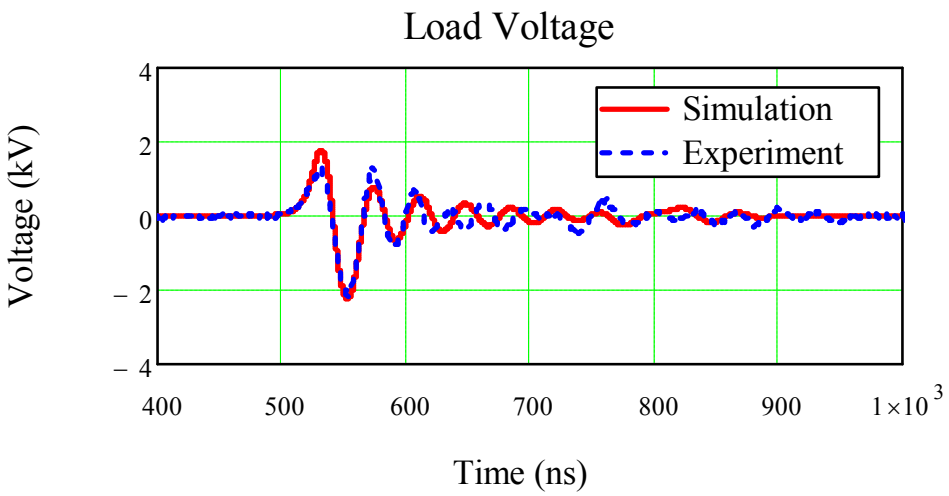

Figure 3.31 Load across inductor: load voltage vs. time.

The time-frequency plot and amplitude-cycle plot are shown in Figure 3.32 and Figure 3.33, respectively. Compared to the NLCL with the load across the capacitor, the NLCL with the load across the inductor has approximately the same oscillation frequency of 28 MHz, although the latter has a much lower frequency for the first cycle. However, for the case with the load across the inductor, the output has much higher peak-to-trough oscillation amplitudes where the VMD and VMDI are significantly larger. In simulations VMD_{sim} = 2136 V and $VMDI_{sim}$ = 0.712. The experimental values are comparatively lower at VMD_{expt} = 1818 V and $VMDI_{expt}$ = 0.606.

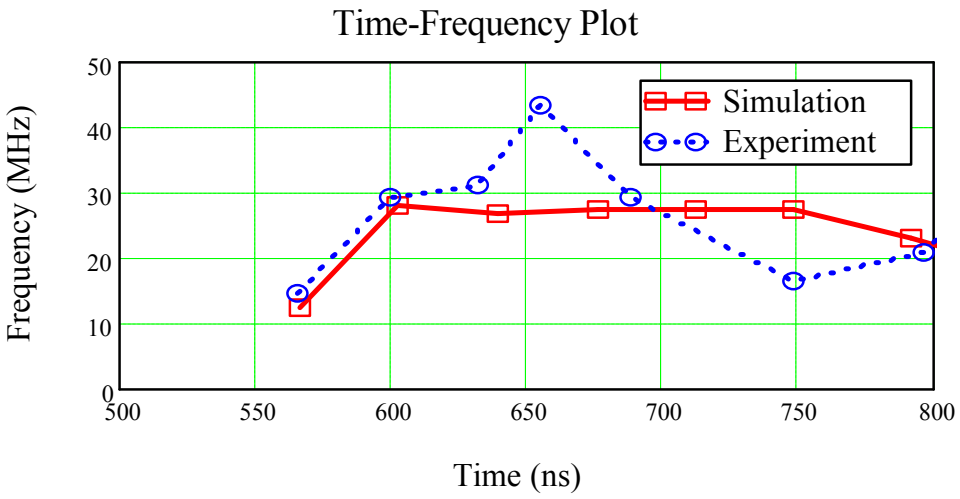

Figure 3.32 Load across inductor: voltage oscillation frequency vs. time.

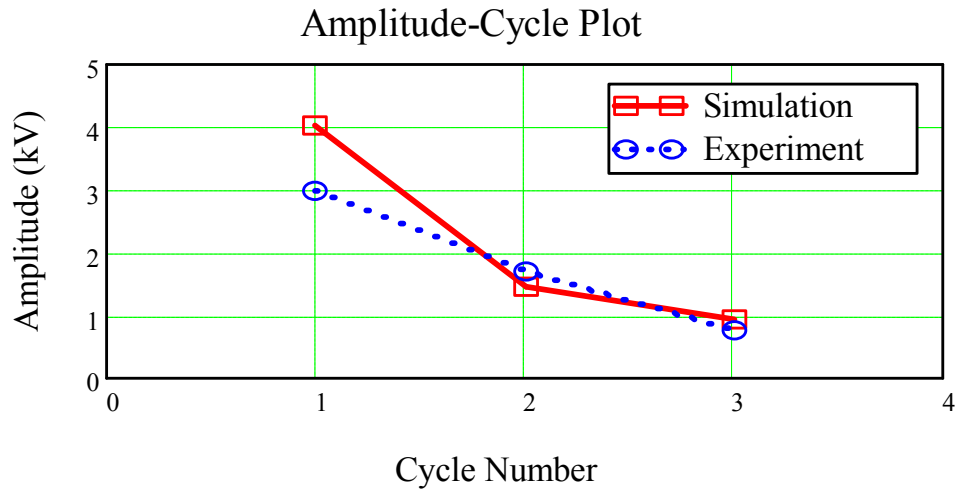

Figure 3.33 Load across inductor: oscillation amplitude vs. oscillation cycle number.

For the same input pulse of 3 kV, the experimental peak RF power calculated from Eq.(3.8) for the load placed across the inductor is 2754 W, which is about 2.8 times greater than that compared to the load placed across the capacitor in Section 3.2.2. Furthermore, the RF efficiency for the former is $\eta_{RF} = 4.6\%$ which is about 12 times better than the latter. Despite the small RF efficiencies, it should be noted that the two cases discussed here are for comparison with each other and further optimization could possibly result in higher RF efficiency of 10% or more.

3.2.4 FREQUENCY TUNING

To illustrate the ability to perform frequency tuning in a NLCL, a DC biasing voltage was applied to the nonlinear capacitors prior to the injection of the voltage pulse into the line. The DC biasing circuit consists of a DC power supply source V_{DC}, a high voltage diode, and an isolating inductor L_{bias} = 800 μH. This biasing circuit was connected to the first section of the NLCL that has the load placed across the inductor at the last section, as shown in Figure 3.34. The biasing voltage of the nonlinear capacitors V_{bias} was charged to V_{DC} before the trigger pulse was applied to the HV switch. To have wide frequency tunability it is necessary to have an input voltage pulse with amplitude that is farther away from the saturation voltage of the nonlinear capacitors, but it cannot be too low since a minimum voltage is required to initiate oscillations (Section 2.2.1.3). Consequently, we used an input pulse of 1 kV; as can be seen in Figure 3.24, this value is away from the capacitor saturation voltage of about 2 kV and there is sufficient capacitance variation between 1 and 2 kV. By varying V_{bias} from 0 to 800 V, the voltage across the load R_{load} was measured and the waveforms are compared in Figure 3.35.

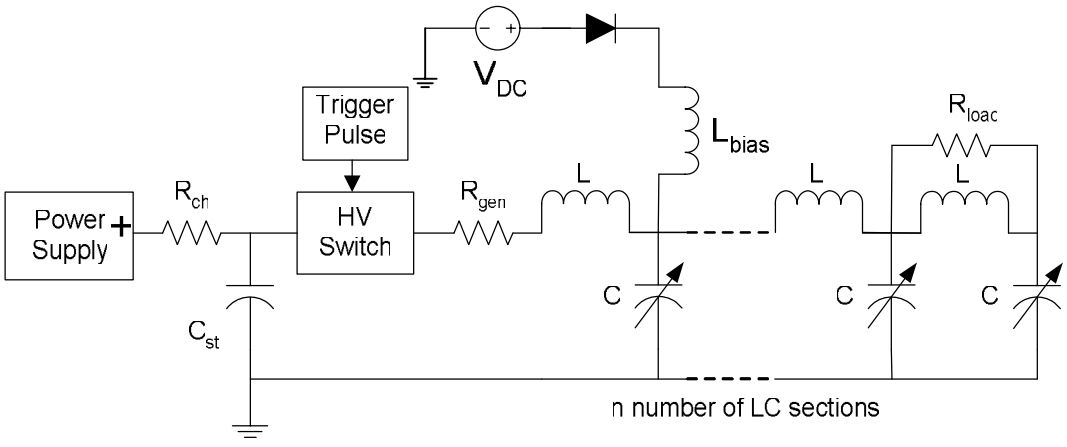

Figure 3.34 NLCL with inductive biasing circuit.

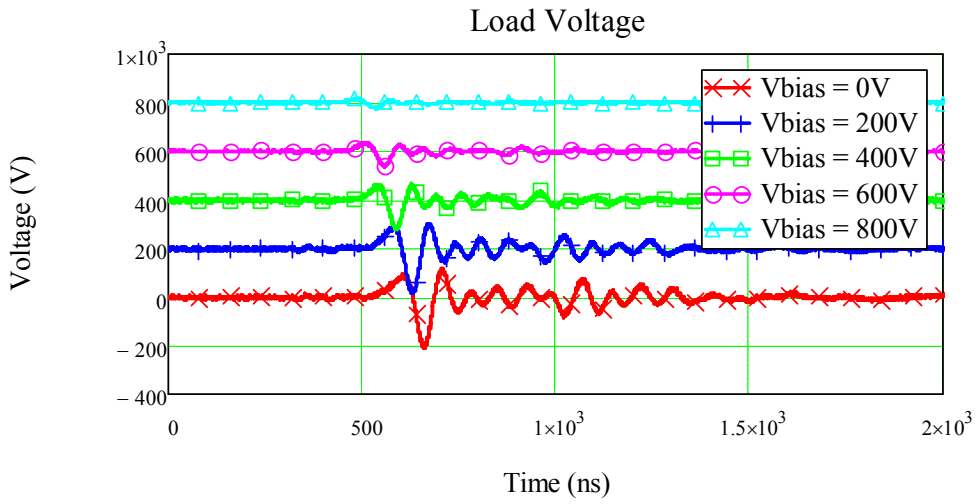

Figure 3.35 Waveforms of load voltage vs. time for different V_{bias} voltage (waveforms shifted by 200 V intervals for easy comparison).

As in previous sections, the measured load voltage waveforms were analyzed in terms of oscillation amplitudes and frequency contents. The amplitude-cycle plot in Figure 3.36 gives a very good indication of how the oscillation amplitudes for the first 3 cycles of the pulse vary with different V_{bias} voltages. The oscillation amplitudes decrease rapidly as V_{bias} increases. This is expected as the initial capacitance of the nonlinear capacitors decreases when V_{bias} increases according to Figure 3.24. Hence, with biasing the initial capacitance is brought closer to the saturation value leading to a small capacitance variation (working range of the capacitance) during pulse application, which in turn reduces drastically the amplitudes obtained as indicated in Section 2.2.6. However, the frequencies of the cycles generally increase with the increase in V_{bias} as depicted by the time-frequency plot in Figure 3.37. The reason is that, as the initial capacitance of the nonlinear capacitors is decreased by applying V_{bias}, the frequency of oscillations will increase according to Eq.(3.2). In Figure 3.37, it is observed that the frequency of the second cycle varied from 12 MHz to 17 MHz.

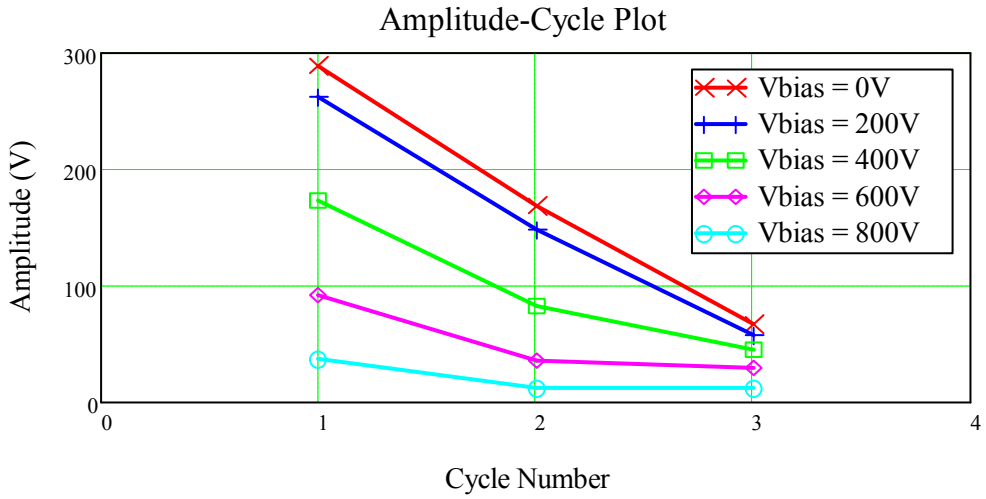

Figure 3.36 Waveforms of oscillation amplitude vs. oscillation cycle number for different V_{bias} voltage.

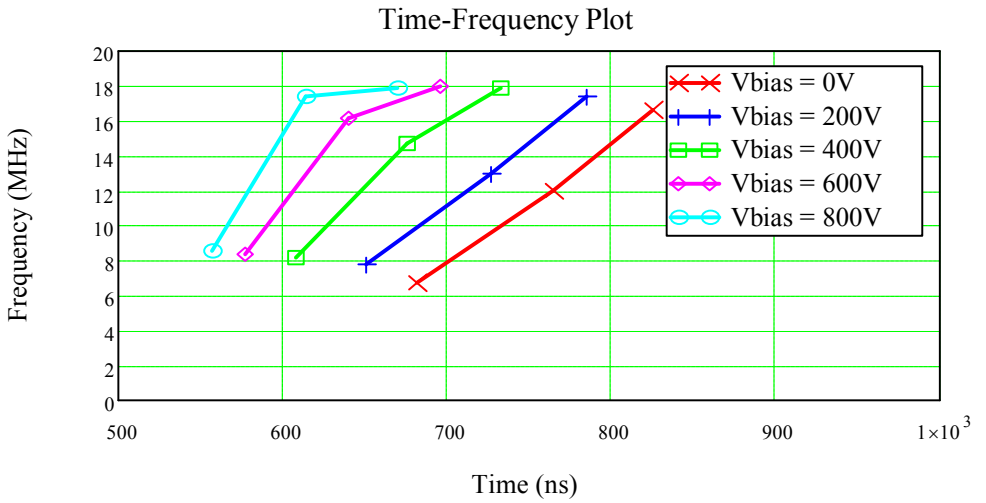

Figure 3.37 Waveforms of voltage oscillation frequency vs. time for different V_{bias} voltage.

3.3 DESIGN CONSIDERATIONS IN LOSSY NLCL

Although, great success was achieved using ferrite-based bead element lines (or NLILs) up to 1 GHz, attempts to operate at higher frequencies above 100 MHz using dielectric element lines (or NLCLs) have been described as impractical due to the capacitor dielectric losses that damp significantly the amplitudes of the RF output oscillations. In order to address this issue, this section by means of numerical simulations (using the NLETL model) it will be shown the possibility of producing oscillations with lower damping using conventional dielectrics of higher losses at frequencies above 1 GHz using ceramic slabs such as the lead-manganese-niobate (PMN) piezoelectric with high equivalent series resistance (ESR) of about 2 Ω.

3.3.1 BACKGROUND INFORMATION

NLCLs using diodes with variable capacitance in embedded coplanar or micro-strip systems can possibly achieve frequency in the GHz range, but with extremely low power. On the other hand, by using commercial ceramic capacitor and air core linear inductors, it is possible to generate RF with only moderate frequency and power (10 to 100 MHz and a few kW of peak power) (Section 3.2). This is because commercial nonlinear ceramic capacitors are normally limited up to 3- 5 kV rated voltages and have self-resonant frequencies in hundreds of MHz range, which are limiting factors in high power and high frequency applications. For high power NLCLs, the best results so far was described in a pioneering work by Ikezi et al. [31] with a parallel plate segmented dielectric line inserted with slabs of barium titanate (BT), where it was reported soliton generation with peak power of 10 MW at a center frequency around 300 MHz below the BT relaxation frequency used of 400 MHz.

Another work that produced 60 MW of RF at 100 MHz using barium titanate using a similar geometry was developed by Brown and Smith [7]. Apparently in this case the lower output frequency obtained than in Ikezi's work was due to the higher nominal unbiased capacitance in the range of nF of the BT slabs used (instead of pF). Anyway, results from both works indicated that pulses with lower damping could be obtained using dielectrics of lower losses, i.e. ESR less than 2 Ω. This result was also confirmed by French [84] recently using a segmented line with a different dielectric, a piezoelectric lead-manganese-niobate (designated PMN38) tile. In order to address that, in this section by means of numerical simulations using the NLETL model it will be shown the possibility of producing oscillations of higher amplitudes using PMN type dielectrics of higher losses (ESR ≈ 2 Ω) inserted in a planar geometry line as described in the literature [84]. Basically, this is made for lines with sections sweeping from 10 to 50 and same simulation parameters by increasing the mismatch at the load and at generator side.

3.3.2 MODELING OF NONLINEAR DIELECTRICS

For applications in high power NLCLs, varicaps are not suitable because of their small reverse breakdown voltage and low current rate. Then in these applications, ceramic capacitors are more appropriate and thus, their characterization and the subsequent implementation of corresponding C-V curve in NLETL model is of great importance for the NLCL design. Normally, capacitance of nonlinear ceramic capacitors decreases with the voltage, but for capacitor with PMN38 dielectric there is an initial alignment of the dipoles before reaching saturation, which means an initial increase of *C* with voltage. A generic model to represent the C-V variation is based on the Gaussian-like curve named the Lorentzian [84]. The C-V curve obtained from the

manufacturer and represented by the Lorentzian function in solid line (red) is shown in Figure 3.38. The corresponding mathematical formulation for the capacitance as a function of the voltage *C(V)* is given below:

$$C(V) = \frac{C_0 \cdot V_{HWFM}^2}{V_{HWFM}^2 + (V - V_0)^2} \tag{3.9}$$

where V_{FWHM} = 4500 V is the full width at half maximum (FWHM) voltage peak amplitude of *C*, and C_0 = 280 pF is the peak capacitance at the potential V_0 = 4000 V.

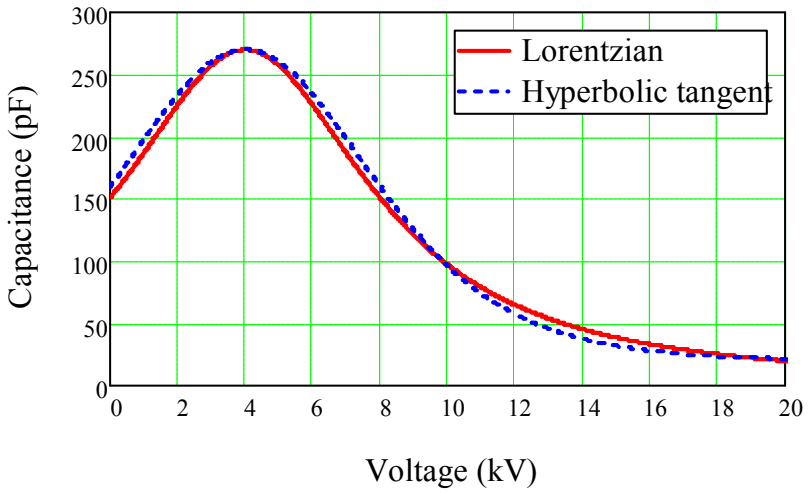

Figure 3.38 Comparison of the C-V curves for PMN38 capacitor: Lorentzian function (in red) and hyperbolic function (in blue).

Another formulation with good fitting based on a hyperbolic tangent function proposed in Section 3.2.1 is represented by the dotted line in blue in Figure 3.38. The corresponding mathematical formulation is given below:

$$C(V) = (C_0 - C_{sat}).\left[1 - \tanh^2\left(\frac{V - V_0}{V_{sat}}\right)\right] + C_{sat} \tag{3.10}$$

where *C* is the capacitance for the applied voltage, C_0 = 280 pF is the peak capacitance at V_0 = 4 kV, C_{sat} = 20 pF is the capacitance on saturation, and V_{sat} = 5 kV is the voltage at which saturation begins to take place.

In principle, Eqs. (3.9) and (3.10) can be used in the NLETL model to represent the PMN38 ceramic capacitor since as shown in Figure 3.38 that there is a good fitting between both formulations.

3.3.3 SIMULATION RESULTS

Simulations were made for a line of parallel plate geometry assumed with a linear fixed inductance of 13 nH per section and based on inserted PNM38 slab capacitors with C-V dependence of Figure 3.38. In the simulations, the line is excited by a 16 kV flat pump impulse generator with pulse of duration of the order of 50 ns and rise and fall times of about 6 ns. The first simulations were performed with the generator output and load basically matched to the characteristic impedance of the unbiased line on the order of 8 Ω.

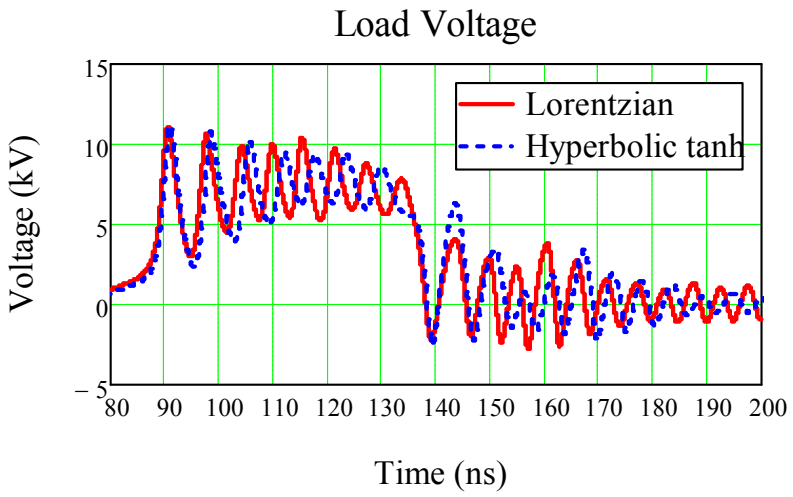

Figure 3.39 Output pulses obtained using two different functions for C-V curves (for matched case, n = 50, ESR = 0 Ω).

Figure 3.39 shows the output pulse simulation for a 50-section PMN38 LC ladder on the lossless condition (i.e. ESR = 0) using two different functions for C-V

curves. In Figure 3.39 one can see a good agreement between both the results and the appearing of the output RF on the electromagnetic shock wave formed in the pulse beginning at half the Bragg frequency. By using only Lorentzian function the LC ladder is simulated with the same parameters, except for the ESR condition, as shown in Figure 3.40. Herein one can observe that the oscillations are damped strongly when ESR increases from 0.2 to 2 Ω, disappearing practically with ESR = 2 Ω. Normally for high power NLCLs, piezoelectric based dielectrics (eg. PMN38) or ceramic based dielectrics (eg. BT) are used, but their ESR can reach 2 Ω or more depending on the frequency range of operation, which causes in practice the elimination of output oscillations as seen in Figure 3.40. Therefore, in order to reduce damping the idea proposed in this work consists of working on "mismatching" conditions on both sides of the NLCL (input and output), i.e. to have the source impedance and load values differ to a great extent from the line impedance. The idea behind this technique is to trap the voltage reflections inside the NLCL structure (so as to raise the voltages applied to the nonlinear capacitors) to increase the voltage modulation and the Bragg frequency along the line length which is given by Eq.(3.2), where L is the section inductance and $C(V)$ the section nonlinear capacitance.

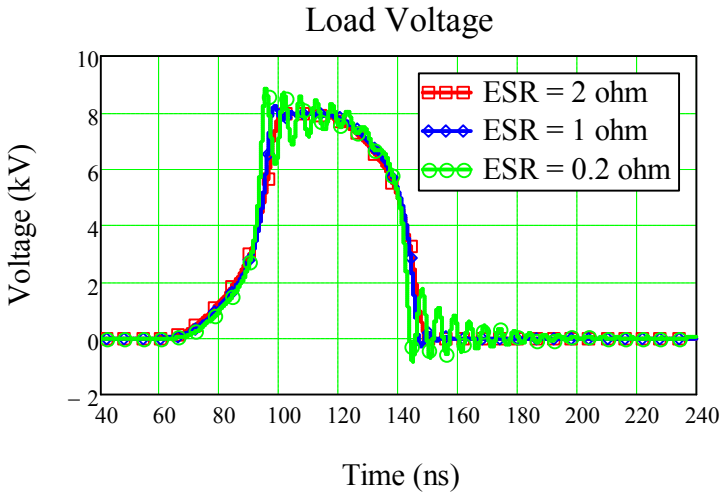

Figure 3.40 Output pulses obtained with different ESRs.

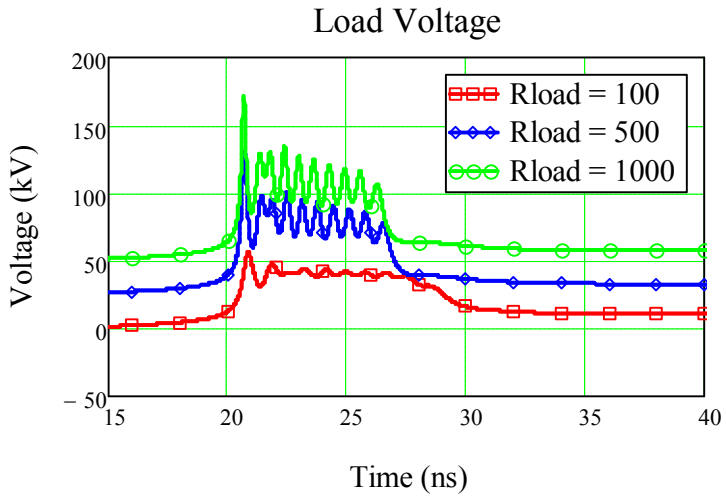

Figure 3.41 Lossy line simulation with load sweep for n=10 (waveforms shifted up by +50 kV for clarity).

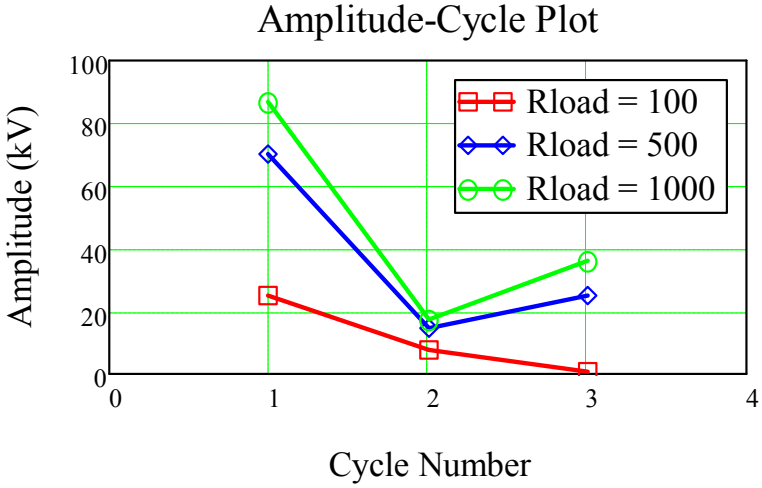

Figure 3.42 Amplitude-cycle plot obtained with load sweep.

The mismatches on both sides (input and output) were produced by a source impedance of 2.5 Ω and a 500 Ω load, respectively. For a 10-section lossy line, simulations were made for a load sweep from 100 to 1000 Ω. Figure 3.41 shows the output pulse obtained for three different values of the load R_L, where one can observe that by increasing the mismatch or R_L, higher oscillation amplitudes are produced. This is illustrated in Figure 3.42, which shows the amplitude for the peak-to-trough

oscillation voltages on the load for the first three pulse cycles. This sweep simulation is also used to determine the average load peak power as defined in Section 3.2.2. The plot of the average peak power as function of the load R_L is shown in Figure 3.43, which has optimum power for R_L in the range of 400-500 Ω. These simulations also indicated that frequency remains approximately the same above R_L = 300 Ω as shown in Figure 3.44 for the time-frequency plot on the load.

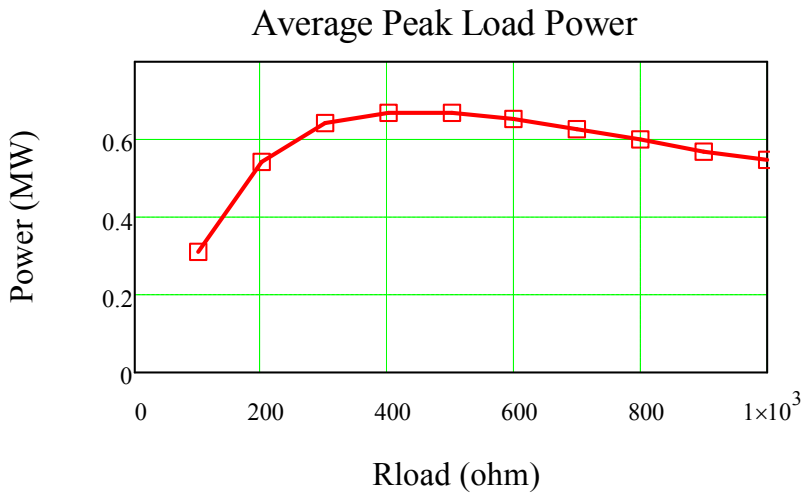

Figure 3.43 Average peak power plot as function of the load.

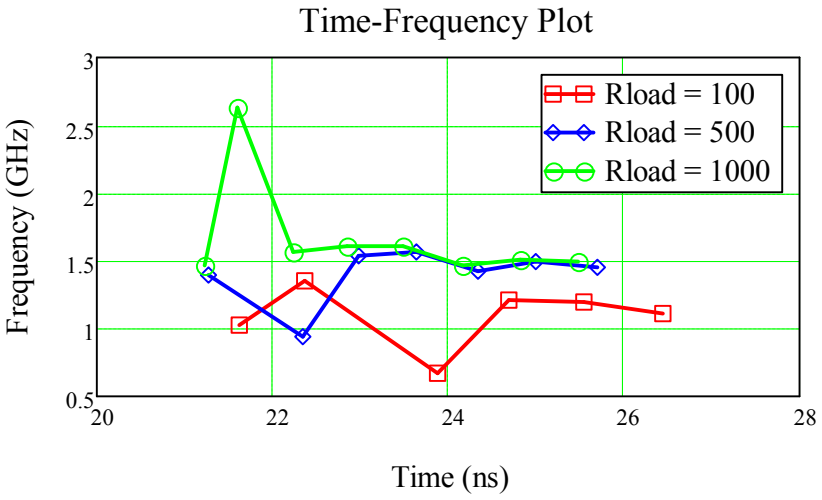

Figure 3.44 Time-frequency plot obtained with load sweep.

In Figure 3.44, one can also observe that the output frequency can spike up to 1.5 GHz or more depending on the load. This can be explained by the fact that voltage oscillation amplitudes at the load in simulations can reach 50 to 60 kV and from the C-V characteristic curve modelled by the Lorentzian function in Eq.(3.9), very low capacitance value of about 3.2 pF can be obtained. Hence, according to the Bragg frequency equation, the low biased value of the capacitance will result in a high frequency of 1.5 GHz. It is also observed that voltages along the line can go as high as 160 kV where dielectric breakdown issue will be a concern. For instance, Figure 3.45 illustrates this showing the capacitor voltage versus time at different sections for the mismatched line with 10 sections and load of 500 Ω, where section 10 is connected to the load.

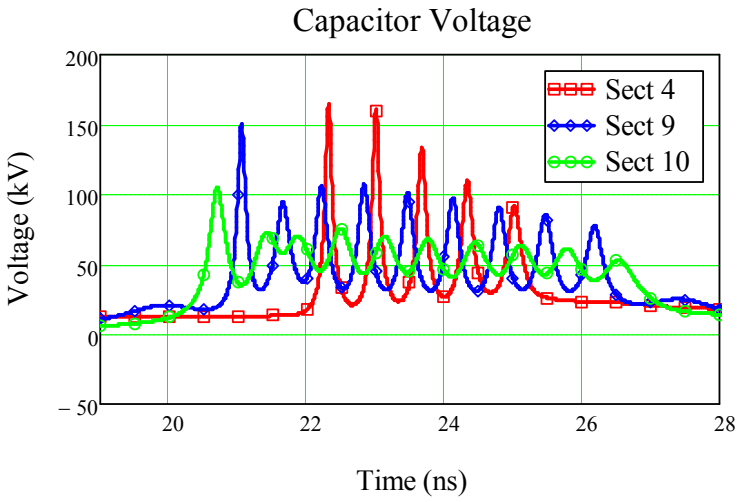

Figure 3.45 Voltage swings shown along line sections.

To complete the study on the mismatched lossy line, simulations were made with a sweep on line sections and load of 500 Ω, considering the amplitude of oscillations, peak power and frequency. Figure 3.46 shows the load voltage obtained as function of the number *n* of sections, where it is noticed that oscillations drift

downwards as *n* increases. Although, not shown herein, time-frequency and amplitude-cycle plots indicated respectively that frequency and amplitude of oscillations are basically not dependent on *n*. As in the previous simulation with *n* =10, the frequency of voltage oscillations at the load are kept near Bragg frequency of about 1.5 GHz with peak-to-trough oscillating amplitudes decreasing from about 70 kV to 20 kV for the first three cycles. Also in this case, simulations show that average peak power remains constant at around 0.6 MW with increasing value of *n* for a load of 500 Ω (as seen in Figure 3.43).

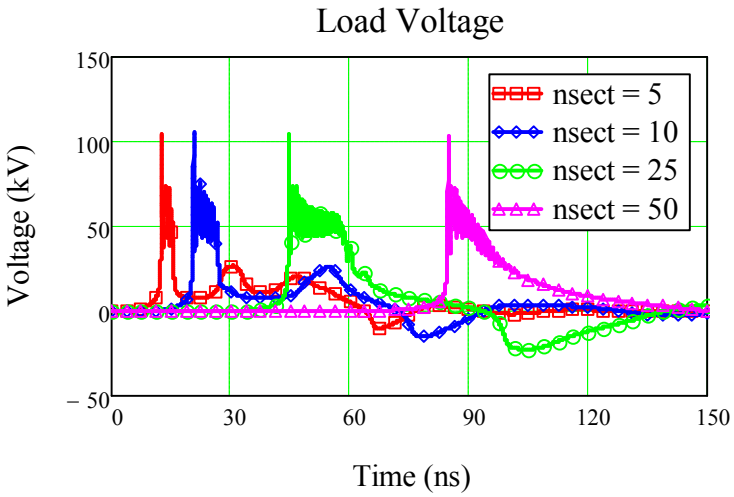

Figure 3.46 Load oscillations for different number of sections.

Despite simulations have shown that lossy PMN38 dielectric NLCLs may have excellent performance operating on mismatch conditions; however, it can be difficult to realize in practice. The feasibility will depend how the dielectric capacitance respond to the high voltage applied at the load and on middle sections of the line. For the good performance obtained in simulations it was assumed that dielectric capacitance can drop to a few picofarads. For instance, in this case the Bragg frequency spikes up to 1.5 GHz because capacitance becomes very low at high load voltage (about 3.3 pF for 50 kV). This is possible because *C(V)* was modelled by a

Lorentzian function given by Eq. (3.9), which does not impose a lower limit on capacitance when it saturates. Nevertheless if *C(V)* is modelled using a hyperbolic tangent function given by Eq. (3.10), C_{sat} is limited to 20 pF and the performance of the NLCL is seriously compromised as shown in Figure 3.47.

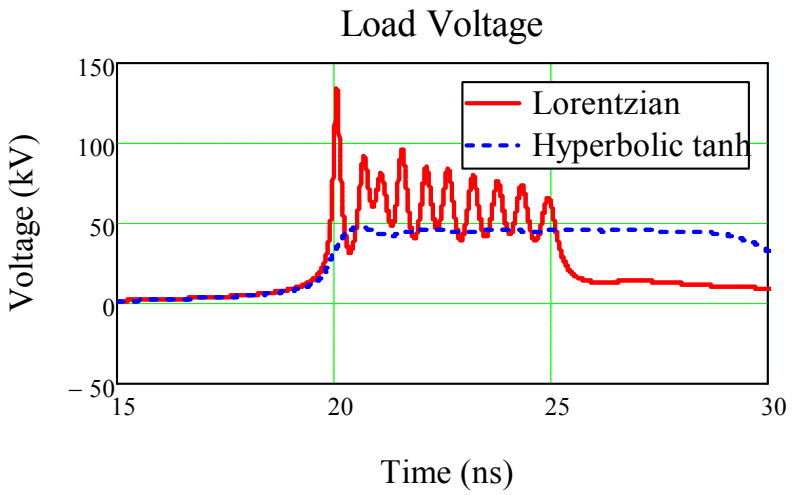

Figure 3.47 Load voltages using two different functions for C-V curves (for unmatched case, n = 10, ESR = 2 Ω).

3.3.4 ANALYSIS

In this section, it was demonstrated in simulation that in principle it is possible to generate large output voltage oscillations using lossy dielectric NLCLs. However, to realize it in practice could be very difficult due to several reasons. First, it will depend on how the dielectric capacitance will respond to the extremely applied high voltages (> 100 kV), i.e. if the dielectric nonlinearity is sufficiently steep and the capacitance value can saturate to very low values. Another problem is the dielectric breakdown (BD) issue. For instance, piezoelectric ceramic dielectrics have BD strength on the order of 50-100 kV/cm and it may be difficult to design a parallel plate transmission with a thickness of a few cm to resist the high voltages in the middle

sections. Besides that, there are still relaxation frequency and self-resonant frequency of the dielectric, which are also serious limiting factors for a good performance. Relaxation frequency of the ceramic dielectric materials is no more over 1 GHz, and worse is the self-resonance between the capacitance and the parasitic inductance associated to the dielectric in the line structure that can be of the order of 700 MHz, considering an inductance of 0.5 nH for an unbiased capacitance on the order of 100 pF.

3.4 CONCLUSIONS

Experimental demonstrations of NLCLs have been carried out using COTS components to validate the simulation results of the NLETL circuit model. The experimental results show very good match to the simulated waveforms. The implementation of the NLCLs using COTS components yields quick validation of the model. Frequency control of the NLCLs was also demonstrated by the addition of voltage biasing networks.

Two variations of low voltage NLCLs: one with two NLCLs in parallel and another with asymmetric parallel configuration were explored to obtain greater oscillation amplitudes (i.e. voltage modulation depth). At high voltage, a compact oscillating pulse generator whereby a simple pulse generator comprising a storage capacitor and a fast semiconductor switch was used to drive a NLCL was implemented. Definitions for voltage modulation depth (VMD), VMD index, and average peak load power were introduced to better quantify the quality of the output waveforms. Time-frequency plots have been used for frequency analysis and amplitude-cycle plots for examination of voltage modulation.

An innovative method to place the load across the inductor in the last section of the NLCL for better performance was proposed and the idea was validated through simulation and experiment. This method results in a direct AC waveform and eliminates the need for a high-pass filter or decoupling capacitor. It produces significantly greater oscillation amplitudes and has better RF efficiency compared to conventional NLCL. Frequency tunability was also demonstrated on this proposed line by adding a biasing circuit. By increasing biasing voltage on the nonlinear capacitors, the frequency of the output oscillations can be increased, but the trade-off is that the oscillations amplitudes will decrease.

Finally, a method is proposed in increasing the load voltage oscillations of a lossy dielectric NLCL by introducing mismatch at the generator and load sides. The proposed method is verified by simulation results obtained using the NLETL model. Critical issues are also highlighted in realising a practical lossy NLCL.

CHAPTER 4: NONLINEAR INDUCTIVE LINE (NLIL)

4.1 INTRODUCTION

This chapter describes the NLETL with nonlinear inductors and linear capacitors, herein called the nonlinear inductive line (NLIL) [82] and [85]. Better performance is obtained by introducing crosslink capacitors in the NLIL and there are numerous works about it from Belyantsev [38]-[40], Seddon [42] and Coleman [86]. The group from BAE systems (UK) has achieved 20 MW peak RF power at 1.0 GHz [42]. Generally, NLIL is capable of generating stronger pulse oscillations at higher frequencies than NLCL because the nonlinear component *L* in NLIL has higher quality factor *Q* (which means lower losses) compared to the nonlinear component *C* in NLCL. NLIL has the advantage of having higher nonlinearity due to its ferrite-based inductors compared to the nonlinear ceramic capacitors in NLCL.

The load voltage waveforms in [82] and [85] appear distorted and skewed. Hence, one of the main objectives here is to produce sinusoidal oscillations with good modulation depth using a NLIL driven by a simple pulser that utilizes a fast semiconductor switch. Subsequent sections describe the experimental work carried out in building and testing a high voltage NLIL by using commercial-off-the-shelf (COTS) components. The design of the NLIL was made possible by using the NLETL circuit

model developed in Chapter 2 that is well validated by experiments in Chapter 3.

Two novel methods are proposed here to characterize the ferrite-based nonlinear inductor. The first method is to obtain the nonlinear L-I profile of the inductor by a curve fitting process for use in the NLETL model. The second method focuses on obtaining the key parameters in the Landau-Lifshitz-Gilbert (LLG) equation [87] and [88] for use in the NLETL model. Results simulated by the NLETL model show good match to the data obtained from the experiments.

In order to better quantify the oscillating pulses produced by the NLIL, the voltage modulation and the frequency content of the pulses are carefully analyzed using amplitude-cycle and time-frequency plots. Trade-offs using crosslink capacitors are also discussed.

4.2 DESCRIPTION OF NLIL

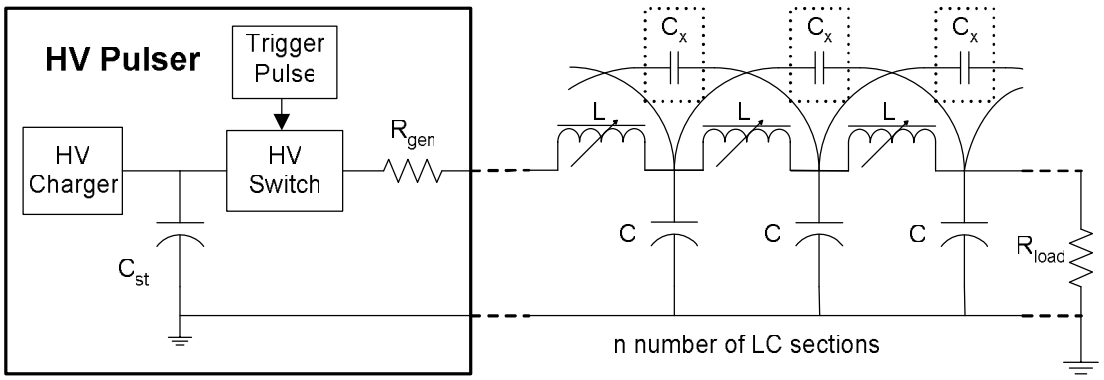

Figure 4.1 Experimental set-up of a NLIL shown with crosslink capacitors C_x.

The NLIL was built using COTS components and the circuit diagram for setting up the experiment is depicted in Figure 4.1. It shows a high voltage (HV) pulser connected to the line with resistive load R_{load} where crosslink capacitors C_x can be

added in-between the LC sections to improve performance. Instead of using a pulser that involves a pulse forming network (PFN) or pulse forming line (PFL) [41], or one with complex architecture [82], we have implemented a much simpler pulser with only a few key components. Our pulser was custom-made in which the high voltage charger, fast high voltage MOSFET semiconductor switch and current limiting resistor R_{gen} = 75 Ω are mounted on a circuit board; together with the storage capacitor C_{st} = 1.3 μF, all parts are housed in a compact enclosure. This compact pulser can be charged up to 9 kV and produces an output waveform that is almost rectangular in shape with pulse repetition rate (PRF) of up to 100 kHz. The output pulse duration is adjustable (depending on the low voltage trigger pulse) and has a typical rise time of 20 ns and fall time of 12 ns. Compared to the usual PFN and PFL, our pulser has a much simpler and compact configuration in generating HV flat pulses with short rise time. In addition, the semiconductor switch in our pulser allows great flexibility in controlling the pulse duration and achieving very high PRF. PFN and PFL usually have fixed pulse duration and are bulky in size; the former is useful for microsecond pulse generation with slower rise time (> 200 ns) whereas the latter is suitable for nanosecond pulse generation with faster rise time (< 100 ns).

The NLIL consists of *n* number of LC sections in which each section contains a single *L* connected to a single *C* arranged in an inverted "L" configuration so that cascading the sections will form a "T" network. Similar to the low voltage NLCL in Section 3.1.1, the COTS ferrite beads were first selected as the nonlinear inductors based on the largest nonlinearity and subsequently, the value of the linear capacitors were selected to give 10s MHz operating frequency. A few ferrites and capacitors were actually shortlisted and tested, but only the ones that gave the best performance were presented.

The capacitive element *C* in the line is a Murata DEA1X3F101JA2B ceramic capacitor rated at 100 pF (with tolerance of ± 5 %) and 3.15 kV. For the nonlinear inductive element *L* in the line a Fair-rite 2944666651 ferrite bead made of NiZn is used. It should be noted that the authors in [85] observed that their line with pre-shot reset current to the ferrite beads performed better than one without pre-shot reset current; even though both of their cases did not give good sinusoidal-shape oscillations. However, contrary to them, we observed in our experiments that the line without pre-shot reset current was better than one with pre-shot reset current. Both our cases gave good sinusoidal-shape waveform and the one without pre-shot current produced better oscillation amplitudes. Hence, the experiments described in here were performed with the NLIL without pre-shot reset current.

Pertaining to Section 1.1.3, the phase velocity v_p, Bragg frequency f_B, and characteristic impedance Z_0 of the line are reproduced here for ease of reference in Eqs. (4.1), (4.2) and (4.3) respectively; but in this case, the capacitor is linear and the capacitance is taken as a constant *C*.

$$v_p = \frac{1}{\sqrt{L(I)\cdot C}} \tag{4.1}$$

$$f_B = \frac{1}{\pi\cdot\sqrt{L(I)\cdot C}} \tag{4.2}$$

$$Z_0 = \sqrt{\frac{L(I)}{C}}\ . \tag{4.3}$$

4.2.1 CHARACTERIZATION USING CURVE FIT FUNCTION

In order to characterize the nonlinear inductor made from the ferrite bead under dynamic conditions at the time scale of operation of the NLIL, the pulser was connected directly to the nonlinear inductor under test via the load R_{load} = 50 Ω that is to be used in the line. The characterization circuit is illustrated in Figure 4.2 where the voltage V_L across the nonlinear inductor and the current I_L flowing through it are measured.

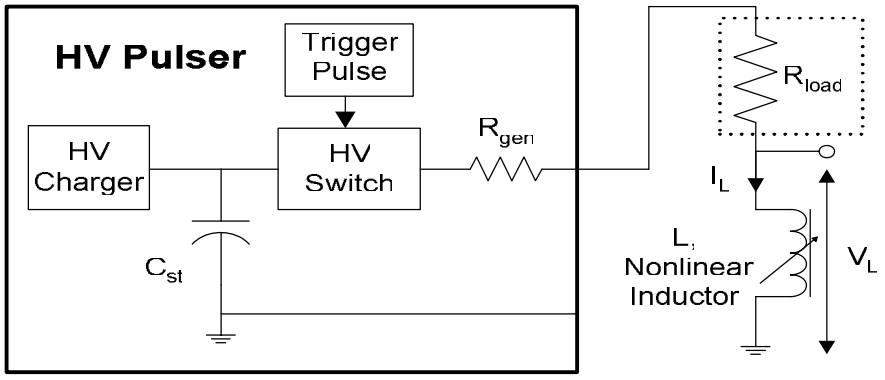

Figure 4.2 Circuit used for characterizing a nonlinear inductor.

The method to obtain the flux-current curve for the ferrite is similar to [89]. For a charge voltage of 5 kV and output pulse duration of 400 ns from the pulser, measured waveforms of V_L and I_L for the rising part of the pulse are shown in Figure 4.3(a). The magnetic flux linkage Ψ in the ferrite bead can then be derived from $V_L = d\psi/dt$ using

$$\Psi(t) = \int V_L(t)dt \,. \tag{4.4}$$

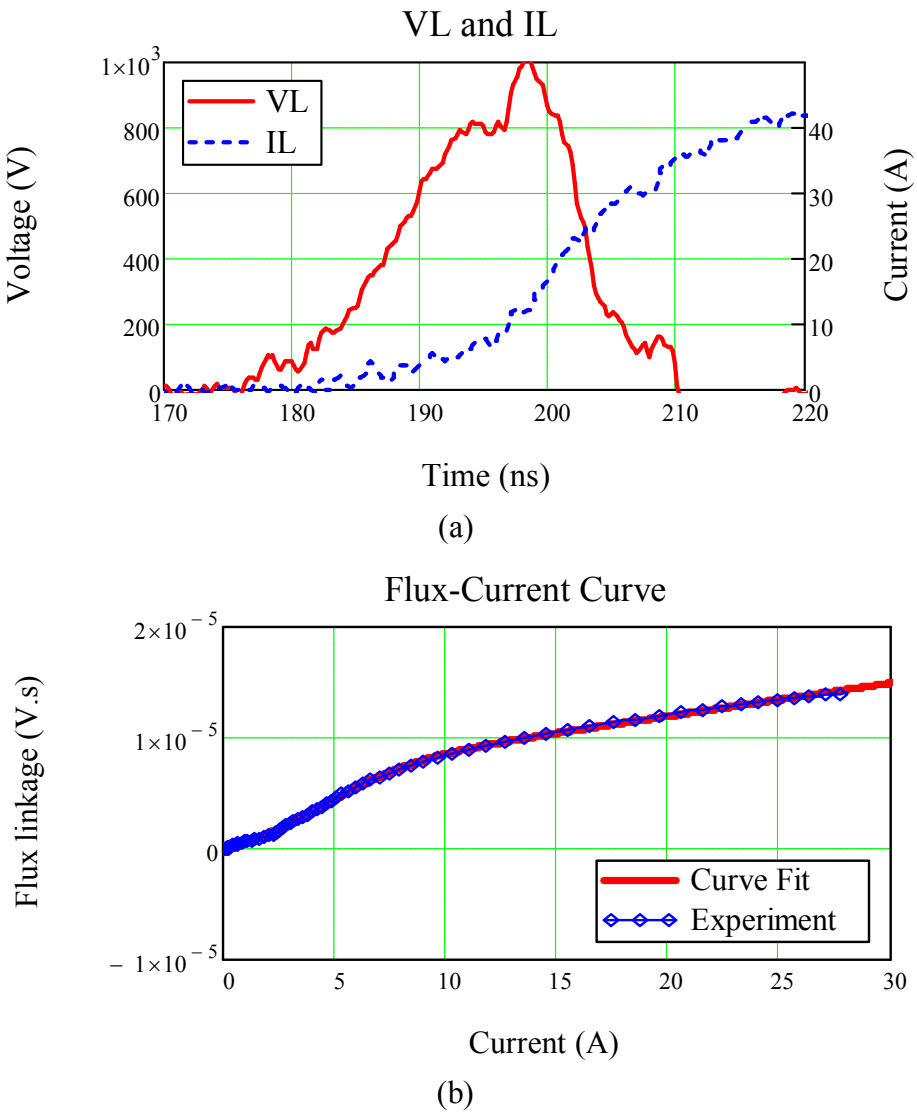

Figure 4.3 Measurements of: (a) voltage V_L , current I_L; and (b) derived flux linkage vs. current of the nonlinear inductor.

Then the characteristic dynamic Ψ-I curve of the nonlinear inductor can be plotted as indicated in Figure 4.3(b). Also shown in this figure, a curve fit was performed on the dynamic curve obtained by using the hyperbolic tangent function given by:

$$\Psi(I) = (L_0 - L_{sat}) \cdot I_{sat} \cdot \tanh\left(\frac{I - I_t}{I_{sat}}\right) + L_{sat} \cdot I + \Psi_t \,, \tag{4.5}$$

where,

I - applied current;

L_0 - initial inductance at I = 0;

L_{sat} - saturation inductance at large value of I;

I_{sat} - saturation scaling factor;

I_t - current shifting factor;

Ψ_t - flux shifting factor.

For best curve fitting [see again Figure 4.3(b)], the parameters obtained for Eq.(4.5) are L_0 = 1.122 μH, L_{sat} = 299 nH, I_{sat} = 4.023 A, I_t = 4.681 A and Ψ_t = 2.672 μV·s. The differential inductance L_d [90] or effective inductance [91] for use in the NLETL model is then obtained by

$$L = L_d(I) = \frac{d\Psi}{dI} = (L_0 - L_{sat})\left[1 - \tanh^2\left(\frac{I - I_t}{I_{sat}}\right)\right] + L_{sat} \,, \tag{4.6}$$

where the characteristic L vs. I curve is plotted in Figure 4.4. The voltage equation for modeling the nonlinear inductor is thus

$$V_L = \frac{d\Psi}{dt} = \frac{d\Psi}{dI} \cdot \frac{dI}{dt} = L_d \cdot \frac{dI}{dt} \,. \tag{4.7}$$

It should be noted that the measurements shown in Figure 4.3(a) were made on the ferrite bead condition with B-H hysteresis curve in the first quadrant. In this case, it was not necessary to find the constant remanent flux as the differential inductance is defined as the derivative of the flux in Eq.(4.6).

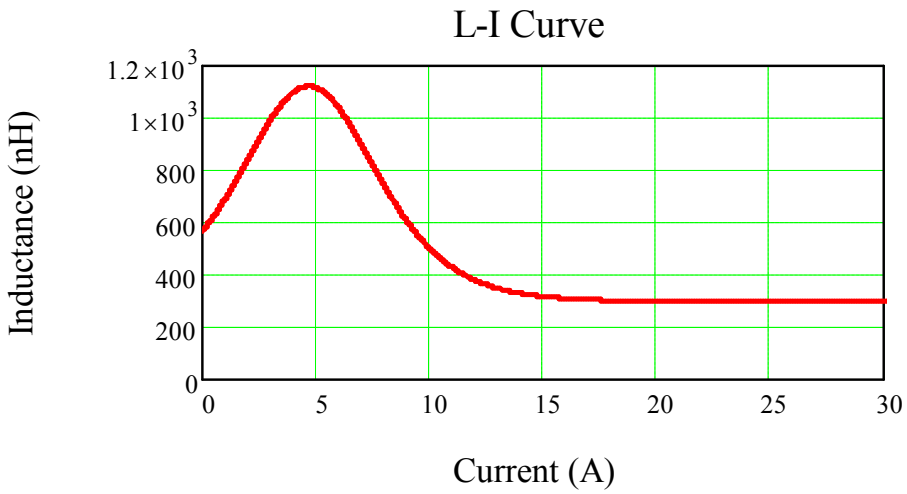

Figure 4.4 L vs. I curve obtained for the nonlinear inductor.

4.2.2 CHARACTERIZATION USING LANDAU-LIFSHITZ-GILBERT (LLG) EQUATION

The nonlinear magnetic property of the ferrite bead is modelled using the Landau-Lifshitz-Gilbert (LLG) equation [87] and [88] and the simplified form [40], [92]-[94] as derived in Appendix C is given as

$$\frac{dM(t)}{dt} = \frac{M_s \cdot \gamma_0 \cdot \alpha}{(1+\alpha^2)} \cdot \left[1 - \left(\frac{M(t)}{M_s}\right)^2\right] \cdot H(t) \tag{4.8}$$

where,

M(t) = mean value of magnetization vector (parallel to magnetic field);

M_s *= saturation magnetization;*

H(t) = magnetic field strength;

α *= dimensionless damping parameter;*

γ_0 *= 221 km/C, gyromagnetic ratio.*

We propose here a simple approach in determining the characteristic parameters M_s and α of the ferrite bead. In order to characterize the nonlinear inductor made from the ferrite bead under dynamic conditions at the time scale of operation of the NLIL, the pulser was connected directly to the nonlinear inductor under test via the load R_{load} = 50 Ω that is to be used in the line. The characterization circuit is illustrated in Figure 4.2 where the voltage V_L across the nonlinear inductor and the current I_L flowing through it are measured .

For a charge voltage of 5 kV and output pulse duration of 400 ns from the pulser, V_L and I_L are measured without resetting the ferrite core and are shown in Figure 4.5(a). Similar waveforms [Figure 4.5(b)] are also obtained for the case where

the ferrite core was reset. The magnetic flux linkage Ψ in the ferrite bead for both cases can then be calculated using Eq.(4.4).

The characteristic dynamic Ψ-I curves of the nonlinear inductor with and without core reset are plotted in Figure 4.5(c) and the saturation flux linkages noted at saturation current I_s = 43 A are Ψ_{s1} (with reset) = 23.4 μV·s and Ψ_{s2}(no reset) = 11.9 μV·s respectively. The remanent flux is then calculated as $\Psi_r = (\Psi_{s1} - \Psi_{s2})/2$ = 5.73 μV·s assuming that the B-H hysteresis curve is symmetrical. By applying the standard magnetic field strength and magnetic flux density equations:

$$H = \frac{N \cdot I}{l_e} \tag{4.9}$$

$$\text{and } B = \mu_0 \cdot (H + M), \tag{4.10}$$

we can calculate the magnetic flux as

$$\psi = N \cdot B \cdot A_e = \eta \cdot (p \cdot I + M) \tag{4.11}$$

where,

I = applied current;

N = number of coil turns;

l_e = effective magnetic path length;

μ_0 = permeability of free space;

A_e = effective cross-sectional area;

$\eta = N \cdot A_e \cdot \mu_0$;

$p = \frac{N}{l_e}$.

From the dimensions of the ferrite bead, we estimate that η = 0.088 nH·m and p = 997 m^{-1}.

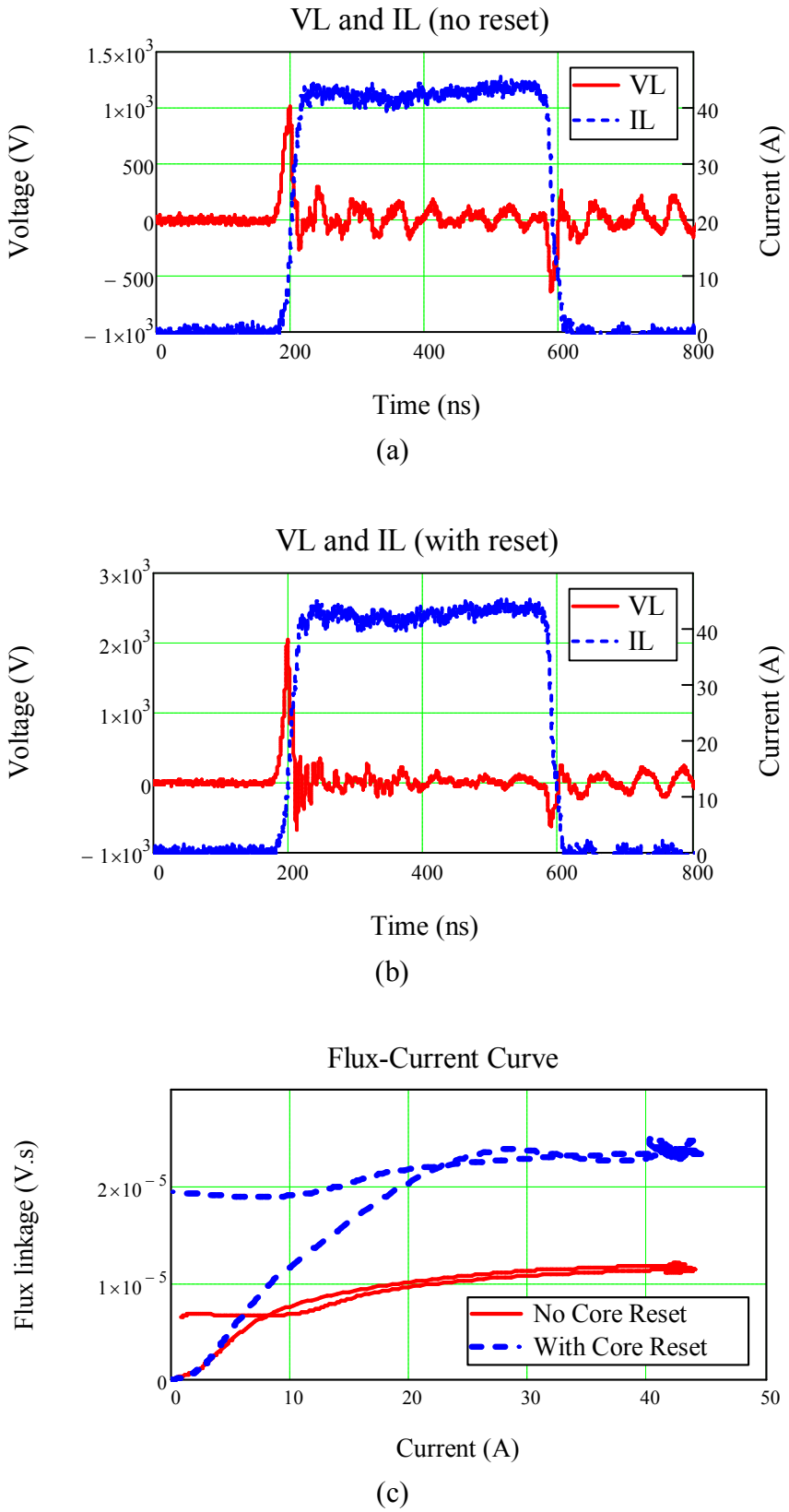

Figure 4.5 (a) Measurements of voltage V_L and current I_L without core reset; (b) measurements of voltage V_L and current I_L with core reset; (c) derived flux linkage vs. current of the nonlinear inductor for cases with and without core reset.

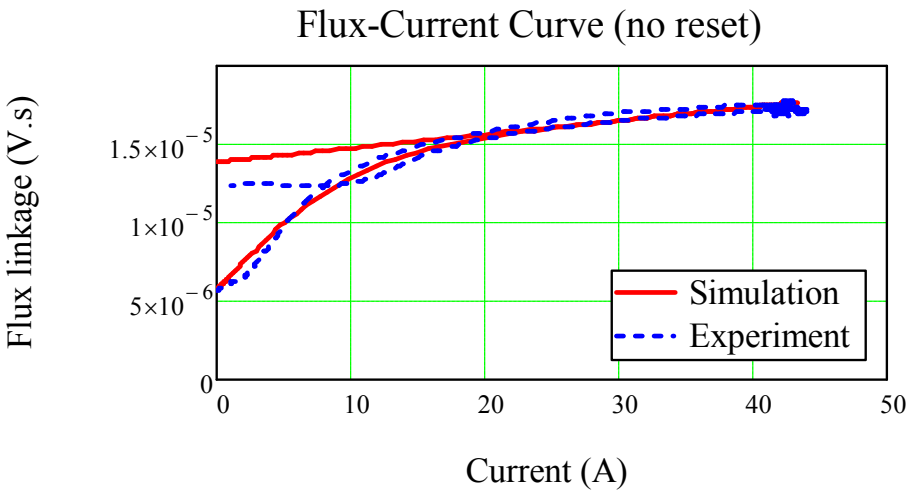

(a)

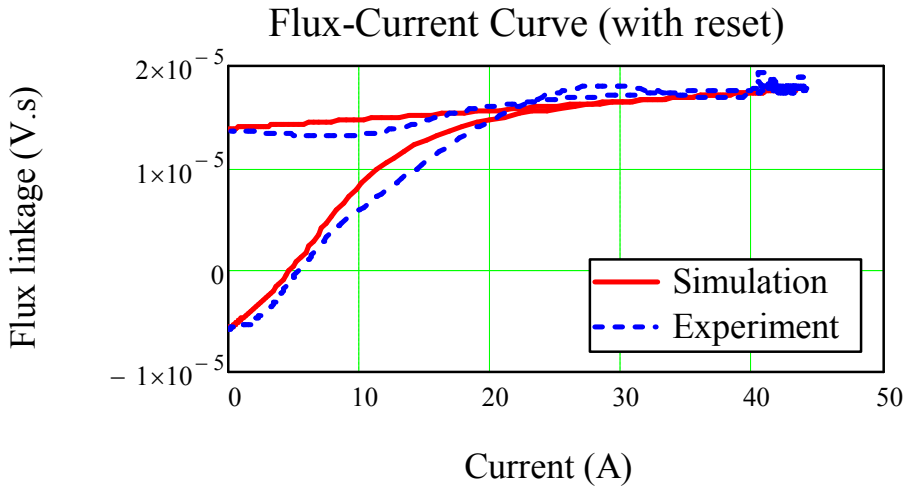

(b)

Figure 4.6 Comparison of simulation and experiment: (a) flux linkage vs. current for case without core reset; (b) flux linkage vs. current for case with core reset.

Hence, by using Eq.(4.11), we calculated M_r = 65.2 kA/m by setting I = 0 A and M_s = 158 kA/m by setting I_s = 43 A. Finally, the characterization circuit in Figure 4.2 was simulated using the LLG equation and the calculated flux-current curves show fairly good match to the experimental ones in Figure 4.6 for damping parameter α = 0.07. Figure 4.6(a) depicts the case without core reset where M_r is positive [the experimental curve without reset from Figure 4.5(c) was shifted up by Ψ_r] and Figure

4.6(b) depicts the case with core reset where M_r is negative [the experimental curve with reset from Figure 4.5(c) was shifted down by Ψ_r].

To model the NLIL, the voltage equation for modeling the nonlinear inductor is taken as $V_L = \frac{d\Psi}{dt}$ and the LLG equation in Eq.(4.8) is included in the NLETL model to account for the dynamics of the ferrites.

4.3 RESULTS OF NLIL

This section analyzes the results of a 20-section NLIL with R_{load} = 50 Ω. The pulser is charged to 5 kV and a discharge pulse of 400 ns duration with approximately rectangular shape is injected into the NLIL. For a saturation inductance of about 300 nH, the linear capacitance is selected to be 100 pF (as indicated in Section 4.2) so that the line can operate close to the Bragg frequency of 58 MHz according to Eq.(4.2). In this case, the calculated characteristic impedance from Eq.(4.3) of the line at saturation is 55 Ω. We use here the average peak load power P_{ave} and voltage modulation depth (VMD) as defined in Section 3.2.2. As can be seen in Eq.(4.3), the characteristic impedance will decrease as $L(I)$ decreases for increasing applied currents. In order to find the load that best matches to the line in terms of P_{ave}, a parameter sweep on the load was performed using the NLETL simulation model. The load of 50 Ω was chosen as it gives peak power near to the maximum point in the sweep. The current through the load was measured using a commercial current monitor and the load voltage was measured using a commercial high voltage probe.

4.3.1 MODELING USING CURVE-FIT L-I CURVE

The measured load voltage indicates a good agreement with the simulated result as shown in Figure 4.7.

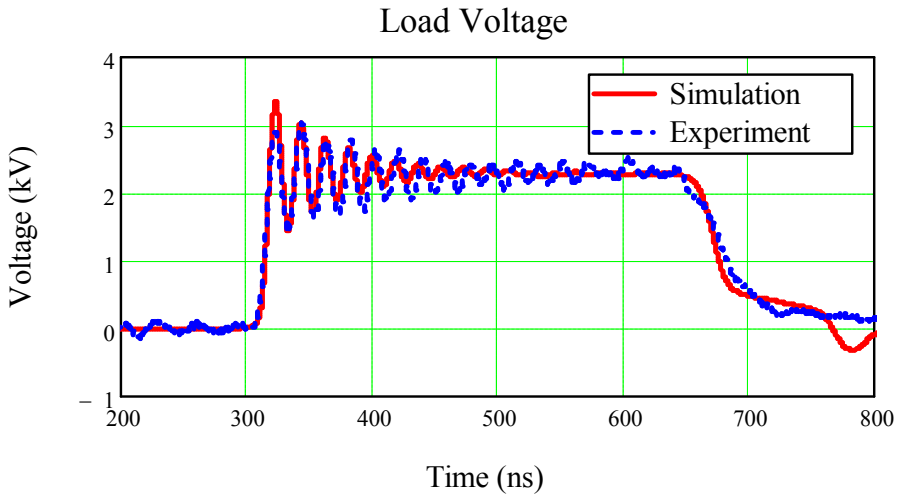

Figure 4.7 Load voltage vs. time for a 20-section NLIL without crosslink capacitor C_x (compared with simulation using L-I curve).

The time-frequency plots for the simulation and experimental results are shown in Figure 4.8. The frequencies obtained are close to the Bragg frequency limit of 58 MHz as defined in Eq.(4.2) where the saturation inductance is about 300 nH.

To see the quality of the load voltage modulation, the peak-to-trough oscillation amplitude V_{pt} is obtained for the first three cycles and is shown in the amplitude-cycle plot in Figure 4.9. The VMDs (as defined in Section 3.2.2) for simulation and experiment are VMD_{sim} = 1380 V and VMD_{expt} = 1174 V, respectively.

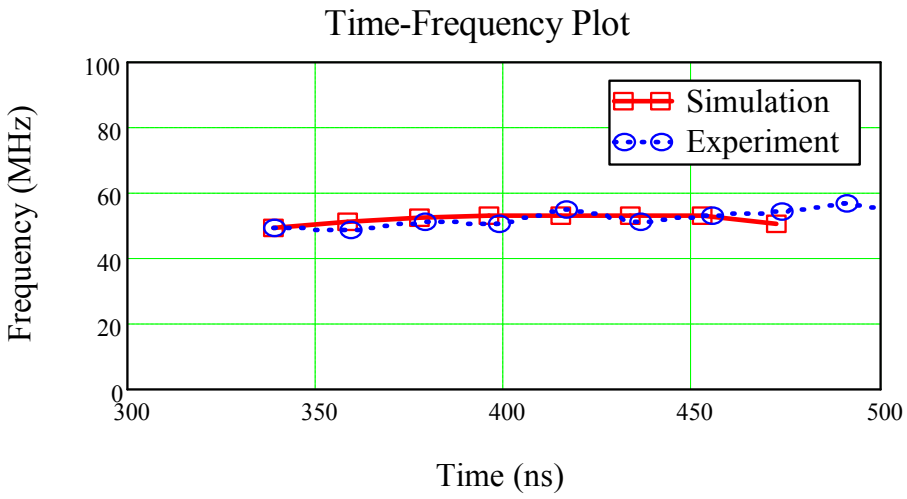

Figure 4.8 Voltage oscillation frequency vs. time for a 20-section NLIL without crosslink capacitor C_x (compared with simulation using L-I curve).

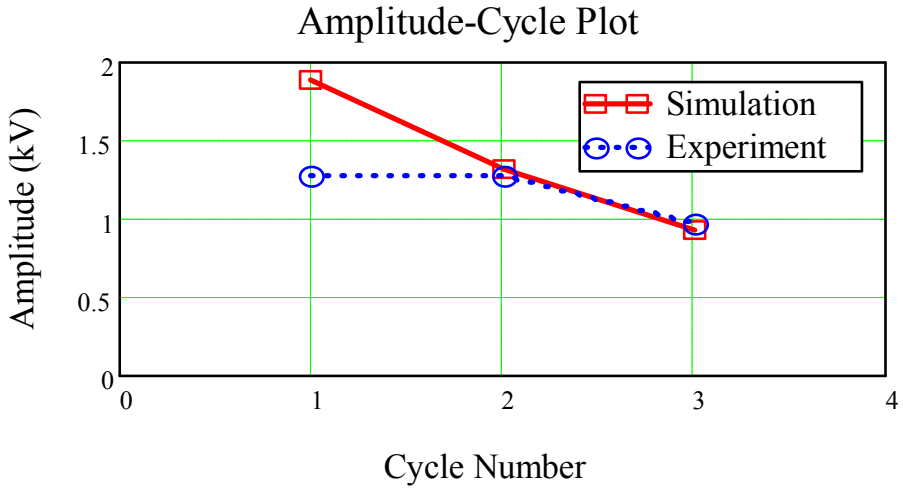

Figure 4.9 Peak-to-trough oscillation amplitude vs. oscillation cycle number for a 20-section NLIL without crosslink capacitor C_x (compared with simulation using L-I curve).

4.3.2 MODELING USING LANDAU-LIFSHITZ-GILBERT (LLG) EQUATION

The measured load voltage indicates a good agreement with the simulated result as shown in Figure 4.10.

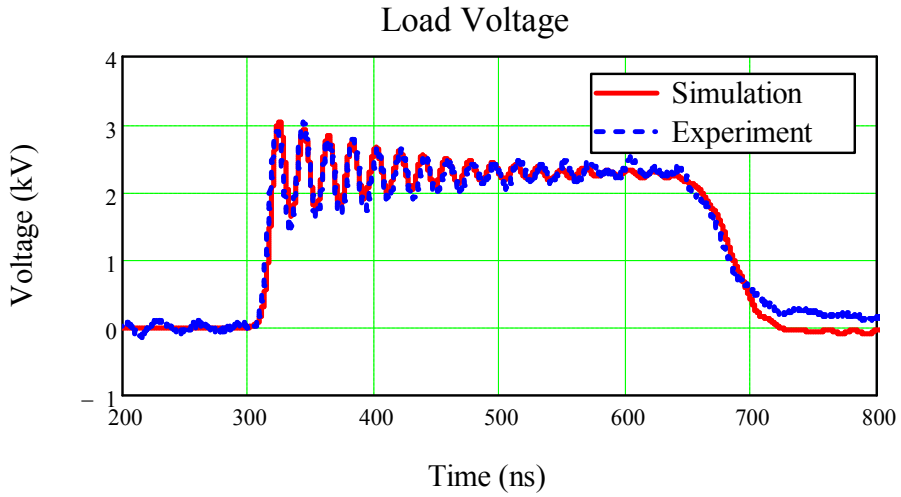

Figure 4.10 Load voltage vs. time for a 20-section NLIL without crosslink capacitor C_x (compared with simulation using LLG equation).

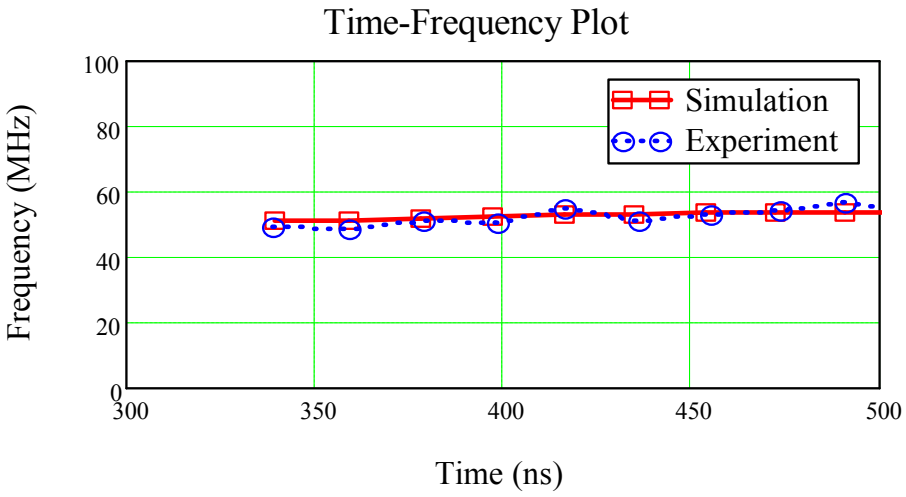

Figure 4.11 Voltage oscillation frequency vs. time for a 20-section NLIL without crosslink capacitor C_x (compared with simulation using LLG equation).

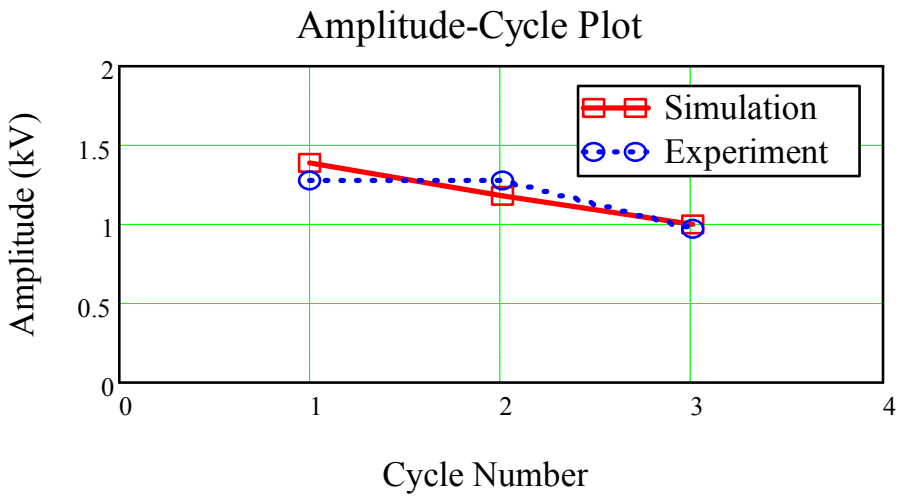

Figure 4.12 Peak-to-trough oscillation amplitude vs. oscillation cycle number for a 20-section NLIL without crosslink capacitor C_x (compared with simulation using LLG equation).

The time-frequency plots for the simulation and experimental results are shown in Figure 4.11. The frequencies obtained are close to the Bragg frequency limit of 58 MHz as defined in Eq.(4.2) where the saturation inductance is about 300 nH.

To see the quality of the load voltage modulation, the peak-to-trough oscillation amplitude V_{pt} is obtained for the first three cycles and is shown in the amplitude-cycle plot in Figure 4.12. The VMDs (as defined in Section 3.2.2) for simulation and experiment are VMD_{sim} = 1191 V and VMD_{expt} = 1174 V, respectively.

4.4 NLIL WITH CROSSLINK CAPACITORS

In an attempt to increase the number of oscillations, the number of LC sections was increased from 20 to 40. However, it is observed that, although the number of oscillations increases for the same input pulse, the amplitude of oscillations decreases. This is due to greater resistive damping as the pulse propagates through a longer line. To solve this problem, crosslink capacitors C_x are introduced into the line as shown in Figure 4.1.

4.4.1 THEORETICAL ANALYSIS

To understand how the operating frequency changes by varying the value of the crosslink capacitors C_x, the dispersion equation for the NLIL was derived with reference to a similar case in [95] (the steps are illustrated in Appendix D) and shown in Eq.(4.12) which has the same form given by Belyantsev [38]

$$\sin^2\left(\frac{\varphi}{2}\right) - 4\gamma\frac{\omega^2}{\omega_c{}^2}\sin^2(\varphi) = \frac{\omega^2}{\omega_c{}^2} \quad . \tag{4.12}$$

The coupling coefficient γ and critical frequency ω_c are defined as follows:

$$\gamma = \frac{C_x}{C_0} \tag{4.13}$$

$$\omega_c = \frac{2}{\sqrt{L_0 C_0}} \tag{4.14}$$

where L_0 is the inductance at saturation and C_0 is the linear capacitance.

By letting $\varphi = kd$, Eq.(4.12) becomes

$$\sin^2\left(\frac{kd}{2}\right) - 4\gamma\frac{\omega^2}{\omega_c{}^2}\sin^2(kd) = \frac{\omega^2}{\omega_c{}^2} \tag{4.15}$$

where we assume d is the distance between sections and k is the wave number.

The phase velocity v_p and group velocity v_g are then determined by

$$v_p = \frac{\omega}{k} = \frac{\omega d}{\varphi} \tag{4.16}$$

$$v_g = d\frac{d\omega}{d\varphi}. \tag{4.17}$$

For L_0 = 300 nH and C_0 = 100 pF, the dispersion curves are plotted using Eq.(4.15) for C_x = 0 pF, 22 pF, 47 pF and 94 pF in Figure 4.13 . By using $\omega = 2\pi f$ and assuming that d = 1 m here without loss of generality, the dispersion relations of frequency f vs wavenumber k are plotted. For comparison, the case for a lossless continuous transmission line (TL) is also included where the dispersion equation [62] is given by

$$\omega = \frac{k\omega_c}{2} \tag{4.18}$$

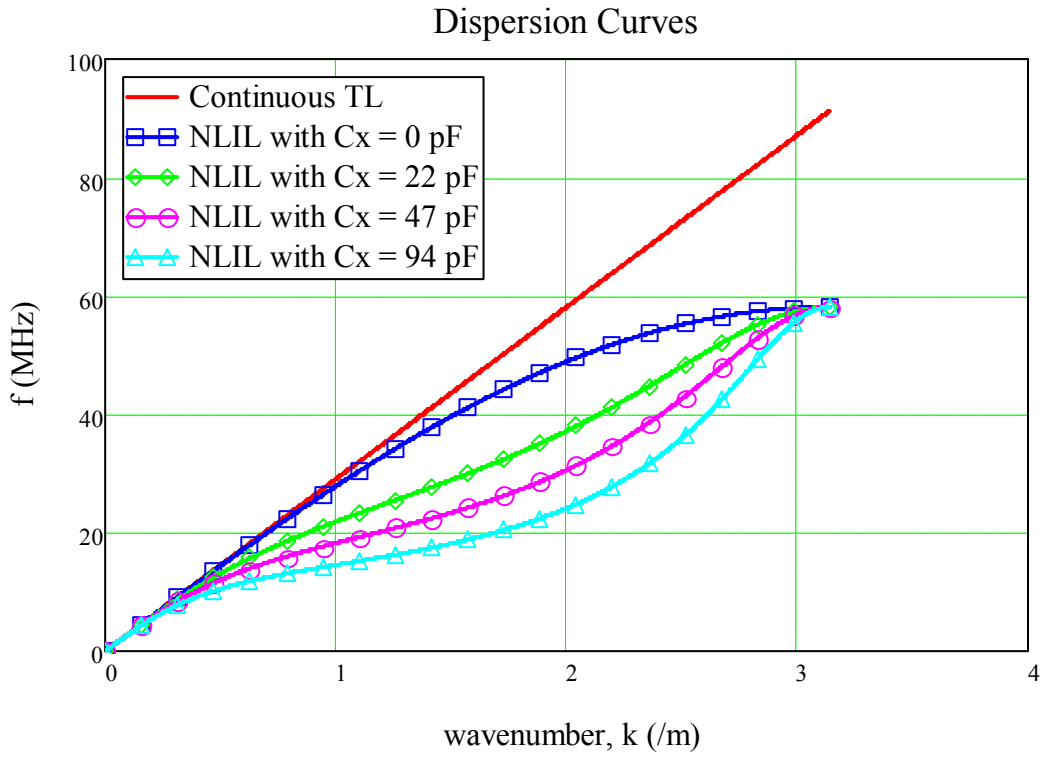

Figure 4.13 Dispersion curves (frequency vs. wavenumber) for NLIL.

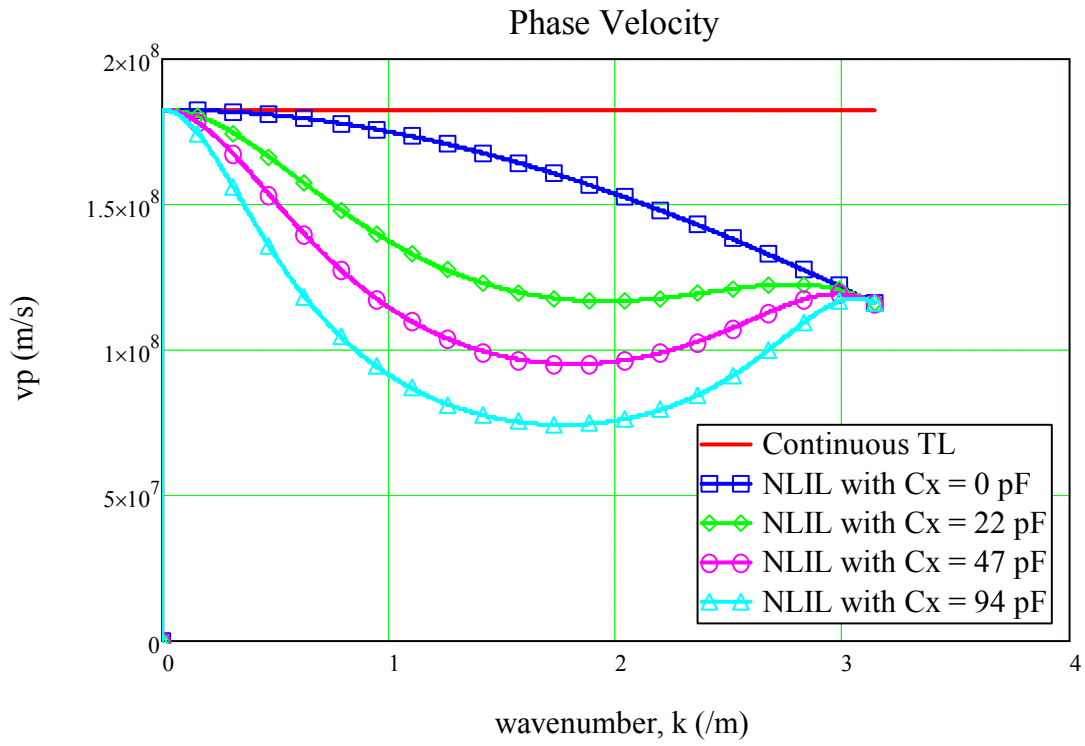

Figure 4.14 Phase velocity plots for NLIL.

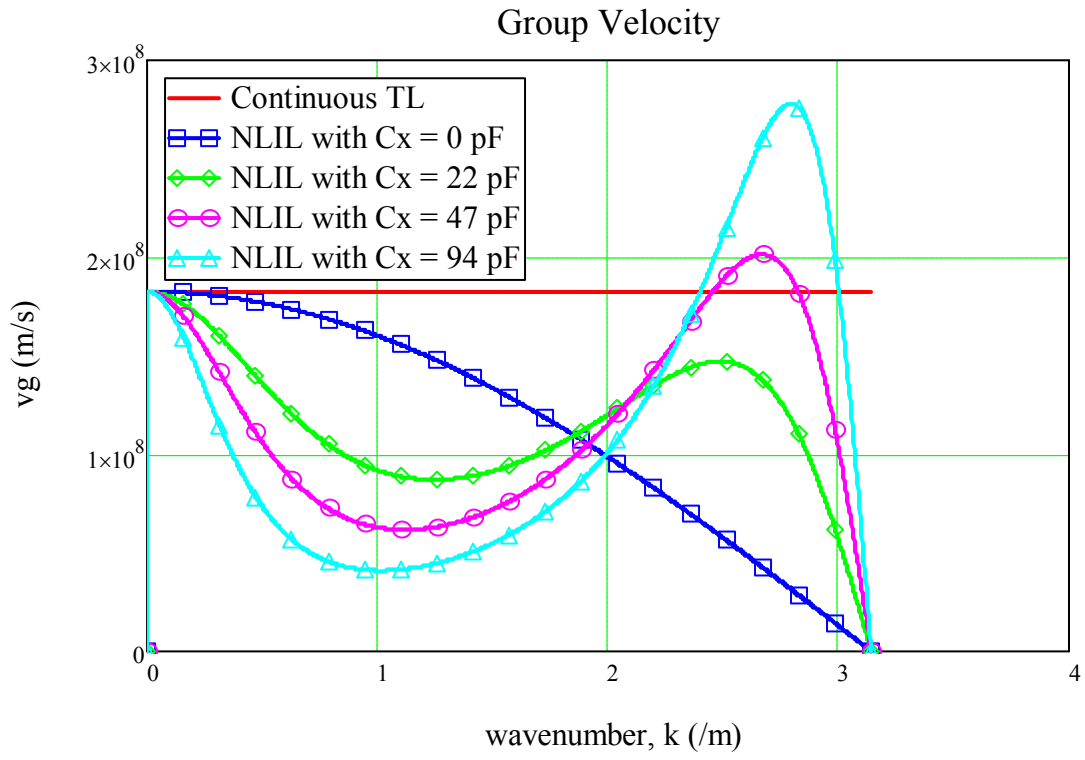

Figure 4.15 Group velocity plots for NLIL.

In Figure 4.13, it can be inferred that the discreteness of the NLIL without crosslink capacitors (i.e. C_x = 0 pF) makes the dispersion curve deviate from the linear form as exhibited by the case for a lossless continuous transmission line. It is also observed that by introducing crosslink capacitors, the shape of the dispersion curves can be modified (as shown by the curves with C_x = 22 pF, 47 pF and 97 pF).

Similarly, the phase velocities obtained using Eq.(4.16) are plotted in Figure 4.14 and the group velocities obtained using Eq.(4.17) are plotted in Figure 4.15 where they show similarity to the ones obtained in [38].

4.4.2 EXPERIMENTATION

For a pulse of 5 kV and a load of 50 Ω, a parameter sweep on C_x was simulated using the NLETL model that included the LLG equation. The curves for the voltage oscillation frequency (noted for second cycle) and VMD (as defined in Section 3.2.2) as C_x varies from 0 to 100 pF are plotted in Figure 4.16 and Figure 4.17, respectively. The case C_x = 0 pF corresponds to the NLIL without any crosslink capacitors.

The voltage oscillation frequency can also be predicted by using the dispersion equation in Eq.(4.12) and the dispersion curves (frequency versus phase shift) for C_x = 0 pF, 22 pF, 47 pF and 94 pF are plotted in Figure 4.18. From experiment, it was noted that frequency for the case without crosslink capacitors (i.e. C_x = 0 pF) is around 52 MHz. From the curve for C_x = 0 pF in Figure 4.18, this corresponds to a phase shift of 126°. As the phase shift is primarily determined by L_0 and C_o, it can be assumed that the phase shift remained constant with the addition of crosslink capacitors. Hence, by drawing a vertical line at phase 126° to intersect the curves in Figure 4.18, the frequencies for NLIL with C_x = 22 pF, 47 pF and 94 pF can

be estimated to be f = 41 MHz, 34 MHz and 27 MHz, respectively.

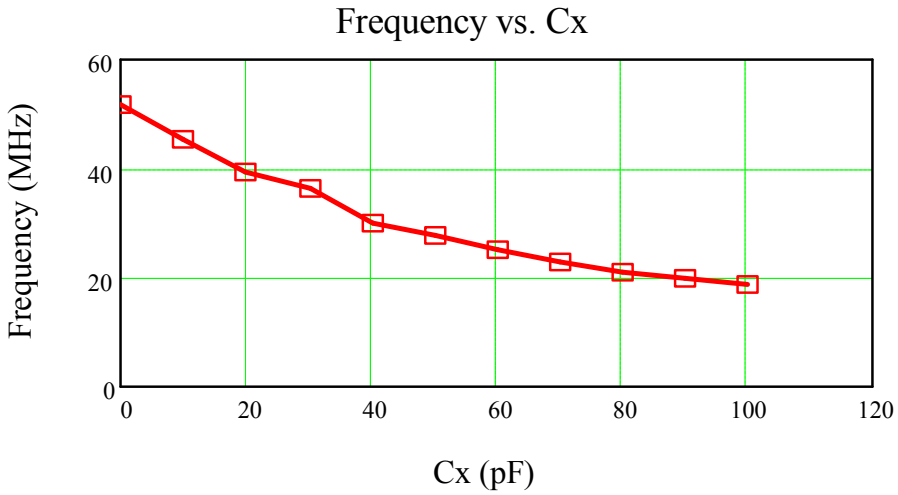

Figure 4.16 Voltage oscillation frequency vs. C_x for a 40-section NLIL (simulation).

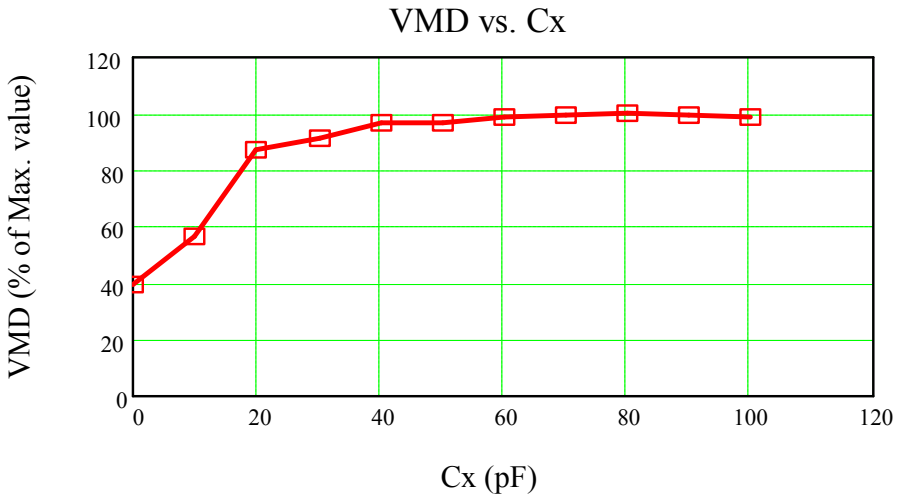

Figure 4.17 VMD (% of maximum value) vs. C_x for a 40-section NLIL (simulation).

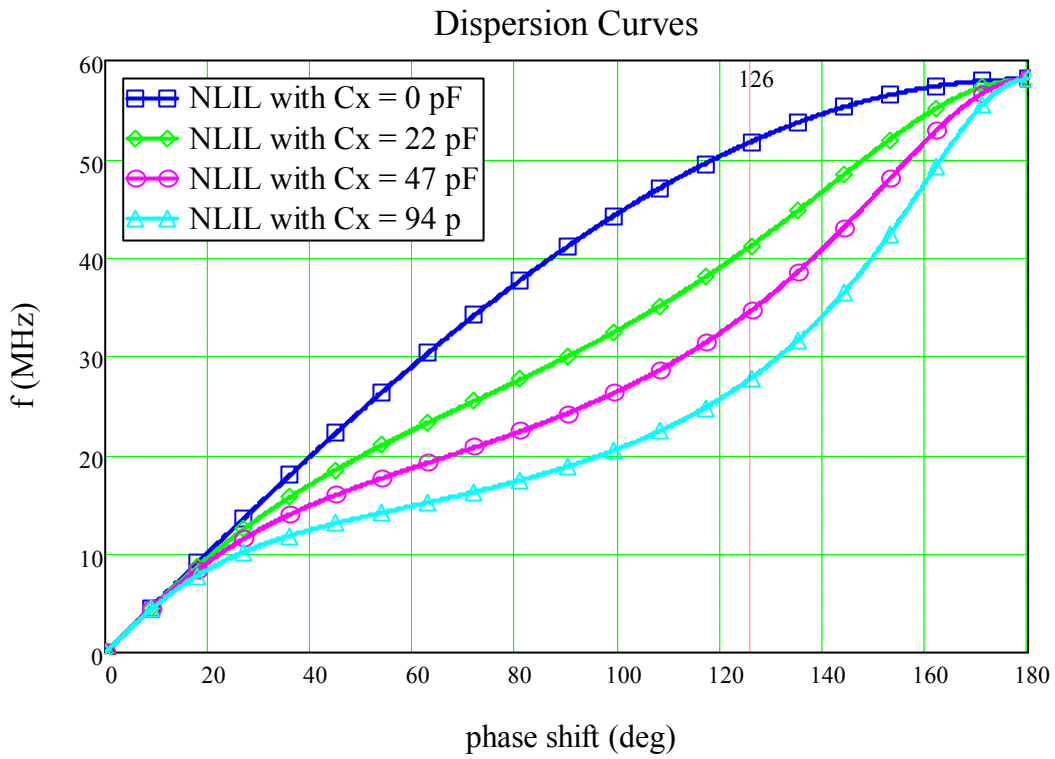

Figure 4.18 Dispersion curves (frequency vs. phase) for NLIL.

During experimentation, the pulser charged to 5 kV was used to inject a 400 ns duration pulse into the line with a 50 Ω load. The value of the crosslink capacitors was varied in discrete steps: C_x = 22 pF, 47 pF and 94 pF. These crosslink capacitors are ceramic capacitors from Murata and have capacitance tolerance of ± 5 %. A photograph of the experimental set-up is shown in Figure 4.19. Commercial high voltage probes were used to measure the node voltages at the main line capacitors. The input current to the NLIL was monitored with a commercial current probe. The load current was measured using either a commercial current probe or a current viewing resistor (CVR) which is indicated in the case for Figure 4.19. The load voltage waveforms were then calculated by multiplying the measured load current with the resistive load value and are presented in Figure 4.20. The case without C_x is also

included for reference. It is clear that the use of crosslink capacitors improves the amplitudes of oscillations.

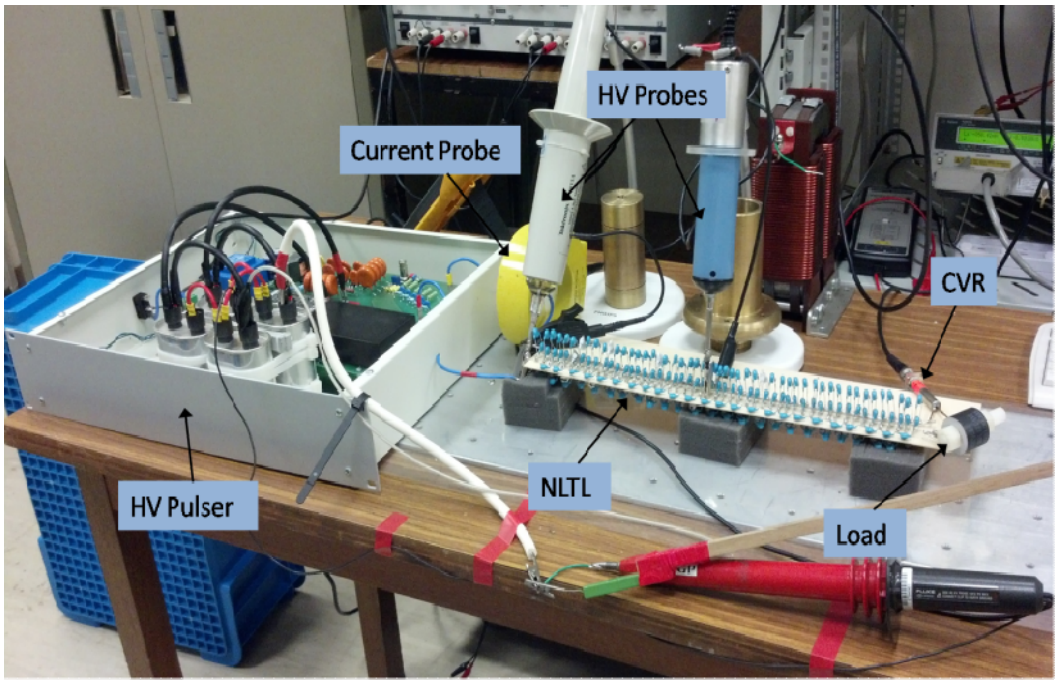

Figure 4.19 Photograph of a typical experimental set-up for a 40-section NLIL with cross-link capacitors C_x.

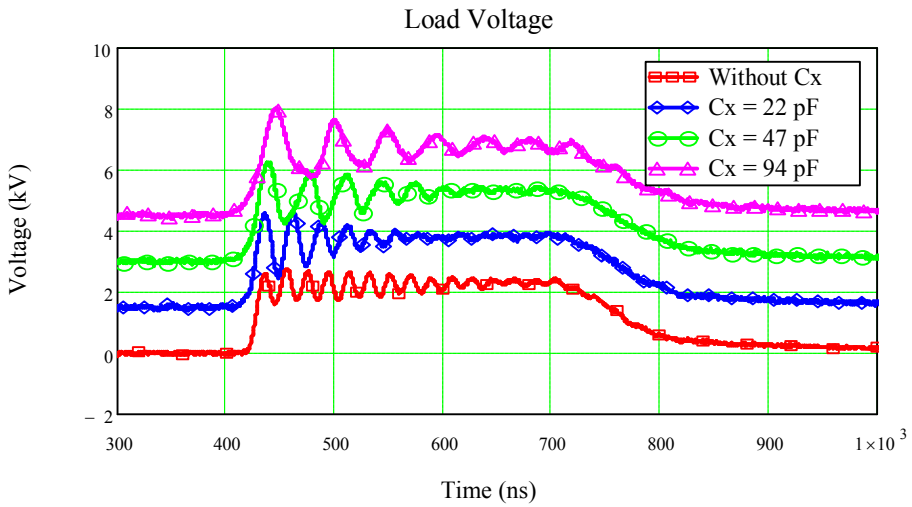

Figure 4.20 Load voltages vs. time for different C_x values (waveforms shifted for easy comparison) for a 40-section NLIL with C_x (expt.).

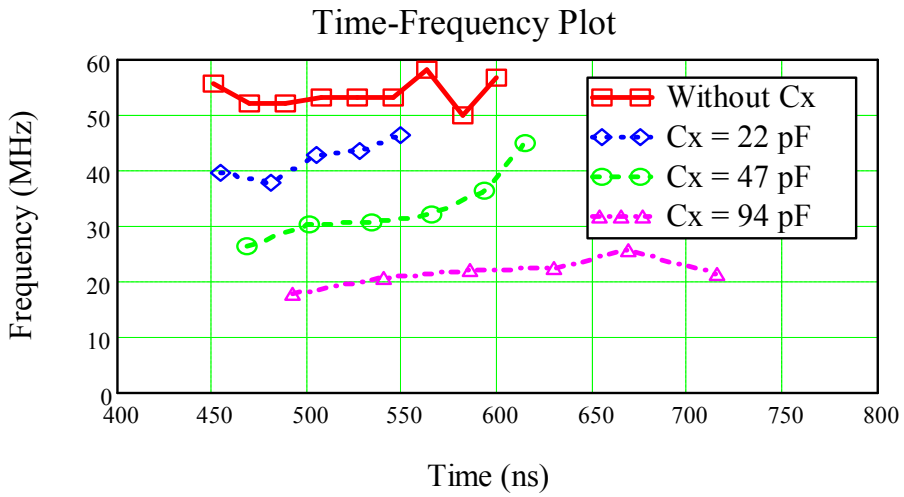

Figure 4.21 Voltage oscillation frequency vs. time for a 40-section NLIL with C_x (expt.).

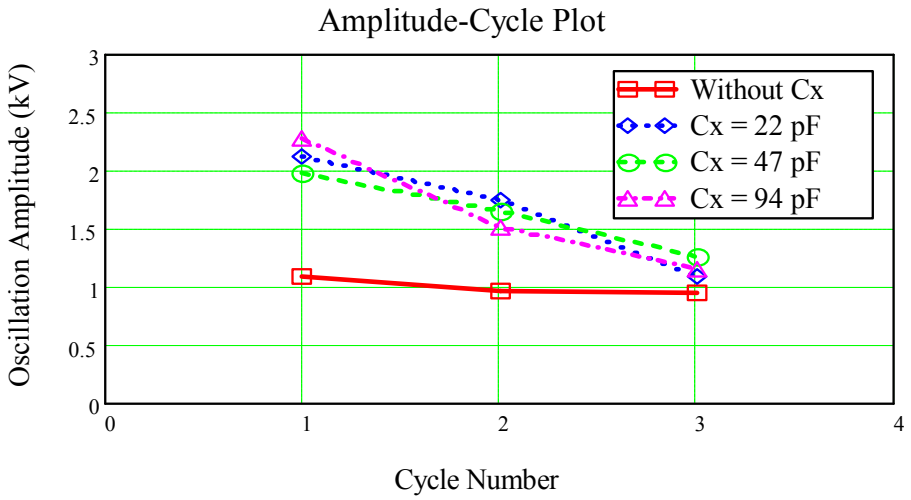

Figure 4.22 Oscillation amplitude vs. cycle number for a 40-section NLIL with C_x (expt.).

Nonetheless, analysis using the time-frequency plot in Figure 4.21 indicates that the frequencies of oscillations have been compromised. The oscillation frequencies decrease with the increase in the value of C_x. This is in close agreement with the simulation result in Figure 4.16. However, the experimental frequencies only show fairly good match to the ones predicted by using the dispersion equation. It

should be noted that the dispersion equation was derived based on a long line with many LC sections and that it is lossless.

In contrast, the amplitude-cycle plots in Figure 4.22 show little variation in the oscillation amplitudes when C_x increases. This trend also concurs with the simulated plot in Figure 4.17 where the VMD starts to level off at C_x = 20 pF. The optimal value for C_x seems to be at 40 pF as further increase in its value does not result in improvement in VMD. The simulated load voltage for the case C_x = 47 pF using the LLG equation in Eq.(4.8) indicates good agreement with the measured results as shown in Figure 4.23.

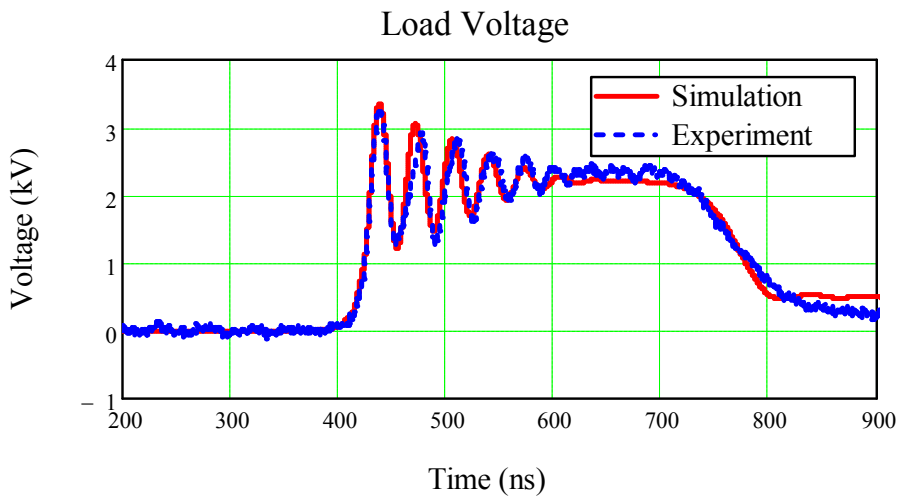

Figure 4.23 Load voltage vs. time for a 40-section NLIL with crosslink capacitor C_x = 47 pF.

4.5 CONCLUSIONS

By using COTS components, we have demonstrated that a simple pulser comprising a storage capacitor and a fast MOSFET semiconductor switch is capable of driving a NLIL to produce oscillating pulses at a repetition rate of up to 100 kHz. Two quick and convenient methods are proposed to characterize the nonlinear inductor made of ferrite bead for use in the NLETL circuit model. The first method is to derive the L vs. I curve from experiments and then apply it in the NLETL model. The second method involved obtaining the key parameters in the LLG equation from experiments where it is then incorporated into the circuit model. The simulation results for both methods show good agreement with the data from experiments.

Generally, increasing the number of sections in a basic NLIL will increase the number of oscillation cycles, but the amplitudes of oscillations will tend to decrease. By adding crosslink capacitors, the oscillation amplitudes can be increased substantially, but at the cost of having lower oscillation frequencies as the crosslink capacitance increases. Hence, to use NLIL without or with crosslink capacitors (and at what capacitance value) will depend on the user's requirement as there is a trade-off between VMD and frequency.

CHAPTER 5: NONLINEAR HYBRID LINE (NLHL)

5.1 INTRODUCTION

Conventional NLETL has only one of the nonlinear elements (either nonlinear capacitor or nonlinear inductor) and consequently, the impedance of the line will change with time causing unwanted reflections as line impedance is mismatched to the linear load. The concept of a nonlinear hybrid line (NLHL) is to have both the nonlinear elements in the line changing at the same rate so that the line impedance can be kept constant and matched to the linear load at all times. This chapter attempts to show that the NLHL will result in greater voltage modulation and higher frequency of RF oscillations. Hence, for the same desired output, it is projected that a system based on NLHL can be made more compact than one with the conventional NLETL.

The idea of a nonlinear hybrid line (NLHL) where both capacitors and inductors are nonlinear was first proposed by Fallside [96] in 1966 for pulse sharpening and Zucker [97] showed theoretically in 1976 that the NLHL has greater energy compression per stage than a line with either nonlinear capacitance or nonlinear inductance. Gaudet [8] then suggested using the NLHL to achieve RF generation in 2008. There is even greater motivation now to explore the hybrid line for RF generation as Smith [81] recently showed that there are some fundamental physical problems that limit the performance of the usual NLCL; in particular, the loss in the

dielectric material limits the operating frequencies to below 100 MHz. To date, research work on generating RF pulses using NLHL has been confined to modeling and simulation [43] and [44]; no experimental result on NLHL has been reported to date. Sanders [82] has intended to build a hybrid line using ferrite beads and capacitors with X7R dielectric (which is expected to exhibit a capacitance decrease of 30%) but he actually checked that the capacitors did not exhibit any significant capacitance changes.

5.1.1 THEORY

The underlying principle for implementing a NLHL is to create a constant characteristic impedance line to match to the resistive load by finding the right combination of the nonlinear functions *C(V)* and *L(I)* of the capacitors and inductors, respectively. It is possible to build such a hybrid line if the functions *C(V)* and *L(I*) are tailored such that the characteristic impedance of the line remains constant according to Eq.(1.3). We adopt here the exponential form of the functions for the nonlinear components that is slightly modified from the one derived by Fallside [96] based on a first-harmonic approximation analysis of nonlinear delay lines. His work actually focuses on pulse sharpening of the rise time, but his equations for a constant impedance line will be used here to study the NLHL for RF generation. For a line to have constant characteristic impedance, the functions *L(I)* and *C(V*) must be related so that the equation

$$Z = \sqrt{\frac{L(I)}{C(Z \cdot I)}} \tag{5.1}$$

has at least one solution for *Z* which is independent of *I*. An example is a line with exponential functions

$$C = C_0 \cdot e^{-q \cdot V} \tag{5.2}$$

$$L = L_0 \cdot e^{-p \cdot I} \,. \tag{5.3}$$

Substituting Eq.(5.2) and Eq.(5.3) into Eq.(5.1) yields

$$Z = \left(\frac{L_0}{C_0} \right)^{1/2} e^{-\frac{1}{2}(pI - qZI)} \,. \tag{5.4}$$

Then $Z = Z_0$ exists only if [96]

$$Z_0 = \frac{p}{q} = \left(\frac{L_0}{C_0} \right)^{1/2} \,, \tag{5.5}$$

where,

C – capacitance as a function of voltage V

L – inductance as a function of current I

C_0 – initial capacitance (at zero voltage)

L_0 – initial inductance (at zero current)

p, q – nonlinearity factors.

In reality, the capacitance and inductance approach asymptotic values as the nonlinear elements saturate. Hence, the nonlinear functions in Eq.(5.2) and Eq.(5.3) can be enhanced to the form similar to Eq.(2.12) to give

$$C = C_0 \cdot \left[x + (1 - x) \cdot e^{-q \cdot V} \right] \tag{5.6}$$

$$L = L_0 \cdot \left[y + (1 - y) \cdot e^{-p \cdot I} \right] . \tag{5.7}$$

Similarly, by substituting Eq.(5.6) and Eq.(5.7) into Eq.(5.1), $Z = Z_0$ is found to exist (for small values of x and y) only if $x = y$ and Eq.(5.5) is satisfied. The values x

and *y* are dimensionless and have typical values between 0 and 0.3. The forms in Eq.(5.6) and Eq.(5.7) are useful as the asymptotic values are given by the fraction *x* multiplied by initial capacitance C_0 and the fraction *y* multiplied by initial inductance L_0.

In the study of the hybrid line here, it is assumed that the resistive losses R_L and R_C are neglected. The capacitive nonlinear parameters are chosen as $C_0 = 816.14$ pF, $q = 0.3$ V^{-1} and $x = y = 0.001$. For $Z_0 = 50$ Ω, using Eq.(5.5) gives the inductive parameters $L_0 = 2.04$ μH and $p = 15$ A^{-1}. The other simulation parameters are similar to those in Section 2.1. For comparison, a nonlinear capacitive line (NLCL) with constant inductor value of L_0 and a nonlinear inductive line (NLIL) with constant capacitor value of C_0 are also simulated.

5.1.2 HYBRID LINE WITHOUT BIASING

The output load voltage and characteristic impedance of the last LC section are depicted in Figure 5.1 and Figure 5.2, respectively. It is interesting to note that the output voltages of the NLCL and NLIL are observed to be identical. This is due to their nonlinear elements having similar exponential functions in Eq.(5.6) and Eq.(5.7) which are being tied to the impedance relationship in Eq.(5.4).

In Figure 5.2, the characteristic impedances are calculated using Eq.(1.3) and all the lines have Z_0 = 50 Ω in the unsaturated state where capacitor voltage and inductor current are both zeroes. For NLCL, the characteristic impedance varies from 50 Ω to above 50 Ω as *L(I)* is constant and *C(V)* decreases. Similarly, characteristic impedance of NLIL varies from 50 Ω to below 50 Ω as *C(V)* is constant and *L(I)* decreases. For a hybrid line, the characteristic impedance oscillates around Z_0 = 50 Ω as *C(V)* variation is more or less compensated by *L(I)* changes. It is observed that the

timings for the peaks and troughs of the load voltage for the hybrid line in Figure 5.1 correspond to the timings for characteristic impedance of 50 Ω in Figure 5.2 as can be seen by putting the relevant waveforms together in Figure 5.3. This means that as the characteristic impedance of the last section changes with time, it will, at a matched condition of 50 Ω, produce maximum voltage swing at the load.

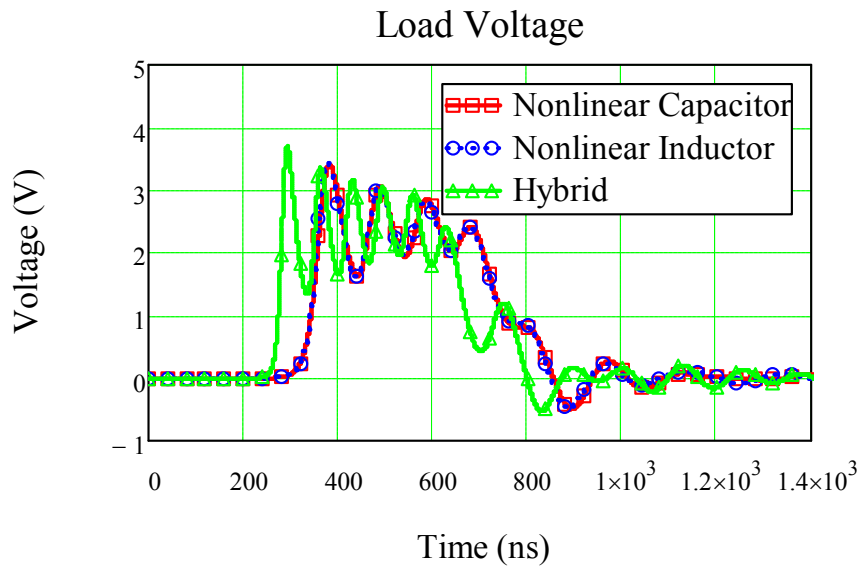

Figure 5.1 Output voltages for NLCL, NLIL, and hybrid line (V_{pump} = 5 V, n = 10, R_{load} = 50 Ω).

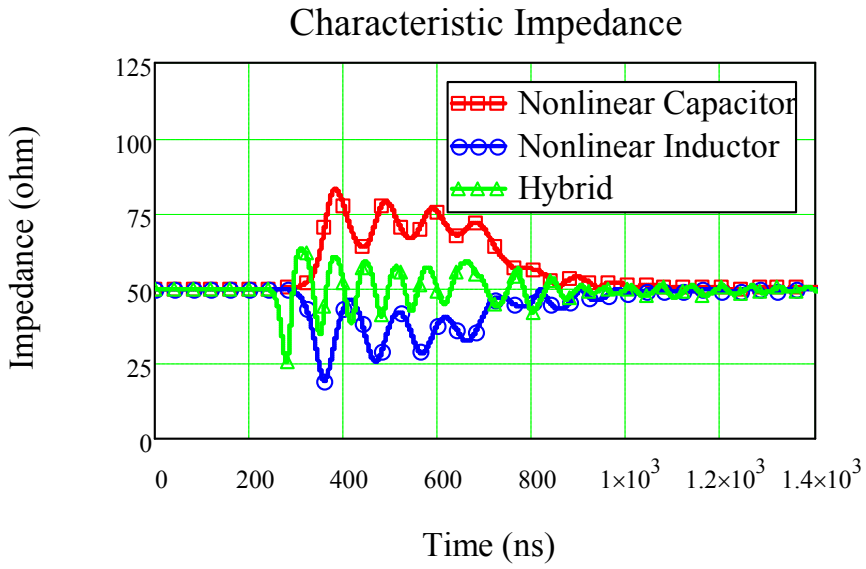

Figure 5.2 Time variation of characteristic impedance of the last LC section for NLCL, NLIL, and hybrid line (V_{pump} = 5 V, n = 10, R_{load} = 50 Ω).

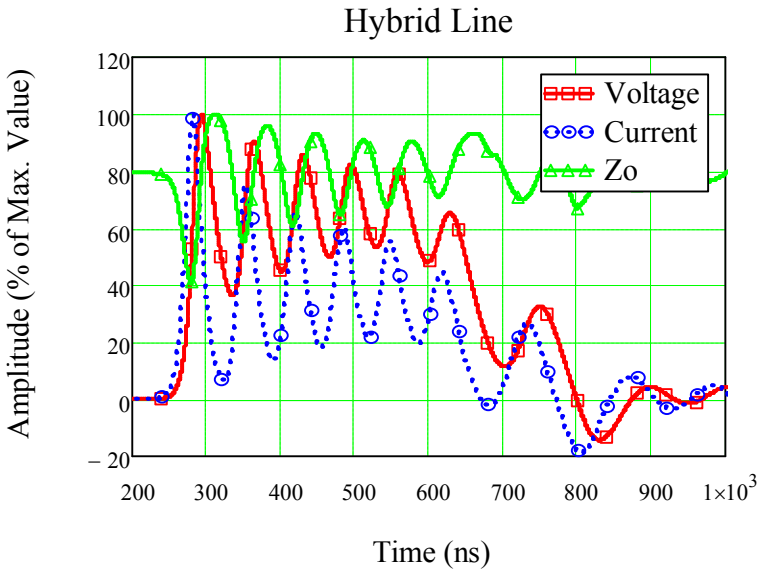

Figure 5.3 Capacitor voltage, inductor current and characteristic impedance waveforms of the last LC section for hybrid line (V_{pump} = 5 V, n = 10, R_{load} = 50 Ω).

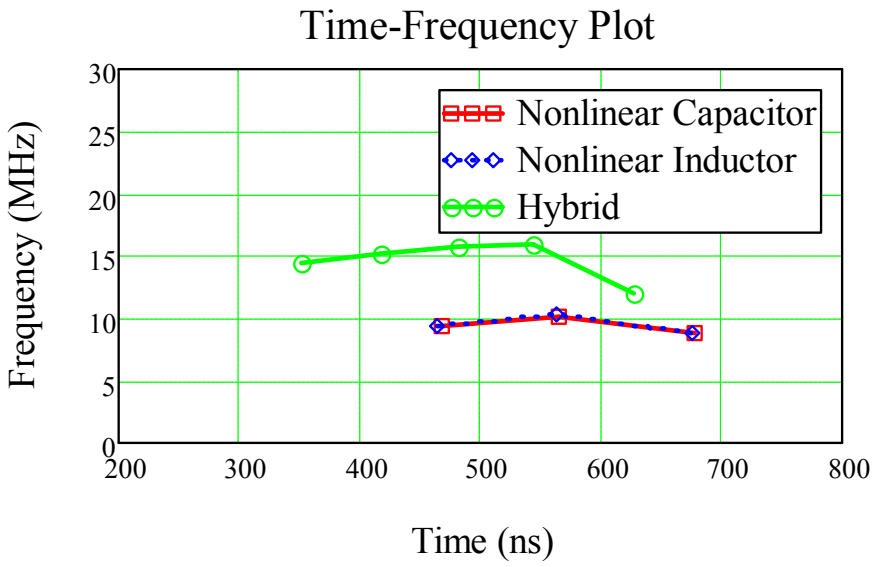

Figure 5.4 Voltage oscillation frequency vs. time for NLCL, NLIL, and hybrid line (V_{pump} = 5 V, n = 10, R_{load} = 50 Ω).

From the time-frequency plot in Figure 5.4, the NLCL and NLIL have three cycles of oscillation at about 10 MHz whereas the hybrid line has 5 cycles of oscillations at 15 MHz. In this study, the hybrid line has a slightly higher peak voltage

and a higher oscillation frequency than NLCL and NLIL. Referring to the PSpice soliton simulation results from Rossi [44], he also obtained an increase in frequency with hybrid line but with lower voltage peak amplitude compared to a standard NLCL. This discrepancy is probably due to the particular functions assumed for *L(I)* and *C(V)*.

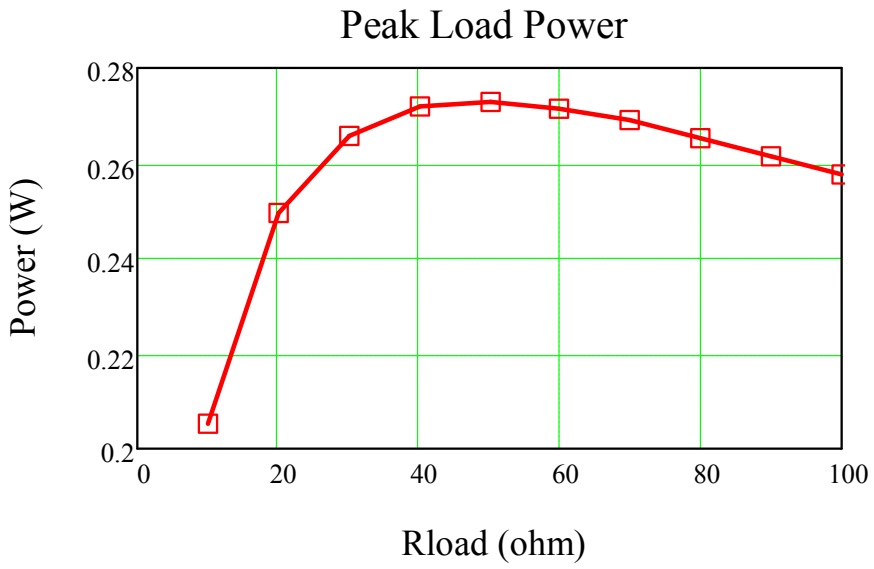

Figure 5.5 Peak power as a function of R_{load} for a hybrid line (V_{pump} = 5 V, n = 10).

By varying the value of the load, the hybrid line shows that the peak power has an optimum point at R_{load} = 50 Ω (Figure 5.5). This verifies the design objective of having a constant impedance hybrid line to match the load at all times, although this is only approximate since the characteristic impedance actually oscillates about the load value of 50 Ω, as shown in Figure 5.2. However, the optimum point for peak load power only exists for input pump pulse of amplitude up to 8 V. Above 8 V, the peak load power begins to decrease exponentially as the resistive load increases. This could be due to the onset of higher harmonic terms in the analysis of delay line by Fallside [96] that become significant at high saturation voltages. It seems that at high input voltage close to the saturation voltage, a lower value resistive load is preferred for high peak power operation.

5.1.3 HYBRID LINE WITH BIASING

To investigate the effects of biasing the nonlinear elements, the functions *C(V)* and *L(I)* in Eq.(5.6) and Eq.(5.7) respectively, are modified as follows:

$$C = C_0 \cdot \left[x + (1-x) \cdot e^{-q \cdot (V_{bias} + V)} \right] \tag{5.8}$$

$$L = L_0 \cdot \left[y + (1-y) \cdot e^{-p \cdot (I_{bias} + I)} \right] \tag{5.9}$$

where

V_{bias} *– bias voltage applied to nonlinear capacitor*

I_{bias} *– bias current applied to nonlinear inductor.*

For a bias voltage applied to the nonlinear capacitors in the hybrid line, the corresponding bias current applied to the nonlinear inductors at the same time is given by

$$I_{bias} = \frac{V_{bias}}{Z_0} . \tag{5.10}$$

In the simulations here, it is assumed that the hybrid line is lossless and biasing is applied separately in which the biasing circuits are isolated from the hybrid line. In practice, the biasing circuit may be connected to the line and may affect, to a certain degree, its performance. Hence, care must be taken in designing the biasing circuits which is an art in itself to ensure sufficient isolation and the design will involve trade-offs between complexity and performance. Examples of simple biasing circuits for the capacitor in the hybrid line can be similar to the one shown in Figure 3.11 and Figure 3.34. A nonlinear inductor can be built by winding a wire around a toroidal magnetic core. The biasing circuit for the nonlinear inductor can then be implemented by winding another wire on another part of the same core and connected to a DC source. This makes a good biasing circuit as biasing is applied through magnetic coupling and it is electrically isolated from the hybrid line.

Due to the similarity between NLCL and NLIL which gives identical results, only the results from the NLCL are compared with those from the hybrid line under the condition of biasing. The output voltages at different bias voltages for NLCL and hybrid line are depicted in Figure 5.6 and Figure 5.7, respectively. The oscillation amplitudes decrease with increasing bias voltage for the NLCL whereas the oscillation amplitudes remain the same with both increasing bias voltage and bias current for the hybrid line. Both lines show increase in output frequency with increase in biasing. For bias voltage of 0 to 5 V, the time-frequency plot in Figure 5.8 indicates that NLCL can have frequency variation of 10 to 21 MHz. On the other hand in Figure 5.9, the hybrid line shows a much greater frequency range of 15 to 70 MHz for the same bias voltage variation (with corresponding bias current). It is also noted that the hybrid line also produces many more cycles of oscillation as seen from the number of symbols in the graph.

Hence, a hybrid line that is designed to have constant impedance can have a much wider range of frequency tunability and greater number of cycle of oscillations compared to either the NLCL or NLIL. The hybrid line also produces oscillations that do not degrade in oscillation amplitudes when the biasing values are increased. However, in practice, losses need to be taken into account for the nonlinear elements. For the nonlinear capacitor, the equivalent series resistor has to be kept small. For the nonlinear inductor, the hysteresis loss and eddy current loss in the magnetic core material need to be minimized.

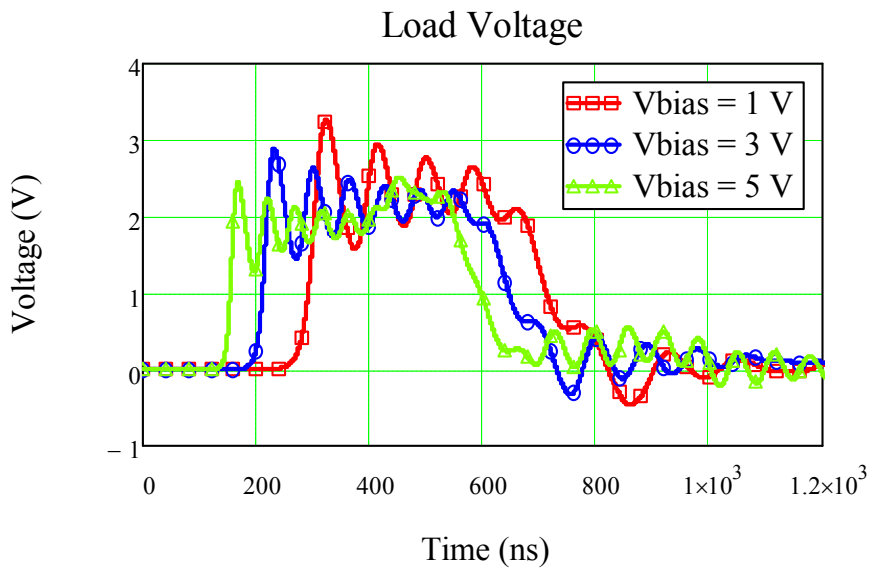

Figure 5.6 Output voltages for NLCL at different bias voltages (V_{pump} = 5 V, n = 10, R_{load} = 50 Ω).

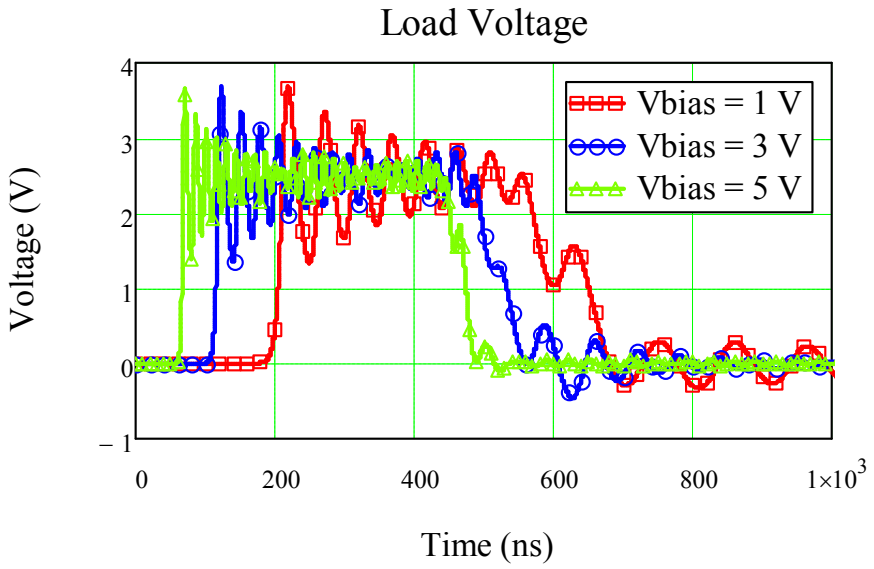

Figure 5.7 Output voltages for hybrid line at different bias voltages and corresponding bias currents of 0.02 A, 0.06 A and 0.1 A (V_{pump} = 5 V, n = 10, R_{load} = 50 Ω).

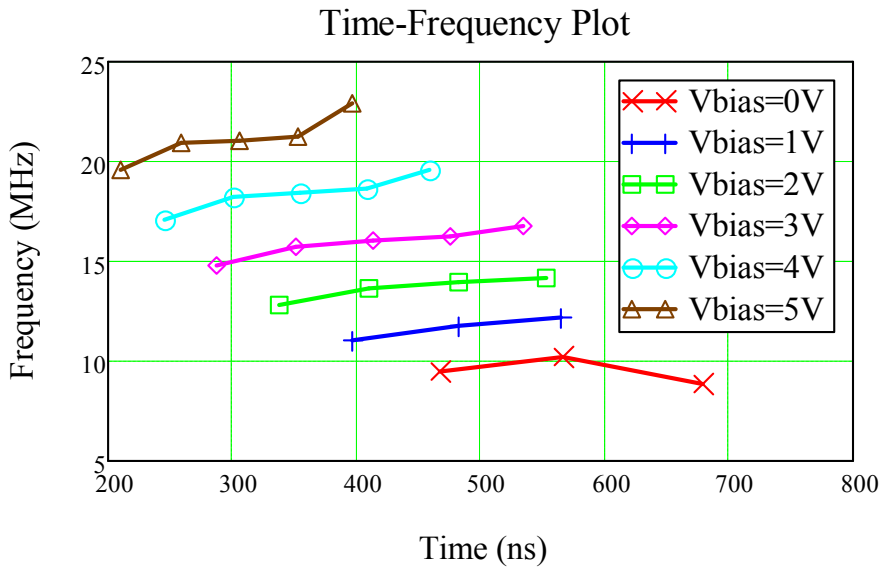

Figure 5.8 Voltage oscillation frequency vs. time for NLCL at different bias voltages (V_{pump} = 5 V, n = 10, R_{load} = 50 Ω).

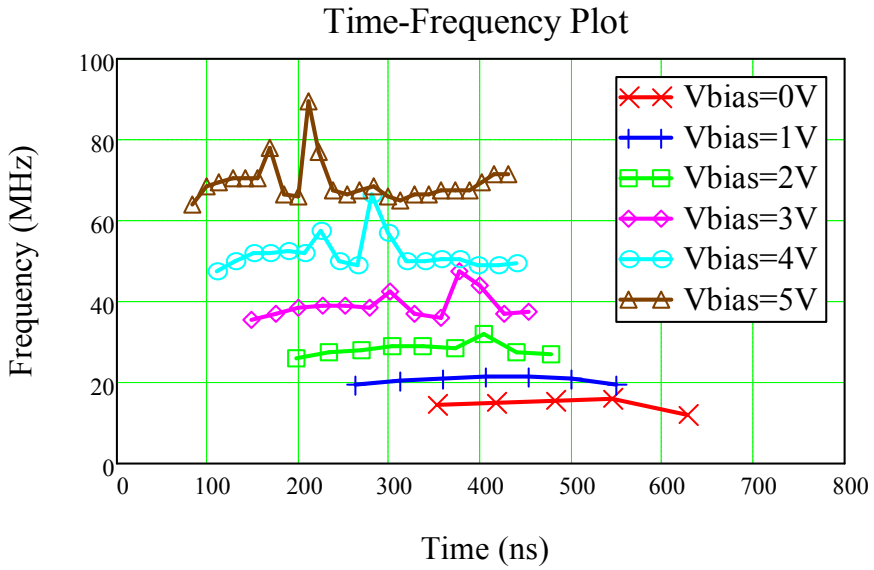

Figure 5.9 Voltage oscillation frequency vs. time for hybrid line at different bias voltages and corresponding bias currents of 0 A, 0.02 A, 0.04 A, 0.06 A, 0.08 A and 0.1 A (V_{pump} = 5 V, n = 10, R_{load} = 50 Ω).

5.2 TESTING OF NLHL

This section describes the experimental work carried out in building and testing a high voltage NLHL by using commercial-off-the-shelf (COTS) components. The design of the NLHL was made possible by using the NLETL circuit model developed in Chapter 2 that is well validated by experiments in Chapter 3 and Chapter 4. Results simulated by the NLETL model show fairly good match to the data obtained from the experiments described in this section. In order to better quantify the oscillating pulses, the voltage modulation and the frequency content of the pulses are carefully analyzed using amplitude-cycle and time-frequency plots.

The NLHL was built using COTS components and the circuit diagram for setting up the experiment is depicted in Figure 5.10. It shows a high voltage (HV) pulse generator circuit connected to a nonlinear LC ladder network with resistive load R_{load} = 50 Ω. Instead of using a pulse generator that involves a pulse forming network or pulse forming line [41], or one with complex architecture [82], we have implemented a much simpler pulse generator with only a few key components. It comprises a HV power supply, a storage capacitor C_{st} = 1 μF, a fast HV MOSFET semiconductor switch and a current limiting resistor R_{gen} = 50 Ω. This pulse generator can be charged up to 10 kV and produces an output waveform that is almost rectangular in shape. The output pulse duration is adjusted to about 600 ns (controlled by the low voltage trigger pulse) and has a typical rise time of 47 ns and fall time of 44 ns at 6 kV.

The NLHL in Figure 5.10 consists of *n* number of LC sections in which each section contains a single *L* connected to a single *C*. The *L* and *C* components were chosen by utilizing the nonlinear capacitors (the ones that give the best performance) used in the high voltage NLCL as described in Section 3.2.1 and the nonlinear

inductors (the ones that give the best performance) used in the NLIL as described in Section 4.2. The objective is to further validate the NLETL model and demonstrate that hybrid line can work and give better performance.

The nonlinear capacitive element C in the line is a Murata DEBF33D102ZP2A ceramic capacitor rated at 1 nF and 2 kV. For the nonlinear inductive element L in the line a Fair-rite 2944666651 ferrite bead made of NiZn is used. In order to characterize the nonlinear capacitor and nonlinear inductor made from the ferrite bead under dynamic conditions at the time scale of operation of the NLHL, the pulse generator was connected directly to the nonlinear component under test with R_{gen} = 100 Ω. The characterization circuit is illustrated in Figure 5.11 where the voltage (V_C or V_L) across the nonlinear component and the current I_{gen} flowing through it are measured.

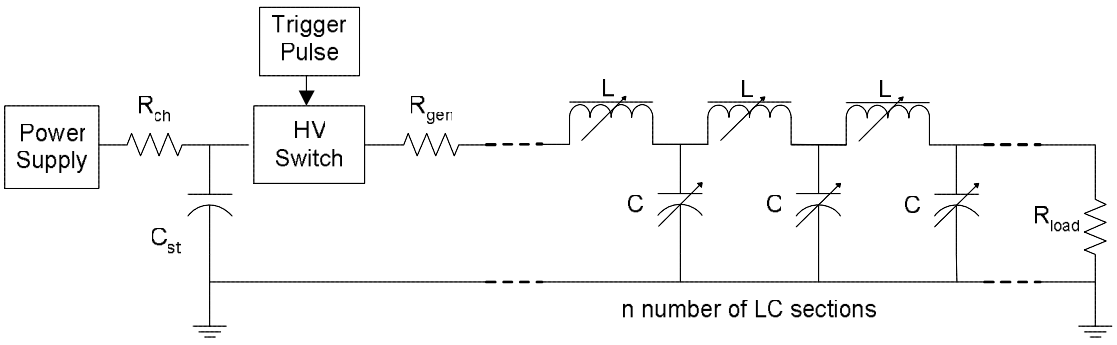

Figure 5.10 Experimental set-up of a NLHL.

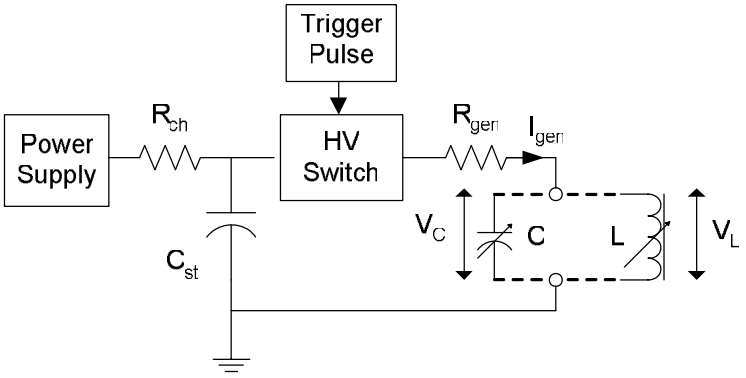

Figure 5.11 Circuit used for measuring the C-V curve of a nonlinear capacitor and the L-I curve of a nonlinear inductor.

To obtain the C-V curve (similar to the method used in Section 3.2.1), the pulse generator was used to discharge a 6 kV pulse into the capacitor. The nonlinear differential capacitance can be calculated using

$$C = \frac{dQ}{dV} = \frac{dQ/dt}{dV/dt} = \frac{I_{gen}}{dV_c/dt} \tag{5.11}$$

where Q is the charge in the capacitor C. The experimental C-V curve was then curve fitted using Eq.(5.6). For best fit, the parameters obtained for equation Eq.(5.6) are C_0 = 0.995 nF, x = 0.11 and q = 1.583 x 10^{-3} V^{-1}. By using these parameters, Eq.(5.6) is plotted in Figure 5.12 with voltage varying up to 6 kV and used in the NLETL model.

Likewise, to obtain the L-I curve (similar to the method used in Section 0), an 8 kV pulse was discharge into the ferrite bead from the pulse generator. First, the flux linkage Ψ in the ferrite bead is derived using

$$\Psi(t) = \int V_L(t)dt\ , \tag{5.12}$$

where V_L is the voltage across the inductor.

The characteristic dynamic Ψ-I curve of the nonlinear inductor was plotted and a curve fit was performed on the curve by using an exponential function. The curve fit function for Ψ was then differentiated with respect to current I to obtain the

differential inductance L_d that has the exponential form given in Eq.(5.7). For L_d function, the parameters obtained are L_0 = 2.08 μH, y = 0.033, p = 0.169 A^{-1} and Eq.(5.7) is plotted in Figure 5.13 by using these parameters up to a current of 80 A. For comparison, the matching inductance function L_m for L-I curve to go with the capacitance function for C-V curve with Z_0 = 50 Ω can be found by calculating the parameters using Eq.(5.5). For L_m function, the parameters obtained for Eq.(5.7) are L_0 = 2.49 μH, y = 0.11, p = 0.079 A^{-1} and the corresponding equation is also plotted in Figure 5.13. The functions L_d and L_m with the exponential form shown in Eq.(5.7) are used in the NLETL model for circuit simulations.

It should be noted that the measurements for nonlinear inductor were made on the ferrite bead condition with B-H hysteresis curve in the first quadrant. In our case it was observed during experiment that the results for the line without pre-shot reset current to the ferrite beads are better than those with pre-shot reset current. Hence, only experiments performed with the NLHL without pre-shot reset current are described in this chapter. Reset current was applied by connecting in series a 20 V DC power supply and a 10 Ω resistor to the first and last inductors of the line.

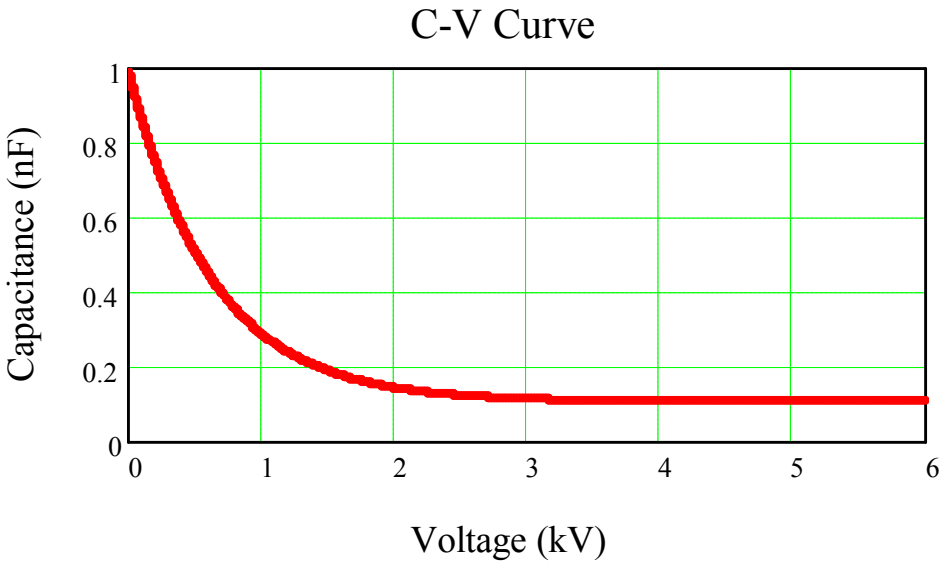

Figure 5.12 C vs. V curve obtained for the nonlinear capacitor.

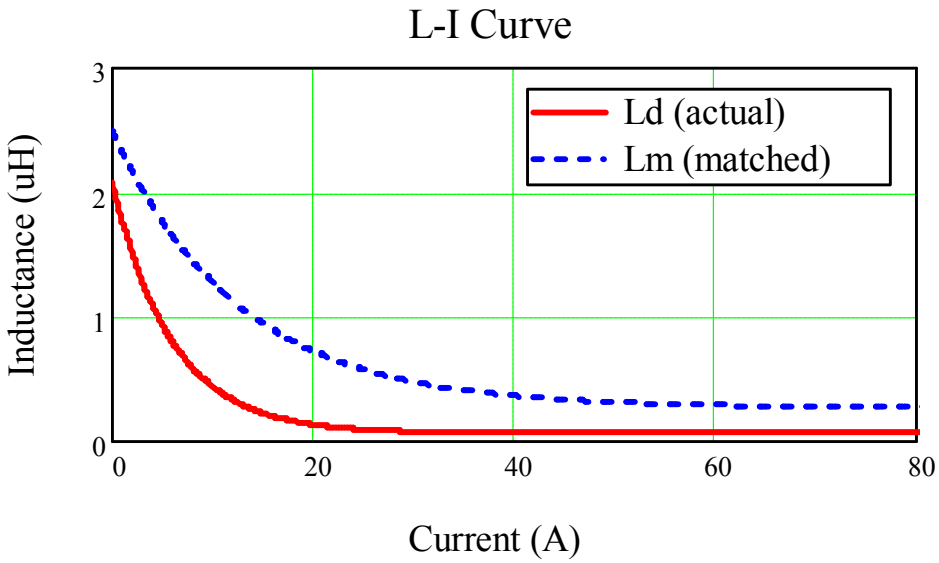

Figure 5.13 L vs. I curve obtained for the nonlinear inductor.

5.3 RESULTS OF NLHL

This section analyzes the results of a 20-section NLHL with R_{load} = 50 Ω as described in Figure 5.10. The pulse generator is charged to 6 kV and a discharge pulse of 600 ns duration with approximately rectangular shape is injected into the NLHL. A photograph of the experimental set-up is shown in Figure 5.14.

We use here the average peak load power P_{ave} and voltage modulation depth (VMD) as defined in Section 3.2.2. In order to find the load that best matches to the line in terms of P_{ave}, a parameter sweep on the load was performed using the NLETL simulation model. The load of 50 Ω was chosen as it gives peak power near to the maximum point in the sweep. The measured load voltage indicates a fairly good agreement with the simulated result (by means of L_d) as shown in Figure 5.15. The simulated matched case using L_m is also depicted in Figure 5.15 for comparison.

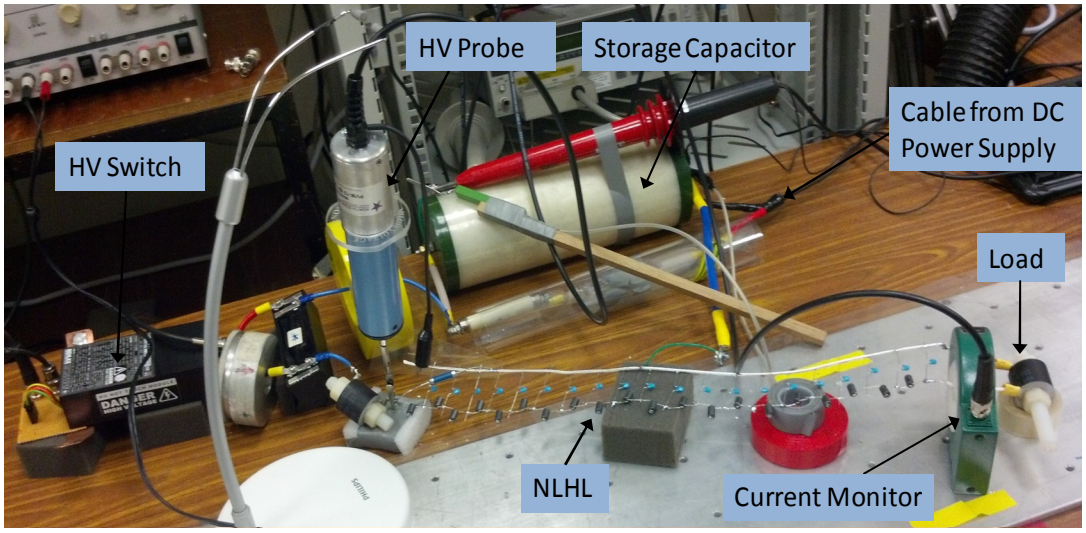

Figure 5.14 Photograph of a typical experimental set-up for a 20-section NLHL.

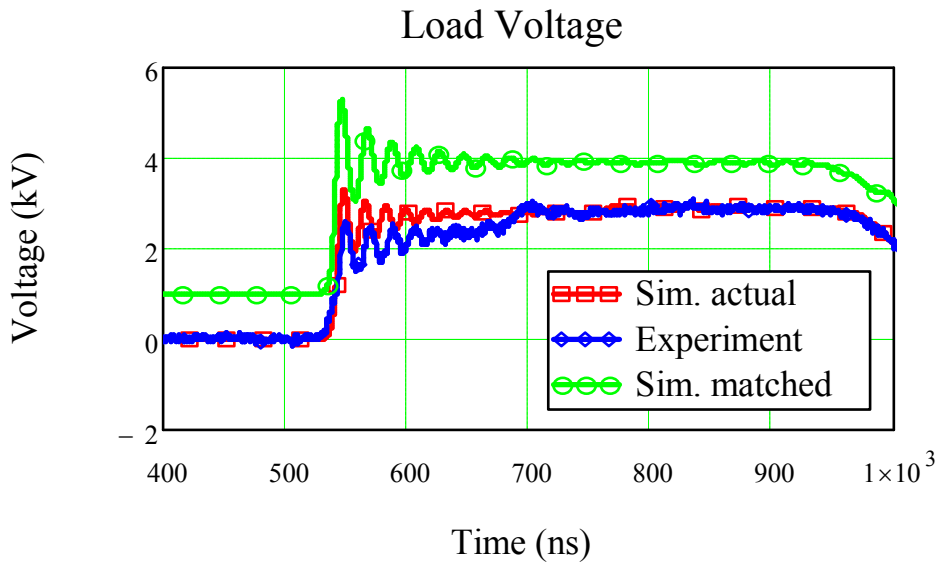

Figure 5.15 Load voltage vs. time for a 20-section NLHL. The simulated matched case is offset by +1 kV for clarity.

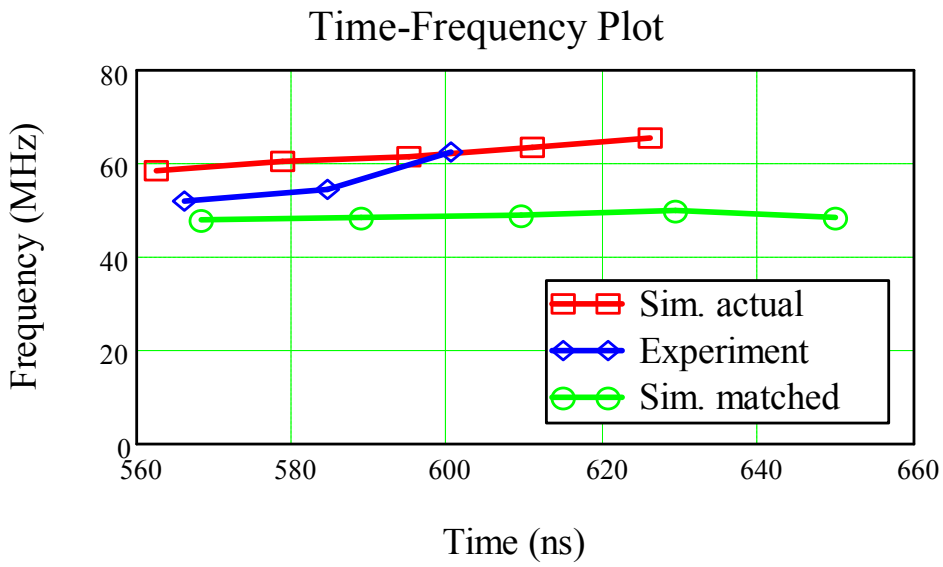

Figure 5.16 Voltage oscillation frequency vs. time for a 20-section NLHL.

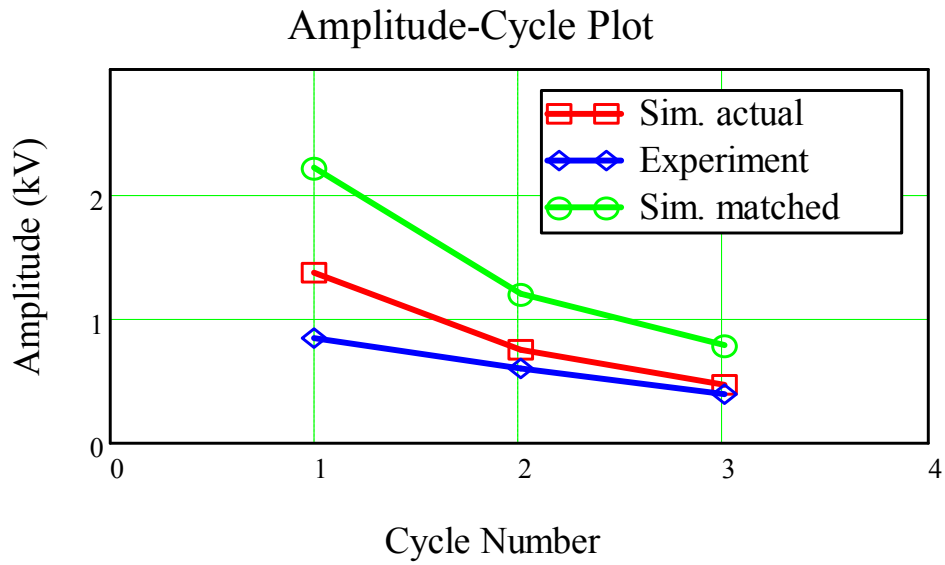

Figure 5.17 Peak-to-trough oscillation amplitude vs. oscillation cycle number for a 20-section NLHL.

The time-frequency plots for the simulation and experimental results are shown in Figure 5.16. The frequencies obtained for the simulated actual case and the experiment are around 60 MHz and 55 MHz, respectively. The simulated matched case has frequencies in the region of 50 MHz.

To see the quality of the load voltage modulation, the peak-to-trough oscillation amplitude V_{pt} is obtained for the first three cycles and is shown in the amplitude-cycle plot in Figure 5.17. The VMDs as defined in Section 3.2.2 for the simulated actual case and experiment are VMD_{Ld} = 859 V and VMD_{expt} = 615 V, respectively. The simulated matched case has VMD_{Lm} = 1398 V which is higher as expected due to the ideally matched conditions specified in Eqs.(5.1), (5.4), (5.5), (5.6) and (5.7).

The effects of the amplitude of the input pulse were also studied by varying the pulse generator voltage from 5 kV to 8 kV in steps of 1 kV. The measured load voltages are depicted in Figure 5.18. The time-frequency plot and amplitude-cycle plot are shown in Figure 5.19 and Figure 5.20, respectively. As the voltage increases from 5 kV to 8 kV, the oscillation frequencies increase from around 50 MHz to 70 MHz and the oscillation amplitudes also show considerable increases. Line reflections can be seen shortly after the oscillations diminish; for example, in the 8 kV line there is a step rise at around 650 ns.

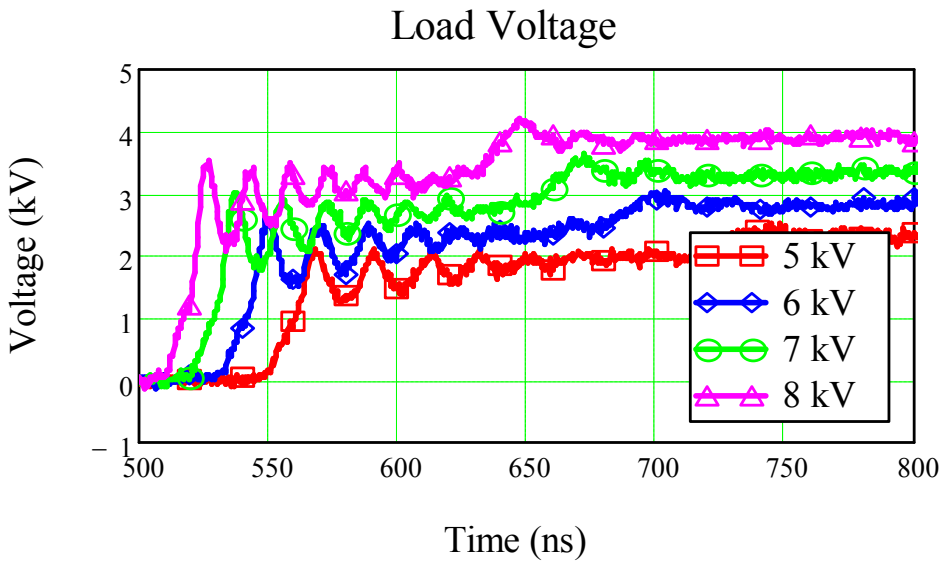

Figure 5.18 Experiment: Load voltage vs. time for a 20-section NLHL for different pulse generator voltages.

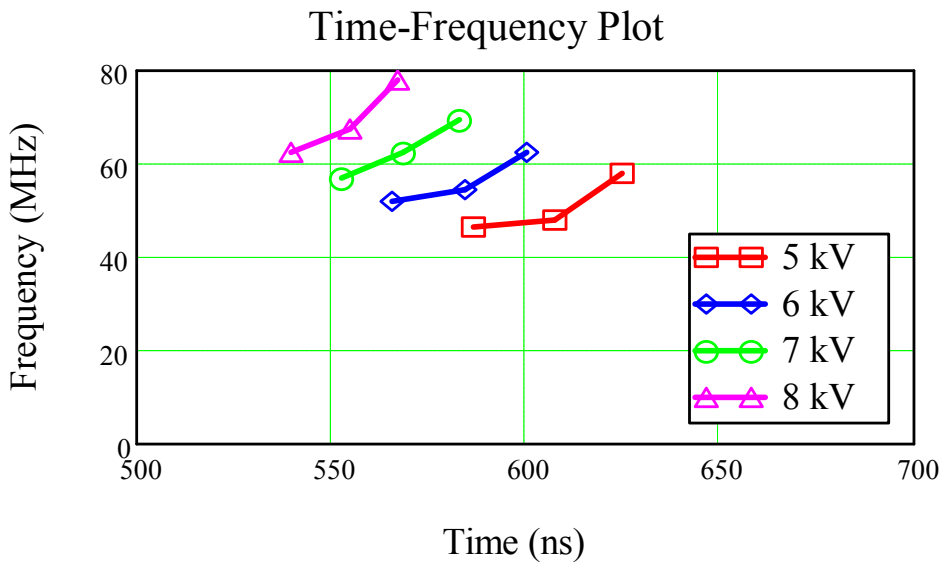

Figure 5.19 Experiment: Voltage oscillation frequency vs. time for a 20-section NLHL for different pulse generator voltages.

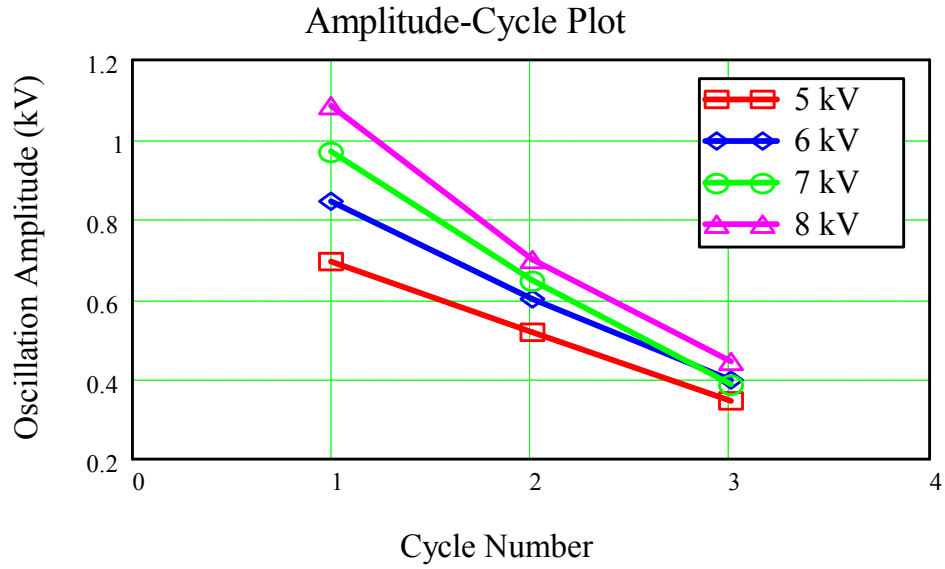

Figure 5.20 Experiment: Peak-to-trough oscillation amplitude vs. oscillation cycle number for a 20-section NLHL for different pulse generator voltages.

5.4 ANALYSIS

From the simulation and experimental results in Section 5.3, it is estimated that the nonlinear capacitors have equivalent series resistors (ESRs) of about 1-2 Ω. This ESR represents the dielectric loss in the capacitor which contains the polar material barium titanate. The main source of this loss is due to hysteresis as the polar material forms domains in the ferroelectric phase [7]. The applied field (via applying voltage across the capacitor) causes the movement of these domains which translates to energy loss. In an attempt to study how critical the ESR damps output oscillations, simulations using the NLETL model were carried out in this section.

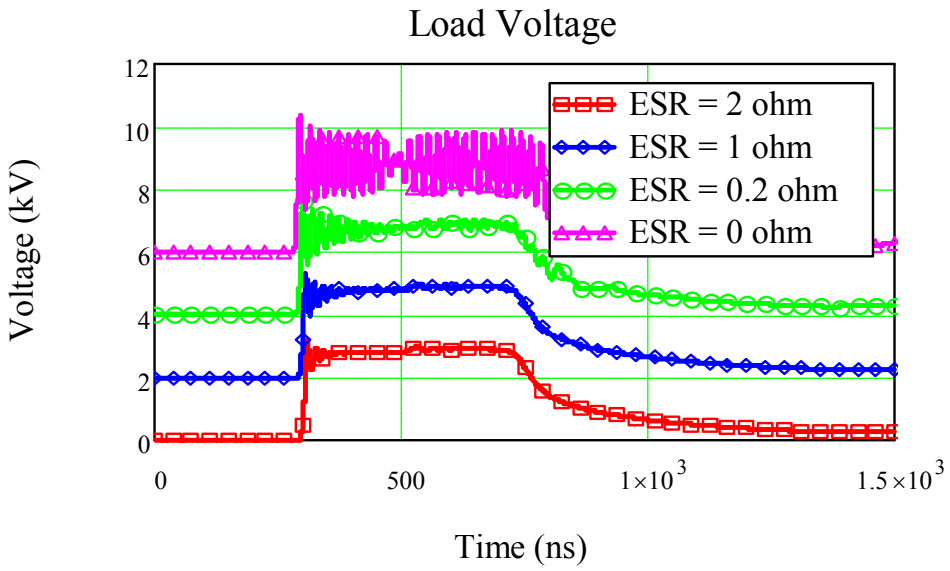

Figure 5.21 Simulation: Load voltage vs. time for a 20-section NLHL for different ESRs. Waveforms are offset by +2 kV from each other for clarity.

For a pulse of 6 kV with R_{gen} = 50 Ω and R_{load} = 50 Ω, a parameter sweep on ESR was simulated on a 20-section hybrid line using the actual L_d function for the nonlinear inductor as presented in Figure 5.13. The values of the ESRs were varied from 0 to 2 Ω in steps of 0.2 Ω. The case of ESR = 0 Ω corresponds to an ideal lossless

capacitor. To avoid cluttering, only four cases are plotted for the load voltage simulations shown in Figure 5.21. It is clear that increasing ESR will result in greatly reduced amplitudes of oscillations. The amplitude-cycle plot in Figure 5.22 indicates quantitatively the amount of oscillating voltage decrease for increasing ESR.

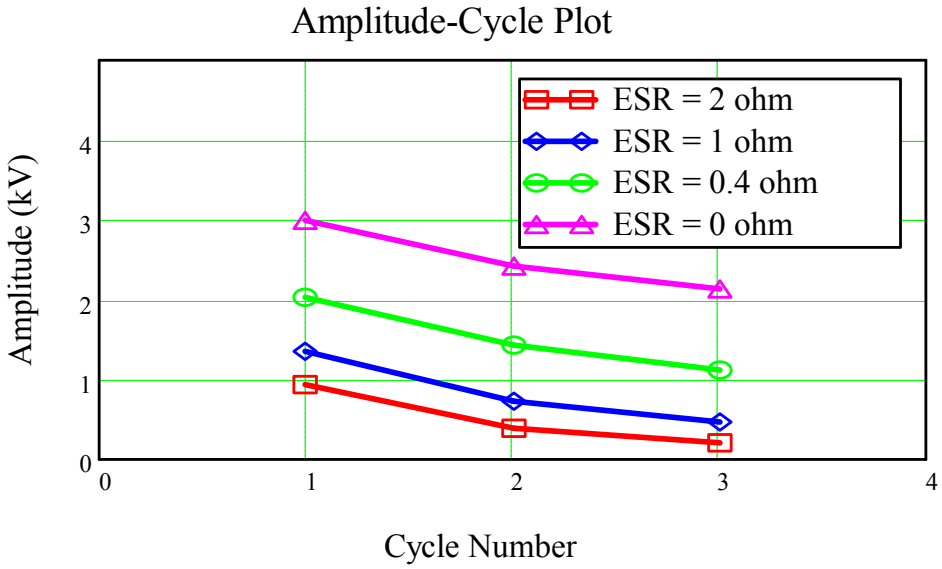

Figure 5.22 Simulation: Peak-to-trough oscillation amplitude vs. oscillation cycle number for a 20-section NLHL for different ESRs.

The time-frequency plot for the load voltages is depicted in Figure 5.23 and it is interesting to observe that the frequency of the oscillating cycles actually increases with increasing ESR. This can be explained by noting that as the ESR increases, the current flowing in the nonlinear capacitors will be diverted to flow even more in the nonlinear inductors. Hence, the inductors will further saturate to lower inductance value resulting in higher Bragg frequency. To view the relationship for power, the average peak load power P_{ave} as defined in Section 3.2.2 was plotted against the varying ESR values in Figure 5.24. The exponential decay in the power as ESR increases emphasizes the importance of the ESR parameter in damping the output oscillations. For comparison, simulation was also carried out for the case using the

matched L_m function (plotted in Figure 5.13) where the L-I curve is matched to the C-V curve according to the criteria in Eqs. (5.4) to (5.7). The P_{ave} for the case using the matched L_m function is also illustrated in Figure 5.24 and it shows greater average peak power than the case with actual L_d function. In particular, the case using L_m indicates at least twice the power of the case using L_d in the region of ESR = 0.4 to 2.0 Ω.

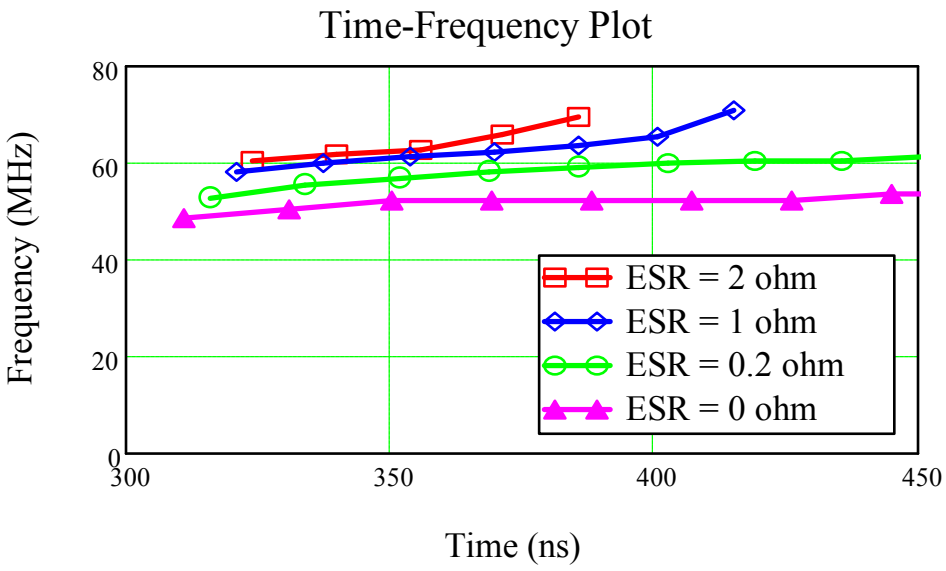

Figure 5.23 Simulation: Voltage oscillation frequency vs. time for a 20-section NLHL for different ESRs.

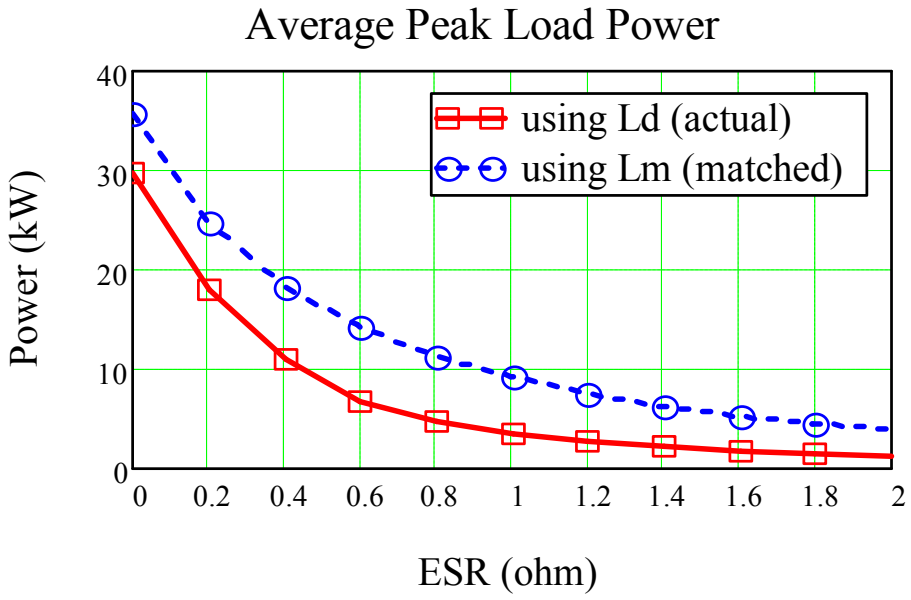

Figure 5.24 Simulation: Average peak load power vs. ESRs for a 20-section NLHL.

5.5 CONCLUSIONS

It has been demonstrated using COTS components that a simple pulse generator comprising a storage capacitor and a fast MOSFET semiconductor switch can be used to drive a NLHL to produce RF oscillations. Although a matched L-I curve to the C-V curve will in theory produce oscillation with good voltage modulation depth (VMD), it is shown in this article that an unmatched case is also capable of producing RF oscillations albeit with reduced VMD. The VMD in the unmatched case can be increased by increasing the amplitude of the input driving pulse which also at the same time increase the oscillation frequency. A detailed analysis was also carried out on the effect of the equivalent series resistor (ESR) of the nonlinear capacitor and it shows that the ESR is a critical parameter that damps the output oscillations. The ESR of the nonlinear capacitors used in the experiment is estimated to be about 1 to 2 Ω. Reducing the ESR by a factor of 2 or more (if better nonlinear capacitors with reduced dielectric losses are employed) will substantially improve the VMD. The average peak load power can be doubled if the L-I curve of the nonlinear inductor is matched to the C-V curve of the nonlinear capacitor.

CHAPTER 6: CONCLUSIONS

The research work undertaken in this thesis focuses on studying discrete lumped element transmission line (NLETL) for RF generation. In contribution to this field of work, a NLETL circuit model was developed to address the inadequacies of the current model in the open literature. This model was validated with experiments at low voltage before being applied in designing high voltage lines. Extensive and comprehensive parametric study using the NLETL model was carried out to fully understand how each parameter of the pulse and line will affect the output waveform. Consequently, the model was used in designing the three types of high voltage NLETL: namely, nonlinear capacitive line (NLCL), nonlinear inductive line (NLIL) and nonlinear hybrid line (NLHL). Other contributions include an innovative method for more efficient RF extraction in NLCL and a simple novel method for obtaining the necessary material parameters for modeling the NLIL. Last but not least, the NLHL (where no experimental NLHL has been reported to date) was successfully demonstrated in experiment.

In the area of NLCL, an innovative method of RF extraction was proposed and implemented. The proposed method gives higher power efficiency and better voltage modulation depth of the output waveform as compared to a convention NLCL. In addition, this method does not require a high-pass filter to remove the DC from the

AC component which are both present in the standard line. This direct extraction method improves efficiency and makes the line more compact.

In an effort to model the NLIL, a simple procedure was developed to obtain the characteristic L-I curve of the nonlinear inductor. A curve-fit function for the L-I curve was then acquired for use in the NLETL model. It can also be applied in commercial PSpice software. Additionally, for better accuracy, a simplified form of the Landau-Lifshitz-Gilbert (LLG) equation was utilized in the NLETL model to better represent the dynamics of the magnetization in the inductor. A novel approach was thus created to find the critical parameters in the LLG equation.

For NLHL, it was shown through the NLETL simulation that if the C-V curve of the nonlinear capacitor and L-I curve of the nonlinear inductor follows a certain impedance design equations to keep the characteristic of the line constant, output pulse at the matched load with better voltage modulation depth and higher operating frequency can be achieved (compared to NLC and NLIL). However, it was difficult to get the C-V and L-I curves to match each other in practice. Nonetheless, it was demonstrated in experiments that the NLHL could still produce oscillatory waveforms without the C-V and L-I curves matching each other. It was observed that if the characteristic impedance of the line at saturation of both nonlinear components is close to the load value, pulse oscillations can be realized. The experimental demonstration of the NLHL is the first of its kind as only simulation work has been reported to date.

On the whole, the simulations results from the NLETL model show good match to the experiment data obtained from the NLCL, NLIL and NLHL. On future work, a possible extension to the model is to make the equivalent series resistor (ESR) for the nonlinear capacitors (which is assumed constant currently) frequency dependent. As this ESR affects the damping of the output oscillation, a model with a

frequency dependent ESR will probably yield better accuracy at higher operating frequency. Parametric study on the performance of the line as the ratio of *L* to *C* varies can also be explored using the model. Maximizing the ratio of *L* to *C* will be useful when a line with certain specifications needs to be designed. In addition, this NLETL model can be further applied to multiple cascading lines in parallel to investigate the combined effect of multiple lines. The NLETL model can also be extended to explore parametric amplification on NLETLs. This technique was proposed by A. B. Kozyrev [94] whereby a sinusoidal pulse and a rectangular pulse are injected simultaneously into the input of a NLETL and a RF pulse with higher power and increased frequency will be generated at the output. Besides using the NLETL model for RF generation, it can also be used for simulating pulse sharpening for nonlinear *L* and *C*; and simulating delay of input pulse for linear *L* and *C*. On the experimental aspect, part of future work can also include investigating the best type of antenna for NLETL to radiate RF pulses. It will also be interesting to synchronize multiple NLETLs to radiate and sum the RF power in space.

The result of having studied the three types of NLETL suggests that there is a need for custom-made capacitors (linear or nonlinear) with low ESR. The ESR is a critical parameter that affects the modulation depth of the output RF pulse and a low ESR value will greatly improve oscillation amplitudes leading to higher power efficiency. The prospect of using of NLHL for better performance also advocates the requirement to develop techniques to make dielectric materials and magnetic materials to conform to certain desired C-V curve and L-I curve, respectively. In other words, this heralds the need to produce materials with C-V and L-I curves that meet the impedance design equations so as to keep the characteristic impedance of the line constant in a nonlinear environment.

BIBLIOGRAPHY

[1] I.G. Kataev, *Electromagnetic Shock Waves*. London: Illife, 1966.

[2] N.J. Zabusky and M.D. Kruskal, "Interaction of "Solitons" in a collisionless plasma and the recurrence of initial states," *Phys. Rev. Lett.*, 15, pp. 240-243 (1965).

[3] B.A.P. Taylor, "What is a solitary wave?" *Am. J. Phys.*, vol. 47, pp. 847 (1979).

[4] K.E. Lonnegren and A. Scott (ed), *Solitons in Action*. New York: Academic Press, pp. 127-152, 1978.

[5] H. Ikezi, S.S. Wojtowicz, R.E. Waltz, J.S. deGrassie, and D.R. Baker, "High power soliton generation at microwave frequencies," *J. Appl. Phys.*, vol. 64, pp. 3277-3281 (1988).

[6] T. Kuusela and J. Hietarinta, "Nonlinear electrical transmission line as a burst generator," *Rev. Sci. Instrum.*, vol. 62, pp. 2266-2270 (1991).

[7] M.P. Brown and P.W. Smith, "High power, pulsed soliton generation at radio and microwave frequencies," *Proc. Of 11th IEEE Int. Pulsed Power Conf.* (Baltimore, MD, 1997), pp. 346-354.

[8] J. Gaudet, E. Schamiloglu, J.O. Rossi, C. J. Buchenauer, and C. Frost, "Nonlinear transmission lines for high power microwave applications – A survey," *Proc. of 28th IEEE Int. Power Modulator Symposium and 2008 High Voltage Workshop* (Las Vegas, NV, 2008), pp. 131-138.

[9] Victor L. Granatstein and Igor Alexeff, *High-Power Microwave Sources*. Artech House, 1987.

[10] R.J. Barker and E. Schamiloglu (ed), *High Power Microwave Sources and Technologies*. New York: IEEE Press/J. Wiley & Sons, 2001.

[11] J. Benford, John A. Swegle and E. Schamiloglu, *High Power Microwaves*. 2nd ed. Taylor & Francis, 2007.

[12] H. Nagashima and Y. Amagishi, "Experiment on the Toda lattice using nonlinear transmission lines," *J. Phys. Soc. Japan*, vol. 45, pp. 690-688 (1978).

[13] T. Kuusela, J. Hietarinta, K. Kokko, and R. Laiho, "Soliton experiments in a nonlinear electrical transmission line," *Eur. J. Phys.*, vol. 8, pp. 27-33 (1987).

[14] T. Tsuboi, "Phase shift in the collision of two solitons propagating in a nonlinear transmission line," *Phys. Rev. A*, vol. 40, pp. 2753-2755 (1989).

[15] S. Ibuka, M. Ohnishi, T. Yamada, K. Yasuoka and S. Ishii, "Voltage amplification effect of nonlinear transmission lines for fast high voltage pulse generation," *Proc. 11th IEEE Int. Pulsed Power Conf.* (Baltimore, MD, 1997), pp. 1548-1553.

[16] T. Tsuboi, "Formation process of solitons in a nonlinear transmission line: experimental study," *Phys. Rev. A*, vol. 41, pp. 4534-4537 (1990).

[17] M. Weiner, S. Schneider, and F. Dollak, "Lumped circuit ferrite pulse sharpener," *Proc. of 4th IEEE Int. Pulsed Power Conf.* (Albuquerque, NM, 1983), pp.150-154.

[18] C.R. Wilson, M.M. Turner, and P.W. Smith, "Pulse sharpening in a uniform LC ladder network containing nonlinear ferroelectric capacitors," *IEEE Trans. Electron Dev.*, vol. 38, pp. 767-771 (1991).

[19] M.M. Turner, G. Branch, and P. Smith, "Methods of theoretical analysis and computer modeling of the shaping of electrical pulses by nonlinear transmission lines and lumped-element delay lines," *IEEE Trans. Electron Dev.,* vol. 38, pp. 810-816 (1991).

[20] S. Ibuka, K. Abe, T. Miyazawa, A. Ishii, and S. Ishii, "Fast high-voltage pulse generator with nonlinear transmission line for high repetitive rate operation," *IEEE Trans. Plasma Sci.*, vol. 25, pp. 266-271 (1997).

[21] E. Afshari and A. Hajimiri, "Nonlinear transmission lines for pulse shaping in silicon," *Solid-State Circuits, IEEE Journal of*, vol.40, no.3, pp. 744-752, March 2005.

[22] E. Afshari, H.S. Bhat, A. Hajimiri & J. E. Marsden, "Extremely wideband signal shaping using one and two dimensional nonuniform nonlinear transmission lines," *J. Appl. Phys.*, 99, 054901 (2006).

[23] H. Ikezi, "Compression of a single electromagnetic pulse in a spatially modulated N dielectric," *J. Appl. Phys.*, vol. 64, pp. 3273-3276 (1988).

[24] H. Ikezi, Y.R. Lin-Liu, T. Ohkawa and J.S. deGrassie, "Electrostrictions in high-power soliton generator," *J. Appl. Phys.*, vol. 64, pp. 4717-4719 (1988).

[25] H. Ikezi, S.S. Wojtowicz, R.E. Waltz and D.R. Baker, "Temporal contraction of solitons in a nonuniform transmission line," *J. Appl. Phys.*, vol. 64, pp. 6836-6838 (1988).

[26] T. Kuusela and J. Hietarinta, "Numerical, experimental, and analytical studies of the dissipative toda lattice: I. The behavior of a single solitary wave," Physica D: Nonlinear Phenomena, Volume 41, Issue 3, April 1990, pp. 322-340.

[27] T. Kuusela and J. Hietarinta, "Numerical, experimental, and analytical studies of the dissipative toda lattice II. Elastic scattering of solitary waves," Physica D: Nonlinear Phenomena, Volume 46, Issue 1, October 1990, pp. 1-9.

[28] T. Kuusela, "Soliton experiments in a damped ac-driven nonlinear electrical transmission line," Physics Letters A, Volume 167, Issue 1, 6 July 1992, pp. 54-59.

[29] T. Kuusela, "AC-driven damped Toda lattice," Computers & Mathematics with Applications, Volume 28, Issues 10-12, November-December 1994, pp. 327-351.

[30] T. Kuusela, "Soliton experiments in transmission lines," Chaos, Solitons & Fractals, Volume 5, Issue 12, December 1995, pp. 2419-2462.

[31] H. Ikezi, J.S. deGrassie and J. Drake, "Soliton generation at 10 MW level in the very high frequency band," *Appl. Phys. Lett.*, 58, pp. 986-987 (1991).

[32] J.D. Darling and P.W. Smith, "High power RF generation from non-linear delay lines," *Proc. of 16th IEEE Int. Pulsed Power Conf.* (Albuquerque, NM, 2007), pp.472-475.

[33] J.D. Darling and P.W. Smith, "High power RF generation and delivery from nonlinear lumped element transmission lines," *Proc. of 2nd Euro-Asian Pulsed Power Conf.* (Vilnius, Lithuania, 2008).

[34] W.S. Melville, "The use of saturable inductors as discharge devices for pulse generators," *Proc. IEE*, 98, pp. 185-207, 1951.

[35] P.R. Johannessen, "High-power step recovery diodes and saturable inductors in radar pulse modulators," *IEEE Transactions on Magnetics*, vol.3, no.3, pp. 256-260, Sep 1967.

[36] A.M. Belyantsev and S.L. Klimin, "High-frequency generation by electromagnetic shock wave in transmission line with nonlinear capacitance," *Radiophysics and Quantum Electronics*, vol. 36, no. 11, pp. 769-778 (1993).

[37] A.M. Belyantsev and A.B. Kozyrev, "Generation of high-frequency oscillations by electromagnetic shock wave on transmission lines on the basis of multilayer heterostructures," *International Journal of Infrared and Millimeter Waves*, vol. 18, no. 6, pp. 1169-1186 (1997).

[38] A.M. Belyantsev, A.I. Dubnev, S.L. Klimin, Yu. A. Kobelev and L.A. Ostrovskii, "Generation of radio pulses by an electromagnetic shock wave in a ferrite loaded transmission line," *Tech. Phys.*, vol 40 (8), pp. 820-826 (1995).

[39] A.M. Belyantsev and A.B. Kozyrev, "Influence of local dispersion on transient processes accompanying the generation of RF radiation by an electromagnetic shock wave," *Tech. Phys.*, vol. 43 (1), pp. 80-85 (1998).

[40] A.M. Belyantsev and A.B. Kozyrev, "Generation of RF oscillations in the interaction of an electromagnetic shock wave with a synchronous backward wave," *Tech. Phys.*, vol. 45 (6), pp. 747-752 (2000).

[41] J.D.C. Darling and P.W. Smith, "High power pulse burst generation by soliton-type oscillation on nonlinear lumped element transmission lines," *Proc. of 17th IEEE Int. Pulsed Power Conf.* (Washington, DC, 2009), pp. 119-123.

[42] N. Seddon, C.R. Spikings, and J.E. Dolan, "RF pulse formation in nonlinear transmission lines," *Proc. of 16th IEEE Int. Pulsed Power Conf.,* (Albuquerque, NM, 2007), pp. 678-681.

[43] J.O. Rossi and P.N. Rizzo, "Study of hybrid nonlinear transmission lines for high power RF generation," *Proc. of 17th IEEE Int. Pulsed Power Conf.* (Washington, DC, 2009), pp. 46-50.

[44] J.O. Rossi, P.N. Rizzo & F.S. Yamasaki, "Prospects for applications of hybrid lines in RF generation," *Proc. of 2010 IEEE Int. Power Modulator and High Voltage Conf.* (Atlanta, GA, 2010), pp. 632-635.

[45] M. Weiner, "Pulse sharpening in ferrite transmission lines," *Proc. of 2nd IEEE Int. Pulsed Power Conf.* (Lubbock, TX, 1979), pp. 91-95.

[46] M. Weiner, S. Schneider, and F. Dollak, "Lumped circuit ferrite pulse sharpener," *Proc. of 4th IEEE Int. Pulsed Power Conf.* (Albuquerque, NM, 1983), pp.150-154.

[47] R. Pouladian-Kari, T.M. Benson, A.J. Shapland and D.M. Parkes, "The electrical simulation of pulse sharpening by dynamic lines," *Proc. of 7th IEEE Int. Pulsed Power Conf.* (Montery, CA, 1989), pp.178-181.

[48] W. Sullivan III, J. Dickens and M. Kristiansen, "Shock wave simulation of ferrite-filled coaxial nonlinear transmission lines," *Proc. of 28th IEEE Int. Power Modulator Symposium and 2008 High Voltage Workshop* (Las Vegas, NV, 2008), pp. 517-520.

[49] J.E. Dolan, "Simulation of ferrite-loaded coaxial lines," *Electronics Letters*, vol.29, no.9, pp.762,763, 1993.

[50] J.E. Dolan, H.R. Bolton and A.J. Shapland, "Analysis of ferrite line pulse sharpeners", *Proc. of 9th IEEE Int. Pulsed Power Conf.* (Albuquerque, NM, 1993), pp. 308-311.

[51] J.E. Dolan, H.R. Bolton, A.J. Shapland, "Development of ferrite line pulse sharpeners," *Proc. of 9th IEEE Int. Pulsed Power Conf.* (Albuquerque, NM, 1993), pp. 795-798.

[52] J.E. Dolan, "Simulation of shock waves in ferrite-loaded coaxial transmission lines with axial bias," *Journal of Physics D: Applied Physics*, 1999, vol. 32, pp. 1826.

[53] V.P. Gubanov, A.V. Gunin. O.B. Koval'chuk, V.O. Kutenkov, I.V. Romanchenko and V.V. Rostov, "Effective transformation of the energy of high-voltage pulses into high-frequency oscillations using a saturated-ferrite-loaded transmission line", *Technical Physics Letters*, Vol. 35, No. 7, pp. 626-628. 2009.

[54] I.V. Romanchenko and V.V. Rostov, "Frequency of high power RF-generation in nonlinear transmission lines with saturated ferrite", *Proc. of 2010 IEEE Int. Power Modulator and High Voltage Conf.* (Atlanta, GA, 2010), pp. 521-524.

[55] I.V. Romanchenko and V.V. Rostov, "Energy levels of oscillations in a nonlinear transmission line filled with saturated ferrite", *Technical Physics*, Vol. 55, No. 7, pp. 1024-1027. 2010.

[56] Vladislav V. Rostov, Nikolai M. Bykov, Dmitry N. Bykov, Alexei I. Klimov, Oleg B. Kovalchuk and Ilya V. Romanchenko, "Generation of Subgigawatt RF Pulses in Nonlinear Transmission Lines," *IEEE Trans. on Plasma Sci.*, vol. 38, no. 10, pp. 2681-2685. 2010.

[57] J. Bragg, J. Dickens and A. Neuber, "Magnetic biasing of ferrite filled nonlinear transmission lines", *Proc. of 2010 IEEE Int. Power Modulator and High Voltage Conf.* (Atlanta, GA, 2010), pp. 600-603.

[58] J. Bragg, J. Dickens and A. Neuber, "Temperature dependence of ferrimagnetic based nonlinear transmission line," *Proc. of 18th IEEE Int. Pulsed Power Conf.* (Chicago, IL, 2011), pp. 182-184.

[59] S.J.F. Chadwick, N. Seddon and S. Rukin, "A novel solid-state HPM source based on a gyromagnetic NLTL and SOS-based pulse generator," *Proc. of 18th IEEE Int. Pulsed Power Conf.* (Chicago, IL, 2011), pp. 178-181.

[60] D.S. Ricketts, X. Li and D. Ham, "Electrical soliton oscillator," *IEEE Trans. Microw. Theory. Tech.*, vol. 54, no. 1, pp. 373–382, Jan. 2006.

[61] B.I. Bleaney and B. Bleaney, *Electricity and Magnetism.* 3rd ed. Oxford, U.K.: Oxford Univ. Press, 1976.

[62] P.W. Smith, *Transient Electronics – Pulsed Circuit Technology.* West Sussex, England: John Wiley & Sons, 2002.

[63] Q.R. Marksteiner, B.E. Carlsten and S. Russell, "Numerical calculations of RF efficiency from a soliton generating nonlinear transmission line," J. Appl. Phys., vol. 106 (11), pp. 113306, 2009.

[64] Q.R. Marksteiner, B.E. Carlsten and S. Russell, "Efficient generation of RF using a biased soliton generating nonlinear transmission line with a bipolar input," Micro. Opt. Techn. Let., vol. 52 (6), pp. 1411, 2010.

[65] S. Giambo, P. Pantano, and P. Tucci, "An electrical model for the Korteweg-de Vries equation," *Am. J. Phys.,* vol. 52, 238-243 (1984).

[66] E. Sawado, M. Taki, and S. Kiliu, "Nonlinear magnetic lattice and the modified Korteweg-de Vries equation," *Phys. Rev. B*, vol. 38, 11911-11914 (1988).

[67] M. Toda, "Wave propagation in anharmonic lattices," *J. Phys. Soc. Japan*, vol. 23, 501-506 (1967).

[68] T. Taniuti and C-C. Wei, "Reduction perturbation method in nonlinear waves propagation. I," *J. Phys. Soc. Japan*, vol. 24, 941-946 (1968).

[69] M. Toda and M. Wadati, "A soliton and two solitons in an exponential lattice and related equations," *J. Phys. Soc. Japan*, vol. 34, 18-25 (1973).

[70] T. Yagi, H. Watanabe and A. Noguchi, "Growth and damping of solitons in a nonlinear trasmission line with moving parameters," *Proc. of IEEE*, vol. 66, no.6, pp. 702-703, 1978.

[71] H. Ikezi, "Compression of a single electromagnetic pulse in a spatially modulated nonlienar dielectric," *J. Appl. Phys.*, vol. 64, pp. 3273-3276 (1988).

[72] L. Fortuna, M. Frasca and A. Rizzo, "Generating solitons in lattices of nonlinear circuits," *2001 IEEE International Symposium on Circuits and Systems*, vol.3, pp. 680-683, 2001.

[73] P. G. Drazin and R. S. Johnson, *Solitons: An Introduction*. 2nd ed. Cambridge, U.K.: Cambridge Univ. Press, 1989.

[74] R. Hirota (ed), *The Direct Method in Soliton Theory.* Cambridge, U.K.: Cambridge Univ. Press, 2004.

[75] R. Hirota, "Exact solution of the Korteweg-de Vries equation for multiple collisions of solitons," *Phys. Rev. Letters*, vol. 27, n. 18, pp. 1192-1194, 1971.

[76] P.J. Hansen and D.R. Nicholson, "Simple soliton solutions," *Am. J. Phys.*, vol. 47, pp. 769 (1979).

[77] W. Malfliet, "Simple solution method for the Korteweg-de Vries equation," *Am. J. Phys.*, vol. 49, pp. 666 (1981).

[78] A-M. M. Abdel-Rahman, "Simple multisoliton solutions," *Am. J. Phys.*, vol. 51, pp. 510 (1983).

[79] M. M. Turner, G. Branch, and P. Smith, "Methods of theoretical analysis and computer modeling of the shaping of electrical pulses by nonlinear transmission lines and lumped-element delay lines," *IEEE Trans. Electron Dev.,* vol. 38, pp. 810-816 (1991).

[80] J.D.C. Darling and P.W. Smith, "High-power pulsed RF extraction from nonlinear lumped element transmission lines," *IEEE Trans. Plasma Sci.,* vol. 36, 2598-2603 (2008).

[81] P.W. Smith, "Pulsed, high power, RF generation from nonlinear dielectric ladder networks – performance limits," *Proc. of 18th IEEE Int. Pulsed Power Conf.* (Chicago, IL, 2011), pp. 167-172.

[82] J.M. Sanders, Y.H. Lin, R. Ness, A. Kuthi and M. Gundersen, "Pulse sharpening and soliton generation with nonlinear transmission lines for producing RF bursts", *IEEE Int'l. Power Modulator and High Voltage Conf.,* Atlanta, GA, USA, pp. 632-635, 2010.

[83] C.K. Campbell, J.D. van Wyk, M.F.K. Holm, J.J.R. Prinsloo and J.J. Schoeman, "Relaxation effects in high-voltage barium titanate nonlinear ceramic disk capacitors", *IEEE Transactions on Components, Hybrid and Manufacturing Technology*, vol. 16, no. 4, pp. 418-423 (1993).

[84] D.M. French, B.D Hoff, S. Heidger and D. Schiffler, "Dielectric nonlinear transmission line," *Proc. of 18th IEEE Int. Pulsed Power Conf.* (Chicago, IL, 2011), pp. 341-345.

[85] D.M. French, Y.Y. Lau and R.M. Gilgenbach, "High power nonlinear transmission lines with nonlinear inductance," *Proc. of 2010 IEEE Int. Power Modulator and High Voltage Conf.* (Atlanta, GA, 2010), pp. 598-599.

[86] P.D. Coleman, J.J. Borchardt, J.A. Alexander, J.T. Williams and T.F. Peters, "Characterization of a synchronous wave nonlinear transmission line," *Proc. of 18th IEEE Int. Pulsed Power Conf.* (Chicago, IL, 2011), pp. 173-177.

[87] T.L. Gilbert, "A phenomenological theory of damping in ferromagnetic materials,"*IEEE Transactions on Magnetics*, vol.40, no.6, pp.3443-3449, 2004.

[88] J. Stohr and H.C. Siegmann, *Magnetism: From fundamentals to nanoscale dynamics*. Springer-Verlag, 2006, pp. 61-103.

[89] R. Burdt and R.D. Curry, "Magnetic core test stand for energy loss and permeability measurements at high constant magnetization rate and test results for nanocrystalline and ferrite materials," *Rev. Sci. Instrum.*, vol. 79, 094703 (2008).

[90] A.V. Bossche and V.C. Valchev, *Inductors and transformers for power electronics*. Taylor & Francis, 2005, pp. 1-29.

[91] W.H. Wolfle and W.G. Hurley, "Quasi-active power factor correction with a variable inductive filter: theory, design and practice," *IEEE Transactions on Power Electronics*, vol.18, no.1, pp. 248- 255, Jan 2003.

[92] R. Kikuchi, "On the minimum of magnetization reversal time," *J. Appl. Phys.*, vol. 27, pp. 1352-1357 (1956).

[93] E.M. Gyorgy, "Rotational model of flux reversal in square loop ferrites," *J. Appl. Phys.*, vol. 28, pp. 1011-1015 (1957).

[94] A.B. Kozyrev and D.W. van der Weide, "Parametric amplification and frequency up-conversion of high power RF pulses in nonlinear transmission lines," *Proc. of 18th IEEE Int. Pulsed Power Conf.* (Chicago, IL, 2011), pp. 156-161.

[95] M. Remoissenet, *Waves called solitons: concepts and experiments*. 3rd ed. Springer-Verlag, 1999.

[96] F. Fallside and D.T. Bickley, "Nonlinear delay line with a constant characteristic impedance," *Proc. IEE*, vol. 113, 263-270 (1966).

[97] O.S.F. Zucker and W.H. Bostick, "Theoretical and practical aspects of energy storage and compression", in *Energy Storage, Compression and Switching* edited by W.H. Bostick, V. Nardi and O.S.F. Zucker. New York: Plenum Publishing Corp., 1976, pp. 71-93.

APPENDIX A: DERIVATION OF KDV EQUATION FOR A LC LADDER CIRCUIT

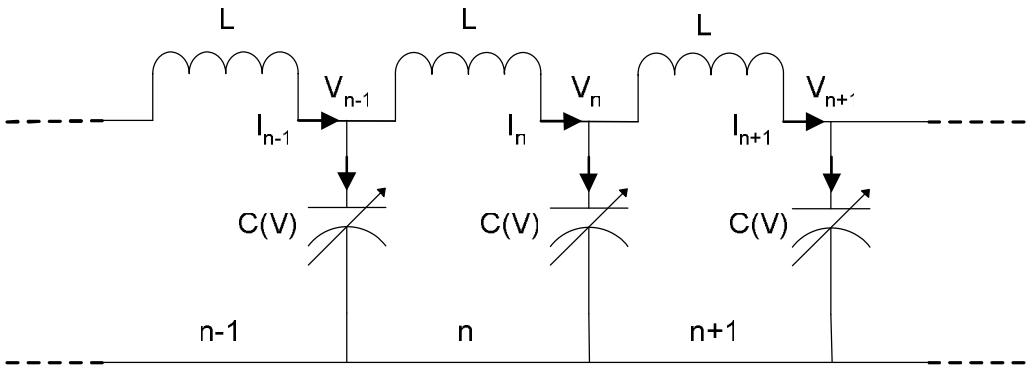

Figure A.1 Circuit diagram of NLCL.

This appendix illustrates the derivation of the Korteweg-de Vries (KdV) equation from a nonlinear capacitive line (NLCL) where the inductive components are linear and the capacitive components are nonlinear.

By applying Kirchoff's law to the circuit in Figure A.1 and assuming the NLCL is lossless, the difference-differential equations are:

$$L\frac{\partial I_n}{\partial t} = V_n - V_{n-1}, \tag{A.1}$$

$$L\frac{\partial I_{n+1}}{\partial t} = V_{n+1} - V_n, \tag{A.2}$$

$$\frac{\partial Q_n}{\partial t} = I_{n+1} - I_n. \tag{A.3}$$

The charge on the capacitor with bias voltage V_0 is given by

$$Q_n(t) = \int_0^{V_0} C(V)\,dV + \int_0^{V_0+V_n} C(V)\,dV \quad . \tag{A.4}$$

Assuming the nonlinear capacitors have the following capacitance function:

$$C(V) = \frac{Q(V)}{F(V_0) - V_0 + V} \quad . \tag{A.5}$$

Sub. Eq.(A.5) into Eq.(A.4),

$$\begin{aligned} Q_n(t) &= Q(V_0)\left[\ln\left(\frac{F(V_0)}{F(V_0)-V_0}\right)\right] + Q(V_0)\left[\ln\left(\frac{F(V_0)+V_n}{F(V_0)}\right)\right] \\ &\text{where } Q(V_0)\left[\ln\left(\frac{F(V_0)}{F(V_0)-V_0}\right)\right] \text{ is a constant.} \end{aligned} \tag{A.6}$$

Differentiating Eq.(A.6) twice w.r.t. t gives

$$\frac{\partial^2 Q_n(t)}{\partial t^2} = \frac{\partial^2}{\partial t^2}\left\{Q(V_0)\left[\ln\left(1+\frac{V_n}{F(V_0)}\right)\right]\right\} \quad . \tag{A.7}$$

Differentiating Eq.(A.3) w.r.t. t gives

$$\frac{\partial^2 Q_n}{\partial t^2} = \frac{\partial I_{n+1}}{\partial t} - \frac{\partial I_n}{\partial t} \quad . \tag{A.8}$$

Sub. Eq.(A.1), Eq.(A.2) and Eq.(A.7) into Eq.(A.8),

$$\begin{aligned} &\frac{\partial^2}{\partial t^2}\left\{Q(V_0)\left[\ln\left(1+\frac{V_n}{F(V_0)}\right)\right]\right\} = \frac{V_{n+1}-V_n}{L} - \frac{V_n - V_{n-1}}{L} \\ &\Rightarrow L\frac{\partial^2}{\partial t^2}\left\{Q(V_0)\left[\ln\left(1+\frac{V_n}{F(V_0)}\right)\right]\right\} = V_{n+1} + V_{n-1} - 2V_n \quad . \end{aligned} \tag{A.9}$$

Assume $(V_n)_{max} << F(V_0)$, using the series expansion

$$\ln(1+x) = x - \frac{x^2}{2} + \frac{x^3}{3} - \frac{x^4}{4} + \cdots \tag{A.10}$$

and using Eq.(A.5), $Q(V_0)\ln\left(1+\frac{V_n}{F(V_0)}\right)$ in Eq.(A.9) becomes

$$\begin{aligned} Q(V_0)\ln\left(1+\frac{V_n}{F(V_0)}\right) &= Q(V_0)\left\{\frac{V_n}{F(V_0)}-\frac{1}{2}\left[\frac{V_n}{F(V_0)}\right]^2+\cdots\right\} \\ &\approx \frac{Q(V_0)}{F(V_0)}\left\{V_n-\frac{V_n^{\,2}}{2F(V_0)}\right\} = C(V_0)\left\{V_n-\frac{V_n^{\,2}}{2F(V_0)}\right\} \end{aligned} \quad \text{(A.11)}$$

Let *n* be a continuous variable such that

$$V_n \Leftrightarrow V(n) = V \quad \text{(A.12)}$$

Making use of Taylor series $f(x)=\sum_{k=0}^{\infty}\frac{f^{(k)}(a)}{k!}(x-a)^k$, expand V_{n+1} and V_{n-1} as follows:

$$V_{n+1} \Leftrightarrow V(n+1) = V+\frac{\partial V}{\partial n}+\frac{1}{2}\frac{\partial^2 V}{\partial n^2}+\frac{1}{6}\frac{\partial^3 V}{\partial n^3}+\frac{1}{24}\frac{\partial^4 V}{\partial n^4}+\cdots \quad \text{(A.13)}$$

$$V_{n-1} \Leftrightarrow V(n-1) = V-\frac{\partial V}{\partial n}+\frac{1}{2}\frac{\partial^2 V}{\partial n^2}-\frac{1}{6}\frac{\partial^3 V}{\partial n^3}+\frac{1}{24}\frac{\partial^4 V}{\partial n^4}+\cdots \quad \text{(A.14)}$$

Sub. Eq.(A.11), (A.12), (A.13) and (A.14) into Eq.(A.9),

$$LC(V_0)\frac{\partial^2}{\partial t^2}\left\{V-\frac{V^2}{2F(V_0)}\right\} = \frac{\partial^2 V}{\partial n^2}+\frac{1}{12}\frac{\partial^4 V}{\partial n^4} \quad \text{(A.15)}$$

Putting $v_0=\frac{1}{\sqrt{LC(V_0)}}$, Eq.(A.15) becomes

$$\frac{\partial^2}{\partial t^2}\left\{V-\frac{V^2}{2F(V_0)}\right\} = v_0^{\,2}\left[\frac{\partial^2 V}{\partial n^2}+\frac{1}{12}\frac{\partial^4 V}{\partial n^4}\right] \quad \text{(A.16)}$$

Using Gardner –Morikawa transformation:

$$x = \varepsilon^{\frac{1}{2}}(n-v_0 t), \quad \text{(A.17)}$$

$$\tau = \varepsilon^{\frac{3}{2}}\frac{v_0}{24}t, \quad \text{(A.18)}$$

$$V = -\frac{\varepsilon F u}{2}, \quad \text{(A.19)}$$

$$\text{where } u = u(x,\tau) \tag{A.20}$$

For an arbitrary function $y = y(x,\tau)$, its derivative w.r.t. *t* gives

$$\frac{\partial y}{\partial t} = \frac{\partial y}{\partial x}\cdot\frac{\partial x}{\partial t} + \frac{\partial y}{\partial \tau}\cdot\frac{\partial \tau}{\partial t} = -\varepsilon^{\frac{1}{2}}v_0\frac{\partial y}{\partial x} + \frac{\varepsilon^{\frac{3}{2}}v_0}{24}\frac{\partial y}{\partial \tau} \tag{A.21}$$

Differentiating Eq.(A.21) w.r.t. *t* gives

$$\begin{aligned}\frac{\partial^2 y}{\partial t^2} &= \frac{\partial x}{\partial t}\cdot\frac{\partial}{\partial x}\left[-\varepsilon^{\frac{1}{2}}v_0\frac{\partial y}{\partial x} + \frac{\varepsilon^{\frac{3}{2}}v_0}{24}\frac{\partial y}{\partial \tau}\right] + \frac{\partial \tau}{\partial t}\cdot\frac{\partial}{\partial \tau}\left[-\varepsilon^{\frac{1}{2}}v_0\frac{\partial y}{\partial x} + \frac{\varepsilon^{\frac{3}{2}}v_0}{24}\frac{\partial y}{\partial \tau}\right]\\ &= -\varepsilon^{\frac{1}{2}}v_0\cdot\left[-\varepsilon^{\frac{1}{2}}v_0\frac{\partial^2 y}{\partial x^2} + \frac{\varepsilon^{\frac{3}{2}}v_0}{24}\frac{\partial^2 y}{\partial x\partial \tau}\right] + \frac{\varepsilon^{\frac{3}{2}}v_0}{24}\cdot\left[-\varepsilon^{\frac{1}{2}}v_0\frac{\partial^2 y}{\partial \tau\partial x} + \frac{\varepsilon^{\frac{3}{2}}v_0}{24}\frac{\partial^2 y}{\partial \tau^2}\right]\\ &= \varepsilon {v_0}^2\frac{\partial^2 y}{\partial x^2} - \frac{\varepsilon^2 {v_0}^2}{12}\frac{\partial^2 y}{\partial x\partial \tau} + \varepsilon^3\left(\frac{v_0}{24}\right)^2\frac{\partial^2 y}{\partial \tau^2}\end{aligned} \tag{A.22}$$

For L.H.S. of Eq.(A.16), it can be expanded by letting $y = V - \frac{V^2}{2F}$ in Eq.(A.22),

$$\frac{\partial^2}{\partial t^2}\left[V - \frac{V^2}{2F}\right] = \varepsilon {v_0}^2\frac{\partial^2}{\partial x^2}\left[V - \frac{V^2}{2F}\right] - \frac{\varepsilon^2 {v_0}^2}{12}\frac{\partial^2}{\partial x\partial \tau}\left[V - \frac{V^2}{2F}\right] + \varepsilon^3\left(\frac{v_0}{24}\right)^2\frac{\partial^2}{\partial \tau^2}\left[V - \frac{V^2}{2F}\right] \tag{A.23}$$

From Eq.(A.17), it can be inferred that $\frac{\partial}{\partial n} \equiv \varepsilon^{\frac{1}{2}}\frac{\partial}{\partial x}$, $\frac{\partial^2}{\partial n^2} \equiv \varepsilon\frac{\partial^2}{\partial x^2}$, $\frac{\partial^4}{\partial n^4} \equiv \varepsilon^2\frac{\partial^4}{\partial x^4}$ and

hence R.H.S. of Eq.(A.16) can be written as

$${v_0}^2\left[\frac{\partial^2 V}{\partial n^2} + \frac{1}{12}\frac{\partial^4 V}{\partial n^4}\right] = {v_0}^2\left[\varepsilon\frac{\partial^2 V}{\partial x^2} + \frac{1}{12}\varepsilon^2\frac{\partial^4 V}{\partial x^4}\right] \tag{A.24}$$

Sub. Eq.(A.23) and Eq.(A.24) into Eq.(A.16) and using Eq.(A.19) gives

$$\begin{aligned}&\varepsilon {v_0}^2\frac{\partial^2}{\partial x^2}\left[-\frac{\varepsilon Fu}{2} - \frac{\varepsilon^2 Fu^2}{8}\right] - \frac{\varepsilon^2 {v_0}^2}{12}\frac{\partial^2}{\partial x\partial \tau}\left[-\frac{\varepsilon Fu}{2} - \frac{\varepsilon^2 Fu^2}{8}\right]\\ &+\varepsilon^3\left(\frac{v_0}{24}\right)^2\frac{\partial^2}{\partial \tau^2}\left[-\frac{\varepsilon Fu}{2} - \frac{\varepsilon^2 Fu^2}{8}\right] = {v_0}^2\left[\varepsilon\frac{\partial^2}{\partial x^2}\left(-\frac{\varepsilon Fu}{2}\right) + \frac{1}{12}\varepsilon^2\frac{\partial^4}{\partial x^4}\left(-\frac{\varepsilon Fu}{2}\right)\right]\\ &\Rightarrow \frac{\varepsilon^3}{4}\frac{\partial^2\left(u^2\right)}{\partial x^2} - \frac{\varepsilon^3}{12}\frac{\partial^2 u}{\partial x\partial \tau} - \frac{\varepsilon^4}{48}\frac{\partial^2\left(u^2\right)}{\partial x\partial \tau} + \frac{\varepsilon^4}{24^2}\frac{\partial^2 u}{\partial \tau^2} + \frac{\varepsilon^5}{4\cdot 24^2}\frac{\partial^2\left(u^2\right)}{\partial \tau^2} = \frac{\varepsilon^3}{12}\frac{\partial^4 u}{\partial x^4}\end{aligned} \tag{A.25}$$

Keeping terms of order ε^3,

$$\frac{1}{4}\frac{\partial^2\left(u^2\right)}{\partial x^2}-\frac{1}{12}\frac{\partial^2 u}{\partial x\partial\tau}=\frac{1}{12}\frac{\partial^4 u}{\partial x^4}. \tag{A.26}$$

Simplifying Eq.(A.26),

$$\begin{aligned}&\frac{\partial^2 u}{\partial x\partial\tau}-3\frac{\partial^2\left(u^2\right)}{\partial x^2}+\frac{\partial^4 u}{\partial x^4}=0\\ &\Rightarrow\frac{\partial}{\partial x}\left(\frac{\partial u}{\partial\tau}\right)-3\frac{\partial}{\partial x}\left[\frac{\partial\left(u^2\right)}{\partial x}\right]+\frac{\partial}{\partial x}\left(\frac{\partial^3 u}{\partial x^3}\right)=0\end{aligned}. \tag{A.27}$$

Integrating Eq.(A.27) w.r.t. *x* and assume that the integrating constant is zero gives the KdV equation,

$$\begin{aligned}&\frac{\partial u}{\partial\tau}-3\frac{\partial\left(u^2\right)}{\partial x}+\frac{\partial^3 u}{\partial x^3}=0\\ &\Rightarrow\frac{\partial u}{\partial\tau}-6u\frac{\partial u}{\partial x}+\frac{\partial^3 u}{\partial x^3}=0\end{aligned}. \tag{A.28}$$

APPENDIX B: ONE-SOLITON SOLUTION FOR KDV EQUATION

The KdV equation is given as follows:

$$\frac{\partial u}{\partial \tau} - 6u\frac{\partial u}{\partial x} + \frac{\partial^3 u}{\partial x^3} = 0 \quad . \tag{B.1}$$

Assume u travels to the right side at velocity v, let

$$u(x,\tau) = u(x - v\tau) \quad . \tag{B.2}$$

By letting $z = x - v\tau$, it can be inferred that

$$\begin{aligned} &\frac{\partial}{\partial z} \equiv \frac{\partial}{-v\partial \tau} \text{ and } \frac{\partial}{\partial z} \equiv \frac{\partial}{\partial x} \\ &\Rightarrow \frac{\partial}{\partial \tau} \equiv -v\frac{\partial}{\partial z} \equiv -v\frac{\partial}{\partial x} \end{aligned} \quad . \tag{B.3}$$

Hence, by using Eq.(B.3), PDE Eq.(B.1) can be transformed into an ordinary differential equation (ODE)

$$-v\frac{\partial u}{\partial x} - 6u\frac{\partial u}{\partial x} + \frac{\partial^3 u}{\partial x^3} = 0 \quad . \tag{B.4}$$

Integrating Eq.(B.4) w.r.t. x and assuming the integration constant to be zero,

$$\begin{aligned} &-vu - \int 3\frac{\partial (u)^2}{\partial x}dx + \frac{\partial^2 u}{\partial x^2} = 0 \\ &\Rightarrow -vu - 3u^2 + \frac{\partial^2 u}{\partial x^2} = 0 \end{aligned} \quad . \tag{B.5}$$

Assume solution is in the form

$$u(x,\tau) = a\sec h^2\left[b(x - v\tau)\right] \tag{B.6}$$

where a and b are constants to be determined.

Differentiating Eq.(B.6) w.r.t. *x*,

$$\frac{\partial u}{\partial x} = -2ab\left\{\tanh\left[b\left(x-v\tau\right)\right]-\tanh^3\left[b\left(x-v\tau\right)\right]\right\} \tag{B.7}$$

Differentiating Eq.(B.7) w.r.t. *x*,

$$\frac{\partial^2 u}{\partial x^2} = 2ab^2\left\{2\sec h^2\left[b\left(x-v\tau\right)\right]-3\sec h^4\left[b\left(x-v\tau\right)\right]\right\} \tag{B.8}$$

Sub. Eq.(B.6) and Eq.(B.8) into Eq.(B.5),

$$\left(4ab^2-av\right)\sec h^2\left[b\left(x-v\tau\right)\right]-\left(3a^2+6ab^2\right)\sec h^4\left[b\left(x-v\tau\right)\right]=0 \tag{B.9}$$

For the KdV equation to satisfy all *x*, the coefficients of the *sech* functions in Eq.(B.9) must be zero.

$$\begin{cases}4ab^2-av=0\\3a^2+6ab^2=0\end{cases}\Rightarrow\begin{cases}a=-\dfrac{v}{2}\\b=\dfrac{\sqrt{v}}{2}\end{cases} \tag{B.10}$$

Sub. Eq.(B.10) into Eq.(B.6) gives the one soliton solution to the KdV equation,

$$u\left(x,\tau\right)=-\frac{v}{2}\sec h^2\left[\frac{\sqrt{v}}{2}\left(x-v\tau\right)\right] \tag{B.11}$$

To obtain the solution for the LC ladder circuit, sub. Eq.(A.17) and Eq.(A.18) into Eq.(B.11) and putting $\varepsilon = 1$,

$$u\left(n,t\right)=-\frac{v}{2}\sec h^2\left[\frac{\sqrt{v}}{2}n-\left(\frac{\sqrt{v}}{2}+\frac{v^{\frac{3}{2}}}{48}\right)v_0 t\right] \tag{B.12}$$

Hence, the voltages at the LC sections are found by sub. Eq.(B.12) into Eq.(A.19),

$$\begin{aligned}&V_n\left(t\right)=F\Omega^2\sec h^2\left[\Omega n-\left(\Omega+\frac{\Omega^3}{6}\right)v_0 t\right]\\&\text{where }\Omega=\frac{\sqrt{v}}{2},\ v_0=\frac{1}{\sqrt{LC\left(V_0\right)}},\ v=\frac{1}{\sqrt{LC\left(V\right)}}\end{aligned} \tag{B.13}$$

APPENDIX C: SIMPLIFICATION OF LANDAU-LIFSHITZ-GILBERT (LLG) EQUATION FOR USE IN MODELING

This appendix shows the simplification of the Landau-Lifshitz-Gilbert (LLG) equation for use in the NLETL circuit model. The standard LLG equation is given as follows:

$$\frac{d\tilde{M}}{dt} = -\gamma\left(\tilde{M} \wedge \tilde{H}\right) + \frac{\alpha}{M_s}\left(\tilde{M} \wedge \frac{\partial \tilde{M}}{\partial t}\right), \tag{C.1}$$

where

$\tilde{M}$ = *magnetization;*

M_s = *saturation magnetization;*

$\tilde{H}$ = *magnetic field strength;*

α = *dimensionless damping parameter;*

γ = *221 km/C, gyromagnetic ratio.*

Take cross product $\tilde{M} \wedge$ on both sides of Eq.(C.1),

$$\tilde{M} \wedge \frac{d\tilde{M}}{dt} = -\gamma \tilde{M} \wedge \left(\tilde{M} \wedge \tilde{H}\right) + \frac{\alpha}{M_s}\tilde{M} \wedge \left(\tilde{M} \wedge \frac{\partial \tilde{M}}{\partial t}\right). \tag{C.2}$$

Using the vector cross product identity $\underset{\sim}{a}\wedge\left(\underset{\sim}{b}\wedge\underset{\sim}{c}\right)=\underset{\sim}{b}\left(\underset{\sim}{a}\cdot\underset{\sim}{c}\right)-\underset{\sim}{c}\left(\underset{\sim}{a}\cdot\underset{\sim}{b}\right)$, Eq.(C.2)

becomes

$$\tilde{M}\wedge\frac{d\tilde{M}}{dt}=-\gamma\tilde{M}\wedge\left(\tilde{M}\wedge\tilde{H}\right)+\frac{\alpha}{M_s}\left[\tilde{M}\left(\tilde{M}\cdot\frac{d\tilde{M}}{dt}\right)-\frac{d\tilde{M}}{dt}\left(\tilde{M}\cdot\tilde{M}\right)\right]. \tag{C.3}$$

Since $\tilde{M}\cdot\frac{d\tilde{M}}{dt}=0$ and $\tilde{M}\cdot\tilde{M}=M_s{}^2$, Eq.(C.3) can be reduced to

$$\tilde{M}\wedge\frac{d\tilde{M}}{dt}=-\gamma\tilde{M}\wedge\left(\tilde{M}\wedge\tilde{H}\right)-\alpha M_s\frac{d\tilde{M}}{dt}. \tag{C.4}$$

Sub. Eq.(C.4) into Eq.(C.1) gives the Landau-Lifshitz equation in the Gilbert form,

$$\begin{aligned}
&\frac{d\tilde{M}}{dt}=-\gamma\left(\tilde{M}\wedge\tilde{H}\right)+\frac{\alpha}{M_s}\left(-\gamma\tilde{M}\wedge\left(\tilde{M}\wedge\tilde{H}\right)-\alpha M_s\frac{d\tilde{M}}{dt}\right)\\
&\Rightarrow\frac{d\tilde{M}}{dt}=-\gamma\left(\tilde{M}\wedge\tilde{H}\right)-\frac{\gamma\alpha}{M_s}\tilde{M}\wedge\left(\tilde{M}\wedge\tilde{H}\right)-\alpha^2\frac{d\tilde{M}}{dt}\\
&\Rightarrow\frac{d\tilde{M}}{dt}=-\frac{\gamma}{1+\alpha^2}\left[\left(\tilde{M}\wedge\tilde{H}\right)+\frac{\alpha}{M_s}\tilde{M}\wedge\left(\tilde{M}\wedge\tilde{H}\right)\right].
\end{aligned} \tag{C.5}$$

Using the vector cross product identity $\underset{\sim}{a}\wedge\left(\underset{\sim}{b}\wedge\underset{\sim}{c}\right)=\underset{\sim}{b}\left(\underset{\sim}{a}\cdot\underset{\sim}{c}\right)-\underset{\sim}{c}\left(\underset{\sim}{a}\cdot\underset{\sim}{b}\right)$, Eq.(C.5)

becomes

$$\begin{aligned}
&\frac{d\tilde{M}}{dt}=-\frac{\gamma}{1+\alpha^2}\left\{\left(\tilde{M}\wedge\tilde{H}\right)+\frac{\alpha}{M_s}\left[\tilde{M}\left(\tilde{M}\cdot\tilde{H}\right)-\tilde{H}\left(\tilde{M}\cdot\tilde{M}\right)\right]\right\}\\
&\Rightarrow\frac{d\tilde{M}}{dt}=-\frac{\gamma}{1+\alpha^2}\left\{\left(\tilde{M}\wedge\tilde{H}\right)+\frac{\alpha}{M_s}\left[\tilde{M}\left(\tilde{M}\cdot\tilde{H}\right)-M_s{}^2\tilde{H}\right]\right\}.
\end{aligned} \tag{C.6}$$

Assume that the magnetic field strength in the ferrite has only z-component,

$$\tilde{H}=H_z\hat{z}. \tag{C.7}$$

Sub. Eq.(C.7) into Eq.(C.6),

$$\frac{d\tilde{M}}{dt}=-\frac{\gamma}{1+\alpha^2}\left\{\left(\tilde{M}\wedge\tilde{H}\right)+\frac{\alpha}{M_s}M_zH_z\tilde{M}-\alpha M_s\tilde{H}\right\}. \tag{C.8}$$

Expand Eq.(C.8) into components,

$$\begin{bmatrix} \frac{dM_x}{dt} \\ \frac{dM_y}{dt} \\ \frac{dM_z}{dt} \end{bmatrix} = -\frac{\gamma}{1+\alpha^2}\left\{ \begin{bmatrix} M_y H_z \\ -M_x H_z \\ 0 \end{bmatrix} + \begin{bmatrix} \frac{\alpha M_z H_z}{M_s} M_x \\ \frac{\alpha M_z H_z}{M_s} M_y \\ \frac{\alpha M_z H_z}{M_s} M_z \end{bmatrix} - \begin{bmatrix} 0 \\ 0 \\ \alpha M_s H_z \end{bmatrix} \right\}. \tag{C.9}$$

Hence, the component equations are

$$\frac{dM_x}{dt} = -\frac{\gamma}{1+\alpha^2}\left(M_y H_z + \frac{\alpha M_z H_z}{M_s} M_x \right), \tag{C.10}$$

$$\frac{dM_y}{dt} = -\frac{\gamma}{1+\alpha^2}\left(-M_x H_z + \frac{\alpha M_z H_z}{M_s} M_y \right), \tag{C.11}$$

$$\frac{dM_z}{dt} = -\frac{\gamma}{1+\alpha^2}\left(\frac{\alpha {M_z}^2 H_z}{M_s} - \alpha M_s H_z \right). \tag{C.12}$$

Consider only the axial magnetic field strength in the z-direction, Eq.(C.12) is adjusted to form the simplified LLG equation (as shown in Eq.(C.13)) for use in the NLETL circuit model.

$$\begin{aligned} &\frac{dM_z}{dt} = -\frac{\gamma}{1+\alpha^2}\left[\alpha M_s H_z \left(\frac{{M_z}^2}{{M_s}^2} - 1 \right) \right] \\ &\Rightarrow \frac{dM_z}{dt} = -\frac{\alpha\gamma M_s}{1+\alpha^2}\left(1 - \frac{{M_z}^2}{{M_s}^2} \right) H_z \end{aligned}. \tag{C.13}$$

APPENDIX D: DERIVATION OF NLIL DISPERSION EQUATION

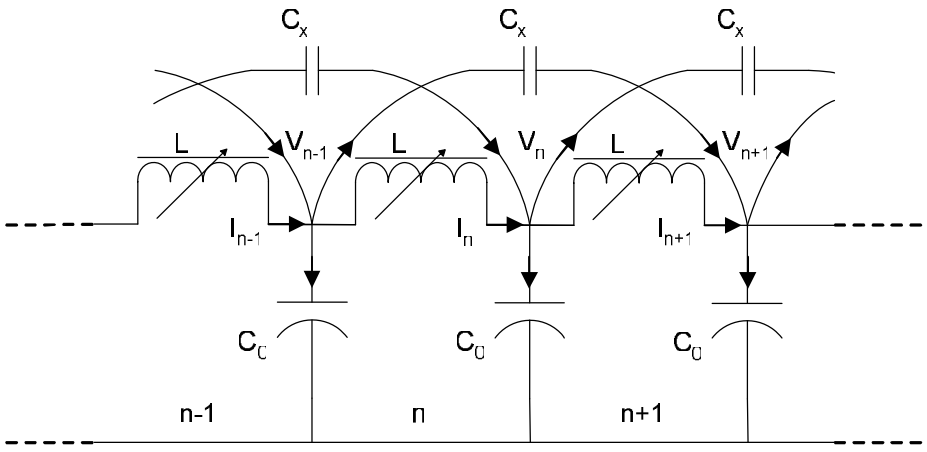

Figure D.1 Circuit diagram of NLIL with crosslink capacitors.

This appendix shows the derivation of the dispersion relation of the NLIL with crosslink capacitors (as depicted in Figure D.1) in the linear regime when the ferrite is saturated. By applying Kirchoff's law to the NLIL circuit and assuming it is lossless, the difference-differential equations at saturated inductance L_0 are:

For n^{th} and $(n+1)^{th}$ inductor,

$$\frac{d\psi_n}{dt} = \frac{d\left(L_0 \cdot I_n\right)}{dt} = L_0 \frac{dI_n}{dt} = V_{n-1} - V_n \quad , \tag{D.1}$$

$$\frac{d\psi_{n+1}}{dt} = \frac{d\left(L_0 \cdot I_{n+1}\right)}{dt} = L_0 \frac{dI_{n+1}}{dt} = V_n - V_{n+1} \quad . \tag{D.2}$$

For the node at V_n,

$$\begin{aligned} & I_n + C_x \frac{d\left(V_{n-2} - V_n\right)}{dt} - I_{n+1} - C_x \frac{d\left(V_n - V_{n+2}\right)}{dt} = C_0 \frac{dV_n}{dt} \\ & \Rightarrow I_n - I_{n+1} + C_x \frac{dV_{n-2}}{dt} + C_x \frac{dV_{n+2}}{dt} - 2C_x \frac{dV_n}{dt} = C_0 \frac{dV_n}{dt} \\ & \Rightarrow I_n - I_{n+1} + C_x \left(\frac{dV_{n-2}}{dt} + \frac{dV_{n+2}}{dt} \right) = \left(C_0 + 2C_x\right) \frac{dV_n}{dt} \end{aligned} \quad \text{(D.3)}$$

Differentiate Eq.(D.3) w.r.t. to t,

$$\frac{dI_n}{dt} - \frac{dI_{n+1}}{dt} = \left(C_0 + 2C_x\right) \frac{d^2V_n}{dt^2} - C_x \left(\frac{d^2V_{n-2}}{dt^2} + \frac{d^2V_{n+2}}{dt^2} \right) \quad \text{(D.4)}$$

Use Eq.(D.1) – Eq.(D.2),

$$V_{n+1} + V_{n-1} - 2V_n = L_0 \left(\frac{dI_n}{dt} - \frac{dI_{n+1}}{dt} \right) \quad \text{(D.5)}$$

Sub. Eq.(D.4) into Eq.(D.5),

$$V_{n+1} + V_{n-1} - 2V_n = L_0 C_0 \frac{d^2V_n}{dt^2} + 2L_0 C_x \frac{d^2V_n}{dt^2} - L_0 C_x \frac{d^2V_{n-2}}{dt^2} - L_0 C_x \frac{d^2V_{n+2}}{dt^2} \quad \text{(D.6)}$$

Now consider a particular harmonic solution of Eq.(D.6) in the form

$$V_n(t) = V_0 \, \mathrm{Re}\left[e^{i(\omega t - \varphi n)} \right] \quad \text{(D.7)}$$

Then it follows that

$$V_{n+1}(t) = V_0 \, \mathrm{Re}\left[e^{i(\omega t - \varphi(n+1))} \right] = e^{-i\varphi} V_0 \, \mathrm{Re}\left[e^{i(\omega t - \varphi n)} \right] = e^{-i\varphi} V_n \quad \text{(D.8)}$$

$$V_{n-1}(t) = V_0 \, \mathrm{Re}\left[e^{i(\omega t - \varphi(n-1))} \right] = e^{i\varphi} V_0 \, \mathrm{Re}\left[e^{i(\omega t - \varphi n)} \right] = e^{i\varphi} V_n \quad \text{(D.9)}$$

$$V_{n+2}(t) = V_0 \, \mathrm{Re}\left[e^{i(\omega t - \varphi(n+2))} \right] = e^{-i2\varphi} V_0 \, \mathrm{Re}\left[e^{i(\omega t - \varphi n)} \right] = e^{-i2\varphi} V_n \quad \text{(D.10)}$$

$$V_{n-2}(t) = V_0 \, \mathrm{Re}\left[e^{i(\omega t - \varphi(n-2))} \right] = e^{i2\varphi} V_0 \, \mathrm{Re}\left[e^{i(\omega t - \varphi n)} \right] = e^{i2\varphi} V_n \quad \text{(D.11)}$$

Differentiate twice for Eqs. (D.7), (D.10) and (D.11) w.r.t. t,

$$\frac{dV_n}{dt} = i\omega V_0 R\mathrm{e}\left[e^{i(\omega t-\varphi n)}\right]$$
$$\Rightarrow \frac{d^2V_n}{dt^2} = -\omega^2 V_0 R\mathrm{e}\left[e^{i(\omega t-\varphi n)}\right] = -\omega^2 V_n \quad , \tag{D.12}$$

$$\frac{dV_{n+2}}{dt} = i\omega V_0 R\mathrm{e}\left[e^{i(\omega t-\varphi(n+2))}\right]$$
$$\Rightarrow \frac{d^2V_{n+2}}{dt^2} = -\omega^2 V_0 R\mathrm{e}\left[e^{i(\omega t-\varphi(n+2))}\right] = -\omega^2 e^{-i2\varphi} V_0 R\mathrm{e}\left[e^{i(\omega t-\varphi n)}\right] = -\omega^2 e^{-i2\varphi} V_n \quad , \tag{D.13}$$

$$\frac{dV_{n-2}}{dt} = i\omega V_0 R\mathrm{e}\left[e^{i(\omega t-\varphi(n-2))}\right]$$
$$\Rightarrow \frac{d^2V_{n-2}}{dt^2} = -\omega^2 V_0 R\mathrm{e}\left[e^{i(\omega t-\varphi(n-2))}\right] = -\omega^2 e^{i2\varphi} V_0 R\mathrm{e}\left[e^{i(\omega t-\varphi n)}\right] = -\omega^2 e^{i2\varphi} V_n \quad . \tag{D.14}$$

Sub. Eqs. (D.8), (D.9), (D.12), (D.13) and (D.14) into Eq.(D.6),

$$e^{-i\varphi}V_n + e^{i\varphi}V_n - 2V_n = L_0C_0\left(-\omega^2 V_n\right) + 2L_0C_x\left(-\omega^2 V_n\right) - L_0C_x\left(-\omega^2 e^{i2\varphi}V_n\right) - L_0C_x\left(-\omega^2 e^{-i2\varphi}V_n\right)$$
$$\Rightarrow e^{-i\varphi} + e^{i\varphi} - 2 = -\omega^2 L_0C_0 - 2\omega^2 L_0C_x + \omega^2 L_0C_x\left(e^{i2\varphi} + e^{-i2\varphi}\right)$$
$$\Rightarrow e^{-i\varphi} + e^{i\varphi} - 2 = -\omega^2 L_0C_0 + \omega^2 L_0C_x\left(e^{i2\varphi} + e^{-i2\varphi} - 2\right)$$
$$\Rightarrow 2\cos(\varphi) - 2 = -\omega^2 L_0C_0 + \omega^2 L_0C_x\left(2\cos(2\varphi) - 2\right)$$
$$\Rightarrow 2\left(\cos(\varphi) - 1\right) = -\omega^2 L_0C_0 + 2\omega^2 L_0C_x\left(\cos(2\varphi) - 1\right)$$
$$\Rightarrow 2\left(-2\sin^2\left(\frac{\varphi}{2}\right)\right) = -\omega^2 L_0C_0 + 2\omega^2 L_0C_x\left(-2\sin^2(\varphi)\right)$$
$$\Rightarrow 4\sin^2\left(\frac{\varphi}{2}\right) - 4\omega^2 L_0C_x\sin^2(\varphi) = \omega^2 L_0C_0 \tag{D.15}$$

Let coupling coefficient γ and critical frequency ω_c be defined as follows:

$$\gamma = \frac{C_x}{C_0} \quad , \tag{D.16}$$

$$\omega_c = \frac{2}{\sqrt{L_0C_0}} \quad . \tag{D.17}$$

Sub. Eq.(D.16) into Eq.(D.15),

$$4\sin^2\left(\frac{\varphi}{2}\right)-4\omega^2 L_0 C_0 \gamma \sin^2(\varphi)=\omega^2 L_0 C_0$$

$$\Rightarrow \sin^2\left(\frac{\varphi}{2}\right)-4\gamma\frac{\omega^2}{\left(\frac{2}{\sqrt{L_0C_0}}\right)^2}\sin^2(\varphi)=\frac{\omega^2}{\left(\frac{2}{\sqrt{L_0C_0}}\right)^2}. \tag{D.18}$$

Hence, the dispersion equation is obtained by sub. Eq.(D.17) into Eq.(D.18),

$$\sin^2\left(\frac{\varphi}{2}\right)-4\gamma\frac{\omega^2}{\omega_c^{\,2}}\sin^2(\varphi)=\frac{\omega^2}{\omega_c^{\,2}}, \tag{D.19}$$

where φ is the phase shift per link.

Now switch from the φn notation in Eq.(D.7) to the more common kx notation. We define k by

$$kx\equiv n\varphi \Rightarrow k\left(nd\right)=n\varphi \Rightarrow kd=\varphi, \tag{D.20}$$

where we assume d is the distance between sections and x is the distance from the first section.

The phase velocity v_p and group velocity v_g are then determined by

$$v_p=\frac{\omega}{k}=\frac{\omega d}{\varphi}, \tag{D.21}$$

$$v_g=d\frac{d\omega}{d\varphi}. \tag{D.22}$$